Subradiance Protected Excitation Transport

Jemma Ann Needham

A thesis presented for the degree of
Doctor of Philosophy

SCHOOL OF PHYSICS AND ASTRONOMY
UNIVERSITY OF NOTTINGHAM

UNITED KINGDOM
JULY 2020

ABSTRACT

We investigate collective behaviour that appears in open, many-body systems of two- and four-level atoms. Here, "open" refers to the system interacting with an external environment that causes dissipation. We derive a general open quantum master equation to describe the system dynamics only, independent of this environment. We identify processes such as coherent exchange of virtual photons and modified decay rates caused by long-range interactions between all pairs of atoms that scale with distance by inverse power laws.

We explore excitation transport within a one-dimensional chain of atoms where the atomic transition dipoles are coupled to the free radiation field. When the interatomic spacing is smaller than or comparable to the wavelength of light associated with the photon emitted from a given transition, virtual photon exchange interactions facilitate excitation transport through the chain. Atomic systems coupled to an environment display dissipative dynamics, however subradiant transport is exhibited from a variety of initial states; spontaneous emission from the chain occurs at a rate much slower than that for an individual atom. In particular, we find a region within the decay spectrum that consists entirely of subradiant states with a corresponding linear dispersion relation in the interaction energy. Identifying this subspace allows for the dispersionless transport of wave packets over long distances with near-zero decay. Moreover, the group velocity of the wave packet and direction of the transport can be controlled via an external uniform magnetic field while preserving its subradiant character.

We discuss a number of experimental considerations to justify the feasibility and robustness of this protocol. Initial state preparation is outlined, utilising external laser driving to excite the system into the single excitation sector. Furthermore, we consider positional disorder by explicitly accounting for the external atomic degrees of freedom – position and momentum – which allows us to model the positions of all atoms by a motional state representing the occupation of a lattice well with a given width. These discussions are made in the low-temperature limit, where the atomic motion is essentially frozen, and we identify that subradiant transport is indeed robust.

Finally, we explore the experimental limits of interatomic spacing and imperfect filling within an experimentally achievable optical lattice. We calculate the photon emission rate – an experimentally measurable quantity – and compare the emission spectra to our analysis. By limiting parameters to those achieved experimentally, we observe a reduction, yet not an absence, of collective behaviour.

The simplicity and versatility of this system, together with the robustness of subradiance against disorder, makes it relevant for a range of applications such as lossless energy transport and long-time light storage. The lifetime of an atomic excitation could be increased by a factor of thousands to millions for a chain of atoms under the conditions that we explore in this thesis.

LIST OF PUBLICATIONS

The research presented in this thesis is largely the subject of the following manuscripts, both published and in preparation. Here, we list these with the chapters that the work appears in.

Chapter 3:

1. **J.A. Needham**, I. Lesanovsky, & B. Olmos, "Subradiance-protected excitation transport." *New Journal of Physics*, vol. 21, no. 7, p. 073061, 7 2019.

    - I performed analytical calculations, guided by known theory.
    - I developed computational simulations and made numerical calculations of the dynamical system behaviour.
    - I created early iterations of the figures used in the manuscript.
    - I wrote a first draft of the published paper and assisted my supervisor in producing the finished manuscript.

2. R. Jones, **J. A. Needham**, I. Lesanovsky, F. Intravaia, & B. Olmos, "Modified dipole-dipole interaction and dissipation in an atomic ensemble near surfaces." *Phys. Rev. A*, vol. 97, p. 053841, 4 2018.

    - Using coefficients, calculated by Ryan Jones, for the coherent and incoherent long-ranged interactions between atoms, I performed numerical calculations to simulate an excitation transport through a chain of atoms in the presence of metallic surfaces.
    - Results from my simulations are outlined in Section. 4 of the manuscript and assisted with the creation of Figure. 11.

Chapter 4:

1. **J.A. Needham**, D. Braun, I. Lesanovsky, & B. Olmos, "Robustness of subradiance against motion and disorder." *manuscript in preparation*.

    - Supported by relevant literature, I analytically derived equations of motion to describe a many-body system incorporating atomic motion.
    - I produced numerical simulations to collect results for the manuscript.
    - I produced a full first draft of the manuscript which includes the creation of all figures using the results of my simulations.

To the whole family cohort.

ACKNOWLEDGEMENTS

Firstly I would like to say a big thank you to my supervisor Beatriz Olmos Sanchez for the constant support and guidance throughout my PhD both professionally and personally. It's been a pleasure to tackle this research together, you've been an absolute inspiration. Thanks to Igor Lesanovsky for his suggestions and collaboration which helped to bring this research to fruition. Finally, I thank you both for the numerous invitations to Tübingen and for your hospitality which led to the smooth completion of this PhD.

I am very grateful to Robin Kaiser for hosting me in Nice. Insightful discussions in this week visit very much motivated a significant amount of research presented in this thesis. Likewise, I am very thankful for discussions and working relationships within the Condensed Matter Theory group. In particular, I thank my fellow PhD students. We have worked together and we have created friendships that I will value always. You've kept me laughing every day and you've kept me sane! I am so grateful to have entered the world of research with Matt Jessop, Maike Ostmann and Loredana Vasiliou. We have taken this journey together and I am so thankful to have known you through this. To Ciarán, Gary, Maike, Matt, Neil, Joe, Charlotte and Dom: thank you for your help in finishing this thesis, I really appreciate the time and care taken to support me at this time.

Alongside work, I have had an incredible support system from so many people outside of academia. I thank the coaches at Mickleover Gymnastics for your patience and support while I balanced PhD life and coaching. I thank the gymnasts of Impulse for giving me the best possible distraction from everything on a Thursday evening and for your awesome gymnastics ability.

A special thank you to my absolutely wonderful housemate Charlotte Beach. We are such an awesome team and I couldn't have adulted without you. Thank you for helping me to live you beautiful, talented, brilliant, powerful muskox.

Of course, I have my wonderful family to acknowledge for a whole number of reasons. You are my emotional support, my safety and my rock. Thank you Mum, Dad, Sheila, Joe, Sammy and Chris.

Finally, I thank Dominic Rose. You are an unexpected, beautiful lifeline and while I know that I am strong by myself (you taught me this), everything is so much clearer and more vibrant with you by my side. Thank you, I love you.

TABLE OF CONTENTS

Chapter 1
Introduction

The interaction between light and matter has been a phenomenon of great interest in the physics community for theorists and experimentalists alike, in both classical and quantum settings, for much of the last century. Let us begin by considering a single atom: if we assume that the atom contains an excitation, with no external influence the atomic state would be stable. However, what if the atom interacts with an electromagnetic field? For instance, let us explore the interaction between the atom and the vacuum radiation field.

A free radiation field allows for the emission of photons with momenta and direction taken from a continuous spectrum containing an infinite number of modes. This transition takes the atom from its excited state to its ground state. The free radiation field is frequently used to model the environment that an atom exists within and in general cannot be ignored. By considering every decay channel available to the excited atom, due to the vacuum field, one finds a decay rate that we define as the spontaneous emission rate of the given atomic transition. The process of spontaneous emission was derived from first principles by Dirac in 1927 [1], and this specific example of the single atom interacting with the vacuum field was studied by Wigner and Weisskopf in the 1930s [2].

The idea of spontaneous emission had already been introduced at this time by Einstein, inline with his development of laser theory in 1917 [3]. The creation of the laser followed this in 1960, by Theodore H Maiman [4] which opened up many opportunities to explore light-matter interactions experimentally, and prompted further theoretical investigation.

Even with a single emitter, the dynamics associated with the interaction between matter and the free radiation field is not easily solvable analytically. However, there are many modifications that can be made to the radiation field that make the dynamics readily solvable. For instance, the Jaynes-Cummings model, detailed in 1963, explores the interaction that couples an atom, modelled by two energy levels (two-level atom), to a single quantised mode of an electromagnetic (EM) field [5]. The radiation field in this case can be restricted by placing the atom within a cavity, where there exists only one optical cavity mode. This model is exactly solvable and research in this area has paved a route into the field of cavity quantum electrodynamics [6].

Alternatively, one can still explore a single atom interacting with the free radiation

field using a method that allows us to extract relevant information about the system (the atom) from what we can describe as a bath (the free EM field). This necessity results in what we call open quantum systems [7].

Theoretical analysis of this type of problem was made possible by the formalism of the density matrix, as posed by von Neumann in 1927 [8]. The time evolution of the system's density matrix is given by a quantum master equation, derivable from a full description of the system-bath dynamics. In cases where the complexity of the bath – otherwise known as the environment – restricts our ability to derive exact system dynamics, we make several assumptions on the bath. For instance, we assume weak coupling between the system and the bath, since the bath is very large and is mostly unchanged by interaction with the system. Likewise, we assume that correlations between the two exist on very short timescales such that the bath is essentially "memoryless", hence the dynamics are Markovian. At approximately the same time in 1976, four theoretical physicists – Vittorio Gorini, Andrzej Kossakowski, George Sudarshan and Göran Lindblad – derived the dynamics for such systems under these assumptions, allowing one to trace out the bath and derive a master equation for the system only [9, 10]. This is often referred to as the GKLS or Lindblad equation and was the first reported derivation of a Markovian quantum master equation that demonstrated trace-preservation and complete positivity.

Now, instead of a single atom (emitter), consider an ensemble of emitters that couple collectively to a common EM bath. The atoms will couple to each other via the EM field which gives rise to collective phenomena. Research into coherent behaviour of many atoms was greatly led by Dicke [11] and was developed further in the late 20th century [12,13]. Here, the exchange of virtual photons results in induced dipole-dipole interactions [14–16] and collective Lamb and Lorentz-Lorenz shifts [17–24]. Moreover, the incoherent, spontaneous photon emission into the bath is modified, evidenced by the appearance of collective decay rates which are much larger (superradiant) and much smaller (subradiant) than the individual atom decay rate [25–31].

The appearance of superradiance, reported by Dicke [11], has been a known response for much of the last century, however research surrounding cooperative behaviour in light-matter experiments remains relevant and is an advancing subject even today. Early experimental research of collectivity has been restricted due to the requirement of close atomic spacing. Cooperative behaviour mostly features in dense ensembles, where the interparticle separations are comparable to or smaller than the wavelength of the scattered light, or dilute ensembles with a very large number of emitters. These systems have returned to the forefront in quantum optics in recent years due to new capabilities in atom trapping [32,33]. Magneto-optical traps (MOTs) permit the exploration of dense and dilute, three-dimensional atomic gases [28]. Additionally, optical lattices and tweezers demonstrate sizeable control for the loading

of atoms into array-like geometries at separations comparable to the atomic transition wavelength [34]. Once again, it is worth noting that this was not possible without the creation of the laser. Not only do these trapping techniques provide accessibility to the relevant spatial regimes required to observe collective phenomena, but it opens up possibilities to explore different geometries of trapped atoms [35, 36].

The capabilities described above have allowed for the observation of superradiance and subradiance experimentally in the form of light scattering and collective decay rates. For example, Pellegrino et al. examined the collective effects of an illuminated cold rubidium cloud [21]. The effect of system size on the observed collective behaviour was measured as broadening, lineshifts and suppression of scattered light. Moreover, experiments performed by Kaiser et al. have demonstrated the appearance of subradiance in dilute thermal atomic gases, trapped in MOTs [28]. Successful experimental investigations demonstrate the need for continued theoretical support to highlight the potential for cooperativity in a variety of different geometries and types of many-body system. For instance, one can compare the theoretical findings regarding collectivity using the high-lying Rydberg states [37–40] to low-lying states in alkaline earth atoms [14].

In addition, significant investigations have been performed for one- [41, 42] and two-dimensional [36] regular arrays of atoms, considering factors such as system size [43] and the response of the system to disorder [44]. Investigations of this type are becoming more imperative due to their growing practicality; in recent years a number of research groups have been exploring the application of thin atomic layers as optical mirrors. This state of the art research has found particular success using uniform atomic arrays, as first proposed by Bettles et al. for a two-dimensional triangular lattice of atoms [45]. By fine-tuning the lattice spacing, the amount of transmitted light through the atomic layer was reduced to a negligible amount. These results have promoted further interest in the ability to manipulate reflectance and transmittance of light from atomic arrays, in both theoretical [46, 47] and experimental [48] investigations, for square lattice atomic arrays.

While the understanding of many-body atomic systems interacting with the free radiation field remains a key topic in quantum optics, an increasing number of groups are also researching the modification of fluorescence due to nearby surfaces [49]. In 1946, Purcell et al. hypothesised that the spontaneous emission rate is dependent on the photon mode density of the surrounding environment [50]. This has been confirmed with a growing understanding of how the environment of an atomic ensemble is altered in the presence of metallic and dielectric surfaces [51, 52], accompanied by further investigations into the modified coherent and incoherent interactions associated with collective phenomena [53].

These are just a couple of examples for the avenues and applications of interacting

atomic systems, and this list is certainly not exhaustive. To illustrate, this type of collective atom-light coupling has also found a variety of applications such as storage of light via the preparation of subradiant states through phase-imprinting protocols [36,54–63], topologically protected transport of excitations [35,64], and efficient long-range energy transport [65–70]. It is also worth noting that super- and subradiance have been observed experimentally not only in atomic gases, but also in QED circuits [71, 72], metamaterial arrays [73], and quantum dots [74–76]. However, we focus solely on collectivity in many-body atomic systems.

1.1 Structure of the thesis

This thesis is structured as follows: we begin by introducing the mathematical techniques, frequently used in literature, to derive a quantum master equation that describes the dynamics of a system interacting with a bath, in Chapter 2. In this very general formalism, we outline the assumptions that allow us to extract the system dynamics only, and we apply the model in particular to the case of many-body atomic systems interacting with the many-mode free radiation field. The atoms are modelled as either two-level atoms (one ground and one excited state) or four-level atoms (one ground and three degenerate excited states). We make a brief analysis on how collective behaviour appears in terms of coherent interactions and incoherent dissipation, before considering modifications to the quantum master equation due to external fields such as laser driving and the application of a magnetic field.

We proceed with a discussion of our research findings in Chapter 3, where we explore the features of collectivity further by deriving dynamical equations within the single excitation sector. Taking this regime allows us to vastly reduce the Hilbert space, and consequently, the complexity of the many-body problem. We explore the potential for transport of a single excitation through uniform, one-dimensional atomic arrays, utilising the cooperative nature arising from closely separated lattice sites. By investigating the form of interaction and dissipation coefficients within the master equation, we improve the fidelity and coherence of the transported wave packet.

Various experimental considerations that we made are outlined in Chapter 3, such as initialisation of the state by laser driving, control of dipole moments using a magnetic field, modification of the radiation field in the presence of metallic surfaces, and the effect of positional disorder due to finite well widths.

We expand on this last consideration in Chapter 4, where we directly model the motional states of the atoms at the level of the Hamiltonian. Chapter 4 begins with a re-derivation of results found in Reference [77]. We derive an analogous quantum master equation, where the external motion of the atoms is considered as a part of

the bath. We extend the motional states describing the external atomic degrees of freedom from one dimension (see Reference [77]) to three. We then use our master equation to make a comparison to the fixed position case for one-dimensional arrays at various temperatures. An additional investigation is made in this chapter for the temperature dependence of collectivity within a three-dimensional MOT, which takes us from cooperativity within a Bose-Einstein Condensate (BEC) to a dilute, thermal gas.

Moreover, we make further investigations into the experimental feasibility of a cooperative one-dimensional chain in Chapter 5. By setting parameters, such as the interatomic spacing lengthscales and filling fraction, to values that one can achieve experimentally, we explore the possibility of observing collectivity. As a part of our exploration, we analyse the cooperative behaviour once again by investigating the dissipation and interaction modes taken directly from the master equation. We also numerically calculate the photon emission rate of the atomic chain in the steady state with weak laser driving. By analysing this emission spectra, we are able to directly relate the features of the spectra to the collective properties extracted from the master equation. A combination of these results creates potential for predicting the shape of the photon emission rate in different parameter regimes, which is frequently measured in experiments of this nature.

The results from these three research chapters (Chapters 3, 4 and 5) are gathered in Chapter 6. We summarise the outcomes of the research presented in this thesis, discuss their impact and propose future avenues for this work.

Chapter 2
Theoretical framework

The purpose of this chapter is to introduce the mathematical techniques utilised in later chapters for the analysis of cooperative many-body effects. We begin by introducing a general Hamiltonian for open quantum systems in Sec. 2.1 that is used to derive the master equation describing a system interacting with a bath (also referred to as a reservoir). We outline a method for tracing out the reservoir degrees of freedom, and specify where the relevant approximations are applied and justified.

In Sec. 2.2, we explore the origin of the system-bath interaction for a specific case: a single atom interacting with a classical electromagnetic (EM) field, which we modify in Sec. 2.3 to model a many-body atomic system with a quantised EM field. We use the simple two-level atom model and derive the corresponding master equation.

We briefly analyse the emergence of collective behaviour in the master equation in Sec. 2.4, before introducing a laser driving term that will allow us to describe the process of state preparation necessary for the observation of interesting dynamics, in Sec. 2.5. We conclude the chapter by exploring the analogous case for a collection of four-level atoms in Sec. 2.6. Presenting these two scenarios here allows us to compare the models and identify cases when it may be appropriate to simplify to the two-level model, in later chapters.

2.1 The master equation

A quantum system interacting with a bath can be described by the Hamiltonian

$$H = H_{\mathrm{s}} + H_{\mathrm{b}} + V, \tag{2.1}$$

where H_{s} and H_{b} are the bare system and bath Hamiltonians, respectively whose eigenvalues and eigenvectors have known solutions, and V describes the interaction between them. While this type of Hamiltonian is a useful expression for understanding the properties of the system and bath as well as the coupling between them, in many cases we are only interested in properties of the system. We instead find the master equation and trace out the bath degrees of freedom. The procedure for deriving a master equation for an open quantum system, in general, is described in Reference [7]. A directly related derivation for two-level systems is given in Reference [12], and we

use this extensively in the calculations that follow.

The von-Neumann equation provides us with the time evolution of the density matrix ρ_S which contains information about all possible states of both the system and the bath [78]

$$\dot{\rho}_S = -\frac{\mathrm{i}}{\hbar}\left[H, \rho_S\right]. \tag{2.2}$$

This equation holds for ρ_S in the Schrödinger picture; the time dependence is contained within the state as opposed to the operators. We then move to the interaction picture, such that the time-dependence is shared between both state and operators. By making this transformation, we are able to solve problems with explicit time dependence within the interaction Hamiltonian. In the interaction picture the density matrix at a given time t is $\rho_I(t) = U^\dagger(t)\rho_S U(t)$, where $U(t) = U_\mathrm{s}(t)U_\mathrm{b}(t)$. The individual factors of this unitary operator are

$$U_{\mathrm{s/b}}(t) = \mathrm{e}^{\frac{-\mathrm{i}H_{\mathrm{s/b}}t}{\hbar}}, \tag{2.3}$$

which commute, since $U_\mathrm{s}(t)$ is only dependent on system operators whereas $U_\mathrm{b}(t)$ is dependent on bath operators. Applying these unitary operators in this way to Eq. (2.2) returns

$$\dot{\rho}_I(t) = -\frac{\mathrm{i}}{\hbar}\left[V_I(t), \rho_I(t)\right], \tag{2.4}$$

the equation in the interaction picture where $V_I(t) = U^\dagger(t)VU(t)$. By formally integrating this expression with respect to time

$$\rho_I(t) = \rho_I(0) - \frac{\mathrm{i}}{\hbar}\int_0^t \mathrm{d}t' \,[V_I(t'), \rho_I(t')], \tag{2.5}$$

and substituting this back into Eq. (2.4) we find

$$\dot{\rho}_I(t) = -\frac{\mathrm{i}}{\hbar}[V_I(t), \rho_I(0)] - \frac{1}{\hbar^2}\int_0^t \mathrm{d}t' \,\Big[V_I(t), [V_I(t'), \rho_I(t')]\Big]. \tag{2.6}$$

This equation contains information on both the system states and the bath states. We are however only interested in the system dynamics, hence we take a partial trace over the reservoir field modes

$$\dot{\rho}(t) = -\frac{\mathrm{i}}{\hbar}\mathrm{Tr_b}\left\{[V_I(t), \rho_I(0)]\right\} - \frac{1}{\hbar^2}\int_0^t \mathrm{d}t' \,\mathrm{Tr_b}\left\{\Big[V_I(t), [V_I(t'), \rho_I(t')]\Big]\right\}, \tag{2.7}$$

where $\rho(t) = \mathrm{Tr_b}\{\rho_I(t)\}$ is the density matrix for the system in the interaction picture. At $t = 0$ we assume that there are no correlations between the system and bath, hence $\rho_I(0) = \rho(0) \otimes \rho_I^\mathrm{b}(0)$. Moreover, the first term can be neglected without loss of generality, since it acts as a shift in the zero point energy and can be absorbed into the

system Hamiltonian.

At later times, we assume that the interaction between the system and the reservoir is weak and that the reservoir is large enough to be unaffected by changes in the system. This assumption of weak coupling allows us to express the density matrix as the tensor product $\rho_I(t') \rightarrow \rho(t') \otimes \rho_I^{\mathrm{b}}(0) + \mathcal{O}(V)$ and we will neglect higher order interaction terms $\mathcal{O}(V)$. Making this assumption is referred to as the Born approximation.

Another assumption is that the lifetime of the correlations between the system and the bath are very short in comparison to the timescale associated with the system dynamics. The reservoir is therefore said to be "memoryless", and the time evolution of the system density matrix is only dependent on its instantaneous value $\rho_I(t') \rightarrow \rho_I(t)$. This description defines the Markov approximation, which also allows us to take the upper limit of the integral from $t \rightarrow \infty$, leading to the following expression:

$$\dot{\rho}(t) = -\frac{1}{\hbar^2} \int_0^\infty \mathrm{d}\tau \, \mathrm{Tr}_{\mathrm{b}} \left\{ \Big[V_I(t), [V_I(t-\tau), \rho(t) \otimes \rho_I^{\mathrm{b}}(0)] \Big] \right\}, \tag{2.8}$$

where $\tau = t - t'$. We justify the extension of the integral limit, since the correlations between system and reservoir decay to zero quickly and no additional information is supplied by taking this limit. From this point, we will consider the time dependence of the system density matrix implicitly $\rho(t) \rightarrow \rho$.

2.2 The system and the bath

Having derived a general master equation for open quantum systems, we now apply this to an ensemble of atoms (system) interacting with an external electromagnetic field (bath). For clarity, we redefine the system indices as $\mathrm{s} \rightarrow \mathrm{a}$ and the bath indices as $\mathrm{b} \rightarrow \mathrm{f}$. In order to understand the form of the interaction between atoms and field, we first consider the description of a single atom within a classical electromagnetic field. The Hamiltonian describing a single electron of mass m bound to an atom is

$$H_{\mathrm{a}} = \frac{1}{2m}\mathbf{p}^2 + \mathcal{V}(\mathbf{r}), \tag{2.9}$$

with the centre of mass position $\mathbf{r}$ and momentum operator $\mathbf{p}$, and $\mathcal{V}(\mathbf{r})$ is the coulomb potential. If the atom is placed in an external field, the Hamiltonian is altered to

$$H'_{\mathrm{a}} = \frac{1}{2m}[\mathbf{p} + e\mathbf{A}(\mathbf{r}, t)]^2 - e\Phi(\mathbf{r}, t) + \mathcal{V}(\mathbf{r}), \tag{2.10}$$

where $\mathbf{A}(\mathbf{r},t)$ and $\Phi(\mathbf{r},t)$ are the vector and scalar potentials of the field, respectively [79]. A solution for the vector potential can be found using Maxwell's equation:

$$\nabla^2\mathbf{A} - \frac{1}{c^2}\frac{\partial^2\mathbf{A}}{\partial t^2} = 0 \quad \Rightarrow \quad \mathbf{A}(\mathbf{r},t) = \mathbf{A}_0 \mathrm{e}^{i(\mathbf{k}\cdot\mathbf{r}-\omega t)} + \text{H.c.}. \tag{2.11}$$

In this definition, H.c. represents the Hermitian conjugate, $\mathbf{k}$ is the wave vector of the field with modulus $|\mathbf{k}| = 2\pi/\lambda_{\mathbf{k}}$ (dependent on the wavelength of the field $\lambda_{\mathbf{k}}$) and $\mathbf{r}$ is the separation of the electron and nucleus in the atom. The electric field $\mathbf{E}(\mathbf{r},t)$ and magnetic field $\mathbf{B}(\mathbf{r},t)$ depend on the vector and scalar potentials as follows

$$\mathbf{E}(\mathbf{r},t) = -\nabla\Phi(\mathbf{r},t) - \frac{\partial\mathbf{A}(\mathbf{r},t)}{\partial t}, \quad \mathbf{B}(\mathbf{r},t) = \nabla\times\mathbf{A}(\mathbf{r},t), \tag{2.12}$$

and they are invariant under the gauge transformations

$$\begin{aligned} \Phi'(\mathbf{r},t) &= \Phi(\mathbf{r},t) - \frac{\partial\chi(\mathbf{r},t)}{\partial t}, \\ \mathbf{A}'(\mathbf{r},t) &= \mathbf{A}(\mathbf{r},t) + \nabla\chi(\mathbf{r},t), \end{aligned} \tag{2.13}$$

where $\chi(\mathbf{r},t)$ is a gauge function.

We now apply the dipole approximation to the vector potential by assuming that $\mathbf{k}\cdot(\mathbf{r}-\mathbf{r}_0) \ll 1$ where $\mathbf{r}_0$ is the position of the atom nucleus. This approximation is justified since the separation of electron and nucleus is much smaller than the field wavelength, the exponential factor in Eq. (2.11) is Taylor expanded around $\mathbf{k}\cdot\mathbf{r} = \mathbf{k}\cdot\mathbf{r}_0$ [80]. The vector potential in the dipole approximation is given by

$$\mathbf{A}(\mathbf{r}_0,t) = \mathbf{A}_0\cos(\mathbf{k}\cdot\mathbf{r}_0 - \omega t), \tag{2.14}$$

where the spatial dependence has been eliminated.

Selecting the Coulomb gauge [$\nabla\cdot\mathbf{A}(\mathbf{r}_0,t) = 0, \Phi(\mathbf{r},t) = 0$], choosing the gauge function $\chi(\mathbf{r},t) = -\mathbf{A}(\mathbf{r}_0,t)\cdot\mathbf{r}$ and using that $\mathbf{E} = -\frac{\partial\mathbf{A}}{\partial t}$, the gauge transformations simplify to

$$\begin{aligned} \Phi'(\mathbf{r},t) &= \frac{\partial\mathbf{A}(\mathbf{r}_0,t)\cdot\mathbf{r}}{\partial t} = -\mathbf{E}(\mathbf{r}_0,t)\cdot\mathbf{r}, \\ \mathbf{A}'(\mathbf{r},t) &= \mathbf{A}(\mathbf{r}_0,t) - \nabla(\mathbf{A}(\mathbf{r}_0,t)\cdot\mathbf{r}) = 0. \end{aligned} \tag{2.15}$$

Therefore, the Hamiltonian is

$$\begin{aligned} H'_{\mathrm{a}} &= \frac{1}{2m}[\mathbf{p} + e\mathbf{A}'(\mathbf{r},t)]^2 - e\Phi'(\mathbf{r},t) + \mathcal{V}(\mathbf{r}) \\ &= \frac{1}{2m}\mathbf{p}^2 + e\mathbf{E}(\mathbf{r}_0,t)\cdot\mathbf{r} + \mathcal{V}(\mathbf{r}) \\ &= H_{\mathrm{a}} - \mathbf{D}\cdot\mathbf{E}(\mathbf{r}_0,t), \end{aligned} \tag{2.16}$$

which tells us that the interaction between an atom and a reservoir EM field is described entirely by the term $-\mathbf{D}\cdot\mathbf{E}(\mathbf{r}_0,t)$ where $\mathbf{D}=-e\mathbf{r}$ is the atomic dipole operator [81].

2.3 Two-level atoms interacting with a quantised EM field

Using Eq. (2.1), we can now model the system as a collection of N atoms (H_a) which interacts with a reservoir EM field (H_f):

$$H = H_\mathrm{a} + H_\mathrm{f} - \sum_{\alpha=1}^{N} \mathbf{D}_\alpha \cdot \mathbf{E}(\mathbf{r}_\alpha, t). \tag{2.17}$$

We have introduced a summation of interaction terms to represent each atom α centred at $\mathbf{r}_\alpha$ with an assigned dipole operator $\mathbf{D}_\alpha$.

H_a is expressed in terms of atomic operators. For simplicity, we model the atoms as two-level atoms, as depicted in Fig. 2.1. Each atom can occupy either a ground state $|g\rangle$ or an excited state $|e\rangle$, and these levels are separated by energy $E_e - E_g = \hbar\omega_\mathrm{a}$ which is proportional to the transition frequency ω_a. This type of approximation is necessary for modelling atoms, due to the vast and complex level structure associated with the electron configuration. We are able to reduce this type of structure when a single transition can be isolated from all others. In general, we require $|g\rangle$ to be the atomic ground state, or a very long-lived state, with forbidden transitions to lower energy levels, and the system must be set up such that the transition to $|e\rangle$ is the only allowed transition. This condition is achieved, for example, by applying a laser field with a frequency and polarisation that matches the desired transition or with small detuning. An example of a two-level atom is the isolated ${}^3P_0 - {}^3D_1$ transition in strontium, provided that an external magnetic field is present to ensure splitting of the degenerate excited state (see Sec. 2.6). The ground state in this case is the lowest energy level in the triplet manifold, and rarely transitions to the true (singlet) ground state due to dipole selection rules [82]. For this work, we consider atomic transitions with frequency ω_a in the optical spectrum, which corresponds to transition wavelengths on the order of $\sim 100\mathrm{nm}$.

The Hamiltonian for a system of N two-level atoms can be written in terms of the spin-z Pauli matrix for each atom,

$$H_\mathrm{a} = \sum_{\alpha=1}^{N} \frac{1}{2}\hbar\omega_\mathrm{a}\sigma_z^\alpha, \tag{2.18}$$

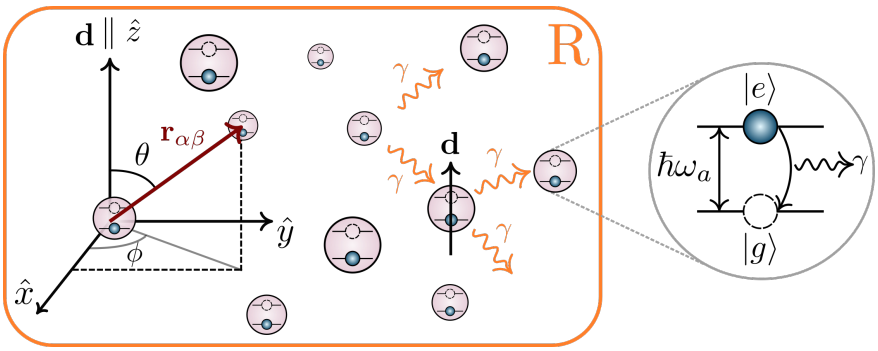

Figure 2.1: **System and reservoir.** A many-body system of two-level atoms, with transition frequency ω_{a} between the single atom ground state $|g\rangle$ and the excited state $|e\rangle$. Interactions between the atoms occur via the exchange of virtual photons and are facilitated by the reservoir field, denoted in orange by R. The atomic dipole moments $\mathbf{d}$ are here aligned with the quantisation axis, in the $\hat{z}$-direction, and the separation between a pair of atoms, α and β, is given by the vector $\mathbf{r}_{\alpha\beta}$.

using the shorthand

$$\sigma_z^\alpha = \left(\bigotimes_{n=1}^{\alpha-1} \mathbb{1}\right) \otimes \sigma_z \otimes \left(\bigotimes_{n=\alpha+1}^{N} \mathbb{1}\right), \tag{2.19}$$

where $\mathbb{1}$ is the identity such that σ_z^α only acts on the index specified. The Pauli matrices for a single atom, defined in the operator, matrix and Dirac notation [83] are

$$\begin{aligned}
\sigma_x &= \begin{pmatrix} 0 & 1 \\ 1 & 0 \end{pmatrix} &&= |e\rangle\langle g| + |g\rangle\langle e|, \\
\sigma_y &= \begin{pmatrix} 0 & -\mathrm{i} \\ \mathrm{i} & 0 \end{pmatrix} &&= -\,\mathrm{i}\left(|e\rangle\langle g| - |g\rangle\langle e|\right), \\
\sigma_z &= \begin{pmatrix} 1 & 0 \\ 0 & -1 \end{pmatrix} &&= |e\rangle\langle e| - |g\rangle\langle g|,
\end{aligned} \tag{2.20}$$

which also appear in the definition of the raising and lowering operators of the atomic states

$$\begin{aligned}
\sigma_+ &= \frac{1}{2}(\sigma_x + \mathrm{i}\sigma_y) = \begin{pmatrix} 0 & 1 \\ 0 & 0 \end{pmatrix} = |e\rangle\langle g|, \\
\sigma_- &= \frac{1}{2}(\sigma_x - \mathrm{i}\sigma_y) = \begin{pmatrix} 0 & 0 \\ 1 & 0 \end{pmatrix} = |g\rangle\langle e|.
\end{aligned} \tag{2.21}$$

These operators are representative of a state being raised from the ground to excited state, and being lowered from the excited to the ground state, respectively. Utilising Dirac notation, we will also refer to the operator acting on a particular atom α by introducing the atom index, for example $\sigma_+^\alpha = |e\rangle_\alpha\langle g|$ and $\sigma_-^\alpha = |g\rangle_\alpha\langle e|$.

The non-interacting field term of the Hamiltonian is expressed in terms of creation and annihilation operators, $a^\dagger_{\mathbf{k}\lambda}, a_{\mathbf{k}\lambda}$ respectively, which refer to the creation and annihilation of photons in the reservoir field with mode $\mathbf{k}$ and polarisation λ. This field term in the Hamiltonian is given by

$$H_\mathrm{f} = \sum_{\mathbf{k},\lambda} \hbar\omega_\mathbf{k} a^\dagger_{\mathbf{k}\lambda} a_{\mathbf{k}\lambda}, \tag{2.22}$$

where the zero-point energy is neglected, and counts the number of photons with each momentum $\mathbf{k}$ and polarisation $\epsilon_{\mathbf{k}\lambda}$, with $\lambda = 1, 2$, present in the bath. These operators obey the bosonic commutation relation $[a_{\mathbf{k}\lambda}, a^\dagger_{\mathbf{k}'\lambda'}] = \delta_{\mathbf{k}\mathbf{k}'}\delta_{\lambda\lambda'}$, which means that different modes of light do not interact with each other [84].

Now, in order to write the interaction term between atom and field in terms of atomic and field operators [79], we write the dipole moment for an atom as:

$$\mathbf{D} = \sum_{i,j} |i\rangle\langle i|\mathbf{D}|j\rangle\langle j| = \sum_{i,j} \mathbf{d}_{ij}\sigma_{ij}, \tag{2.23}$$

where $\mathbf{d}_{ij} = \langle i|\mathbf{D}|j\rangle$ is the electric dipole transition matrix element associated with the transition from the atomic eigenstate $|j\rangle$ to $|i\rangle$, and $\sigma_{ij} = |i\rangle\langle j|$. These matrix elements are related to the Einstein coefficient (spontaneous emission rate) for the given transition [85]. We take an ensemble of identical atoms and we consider all dipole moments to be identical. For a two-level atom, we are restricted to $i, j = e, g$, and $\langle i|\mathbf{D}|i\rangle = 0$ due to parity. Therefore, $\mathbf{D} = \mathbf{d}^*\sigma_+ + \mathbf{d}\sigma_-$, where $\mathbf{d}_{ge} = \langle g|\mathbf{D}|e\rangle = (\langle e|\mathbf{D}|g\rangle)^* = \mathbf{d}$. The electric field, which is time-independent in our chosen reference frame, can be written as

$$\mathbf{E}(\mathbf{r}_\alpha) = \mathrm{i}\sum_{\mathbf{k},\lambda} \left(\hat{\epsilon}_{\mathbf{k}\lambda}\xi_\mathbf{k} a_{\mathbf{k}\lambda} \mathrm{e}^{\mathrm{i}\mathbf{k}\cdot\mathbf{r}_\alpha} - \mathrm{H.c.}\right), \tag{2.24}$$

with the direction of polarisation defined as $\hat{\epsilon}_{\mathbf{k}\lambda}$ and $\xi_\mathbf{k} = \sqrt{\hbar\omega_\mathbf{k}/(2\epsilon_0\mathcal{V})}$. In this expression, $\mathcal{V}$ is the quantisation volume which encloses the vector potential. If we assume that the dipole moment is real $\mathbf{d} = \mathbf{d}^*$ [86], the interaction Hamiltonian becomes

$$V = -\sum_{\alpha=1}^{N} \mathbf{D}\cdot\mathbf{E}(\mathbf{r}_\alpha) = -\mathrm{i}\hbar\sum_{\alpha=1}^{N}\sum_{\mathbf{k},\lambda}(\sigma^\alpha_+ + \sigma^\alpha_-)\left(g_{\mathbf{k}\lambda}a_{\mathbf{k}\lambda}\mathrm{e}^{\mathrm{i}\mathbf{k}\cdot\mathbf{r}_\alpha} - g^*_{\mathbf{k}\lambda}a^\dagger_{\mathbf{k}\lambda}\mathrm{e}^{-\mathrm{i}\mathbf{k}\cdot\mathbf{r}_\alpha}\right), \tag{2.25}$$

where $g_{\mathbf{k}\lambda} = \frac{\mathbf{d}\cdot\hat{\epsilon}_{\mathbf{k}\lambda}\xi_\mathbf{k}}{\hbar}$ is the coupling strength between the system and the reservoir.

Together, these terms provide us with the Hamiltonian

$$H = \sum_{\alpha=1}^{N} \frac{\hbar\omega_{\rm a}\sigma_z^\alpha}{2} + \sum_{\mathbf{k},\lambda} \hbar\omega_{\mathbf{k}}(a_{\mathbf{k}\lambda}a_{\mathbf{k}\lambda}^\dagger) \\ - {\rm i}\hbar\sum_{\alpha=1}^{N}\sum_{\mathbf{k},\lambda}(\sigma_+^\alpha + \sigma_-^\alpha)\left(g_{\mathbf{k}\lambda}a_{\mathbf{k}\lambda}{\rm e}^{{\rm i}\mathbf{k}\cdot\mathbf{r}_\alpha} - g_{\mathbf{k}\lambda}^* a_{\mathbf{k}\lambda}^\dagger {\rm e}^{-{\rm i}\mathbf{k}\cdot\mathbf{r}_\alpha}\right), \tag{2.26}$$

for an ensemble of two-level atoms interacting with a reservoir field.

To calculate the system master equation in the interaction picture [Eq. (2.8)], we must now rotate the basis, first with respect to the atomic Hamiltonian such that $\sigma_\alpha^\pm(t) = U_{\rm a}^\dagger(t)\sigma_\alpha^\pm U_{\rm a}(t) = {\rm e}^{\pm{\rm i}\omega_{\rm a}t}\sigma_\alpha^\pm$, and then with respect to the field Hamiltonian $a_{\mathbf{k}\lambda}(t) = U_{\rm f}^\dagger(t)a_{\mathbf{k}\lambda}U_{\rm f}(t) = {\rm e}^{-{\rm i}\omega_{\mathbf{k}}t}a_{\mathbf{k}\lambda}$, where $U_{\rm a}(t) = {\rm e}^{-{\rm i}H_{\rm a}t/\hbar}$ and $U_{\rm f} = {\rm e}^{-{\rm i}H_{\rm f}t/\hbar}$ are unitary operators. The interaction now becomes time-dependent

$$\begin{aligned} V_I(t) &= -{\rm i}\hbar\sum_{\alpha=1}^{N}\sum_{\mathbf{k},\lambda}(\sigma_+^\alpha{\rm e}^{{\rm i}\omega_{\rm a}t} + \sigma_-^\alpha{\rm e}^{-{\rm i}\omega_{\rm a}t})\left[g_{\mathbf{k}\lambda}a_{\mathbf{k}\lambda}{\rm e}^{{\rm i}(\mathbf{k}\cdot\mathbf{r}_\alpha-\omega_{\mathbf{k}}t)} - g_{\mathbf{k}\lambda}^* a_{\mathbf{k}\lambda}^\dagger{\rm e}^{-{\rm i}(\mathbf{k}\cdot\mathbf{r}_\alpha-\omega_{\mathbf{k}}t)}\right] \\ &= -\hbar\sum_{\alpha=1}^{N}\sum_{\mathbf{k},\lambda}A_\alpha(t)\left[B_{\alpha,\mathbf{k}\lambda}(t)a_{\mathbf{k}\lambda} + B_{\alpha,\mathbf{k}\lambda}^*(t)a_{\mathbf{k}\lambda}^\dagger\right], \end{aligned} \tag{2.27}$$

where $A_\alpha(t) = \sigma_+^\alpha{\rm e}^{{\rm i}\omega_{\rm a}t} + \sigma_-^\alpha{\rm e}^{-{\rm i}\omega_{\rm a}t}$ contains the terms dependent on the atomic operators, and $B_{\alpha,\mathbf{k}\lambda}(t) = {\rm i}g_{\mathbf{k}\lambda}{\rm e}^{{\rm i}(\mathbf{k}\cdot\mathbf{r}_\alpha-\omega_{\mathbf{k}}t)}$ is the coefficient of the field operator $a_{\mathbf{k}\lambda}$.

Since the atomic and field operators commute, we are able to extract the field operators and perform the trace over these degrees of freedom. The various combinations of ordering for the two interaction Hamiltonian factors $V_I(t)$ and $V_I(t-\tau)$ [Eq. (2.8)] provide us with expectation values of pairs of field operators

$$\begin{aligned} \langle a_{\mathbf{k}\lambda}a_{\mathbf{k}'\lambda'}^\dagger\rangle &= \delta_{\mathbf{k}\mathbf{k}'}\delta_{\lambda\lambda'}(\bar{n}_{\omega_{\mathbf{k}}}+1), \\ \langle a_{\mathbf{k}\lambda}^\dagger a_{\mathbf{k}'\lambda'}\rangle &= \delta_{\mathbf{k}\mathbf{k}'}\delta_{\lambda\lambda'}\bar{n}_{\omega_{\mathbf{k}}}, \\ \langle a_{\mathbf{k}\lambda}^\dagger a_{\mathbf{k}'\lambda'}^\dagger\rangle &= \langle a_{\mathbf{k}\lambda}a_{\mathbf{k}'\lambda'}\rangle = 0. \end{aligned} \tag{2.28}$$

Here, $\bar{n}_{\omega_{\mathbf{k}}}$ is the mean occupation for a mode of frequency, $\omega_{\mathbf{k}}$. For these calculations, we are modelling the reservoir field as a thermal bath, such that the number of photons of a given frequency is determined by a Boltzmann distribution. Recalling that we are only interested in transitions within the optical regime, we find that the bath contains approximately zero optical modes, $\bar{n}_{\omega_{\mathbf{k}}} \approx 0$, therefore $\langle a_{\mathbf{k}\lambda}a_{\mathbf{k}'\lambda'}^\dagger\rangle \approx \delta_{\mathbf{k}\mathbf{k}'}\delta_{\lambda\lambda'}$ is the

only non-zero expectation value. We neglect the remaining terms and find

$$\dot{\rho} = \int_0^\infty \mathrm{d}\tau \sum_{\alpha,\beta=1}^{N} \sum_{\substack{\mathbf{k},\mathbf{k}' \\ \lambda,\lambda'}} \Bigg\{ \delta_{\mathbf{k}\mathbf{k}'}\delta_{\lambda\lambda'} B_{\alpha,\mathbf{k}\lambda}(t) B^*_{\beta,\mathbf{k}'\lambda'}(t-\tau) \\ \times \left[A_\beta(t-\tau)\rho A_\alpha(t) - A_\alpha(t)A_\beta(t-\tau)\rho\right] + \mathrm{H.c.}\Bigg\}. \tag{2.29}$$

The pairs of operators $A_\alpha(t)$ and $A_\beta(t-\tau)$ create four terms from the various combinations of the atomic raising and lowering operators. For example,

$$A_\alpha(t)A_\beta(t-\tau)\rho = \Big[\sigma_+^\alpha\sigma_+^\beta \mathrm{e}^{\mathrm{i}\omega_\mathrm{a}(2t-\tau)} + \sigma_+^\alpha\sigma_-^\beta \mathrm{e}^{\mathrm{i}\omega_\mathrm{a}\tau} \\ + \sigma_-^\alpha\sigma_+^\beta \mathrm{e}^{-\mathrm{i}\omega_\mathrm{a}\tau} + \sigma_-^\alpha\sigma_-^\beta \mathrm{e}^{-\mathrm{i}\omega_\mathrm{a}(2t-\tau)}\Big]\rho. \tag{2.30}$$

At this stage, we make the secular approximation and neglect the fast oscillating terms that do not conserve energy ($\sigma_+^\alpha\sigma_+^\beta$ and $\sigma_-^\alpha\sigma_-^\beta$ terms)

$$A_\alpha(t)A_\beta(t-\tau)\rho \approx \left(\sigma_+^\alpha\sigma_-^\beta \mathrm{e}^{\mathrm{i}\omega_\mathrm{a}\tau} + \sigma_-^\alpha\sigma_+^\beta \mathrm{e}^{-\mathrm{i}\omega_\mathrm{a}\tau}\right)\rho, \tag{2.31}$$

and using that $B_{\alpha,\mathbf{k}\lambda}(t)B^*_{\beta,\mathbf{k}\lambda}(t-\tau) = |g_{\mathbf{k}\lambda}|^2 \mathrm{e}^{\mathrm{i}\mathbf{k}\cdot\mathbf{r}_{\alpha\beta}}\mathrm{e}^{-\mathrm{i}\omega_\mathbf{k}\tau}$, we write

$$\dot{\rho} = \int_0^\infty \mathrm{d}\tau \sum_{\alpha,\beta=1}^{N} \sum_{\mathbf{k},\lambda} \Bigg(|g_{\mathbf{k}\lambda}|^2 \mathrm{e}^{\mathrm{i}\mathbf{k}\cdot\mathbf{r}_{\alpha\beta}} \Big\{ \mathrm{e}^{-\mathrm{i}(\omega_\mathbf{k}-\omega_\mathrm{a})\tau}\left[\sigma_-^\beta\rho\sigma_+^\alpha - \sigma_+^\alpha\sigma_-^\beta\rho\right] \\ + \mathrm{e}^{-\mathrm{i}(\omega_\mathbf{k}+\omega_\mathrm{a})\tau}\left[\sigma_+^\beta\rho\sigma_-^\alpha - \sigma_-^\alpha\sigma_+^\beta\rho\right] \Big\} + \mathrm{H.c.}\Bigg). \tag{2.32}$$

We are now able to perform the time integral over τ using the Heitler function

$$\int_0^\infty \mathrm{d}\tau\ \mathrm{e}^{-\mathrm{i}(\omega_\mathbf{k}\pm\omega_\mathrm{a})\tau} = \pi\delta(\omega_\mathbf{k}\pm\omega_\mathrm{a}) - \mathrm{i}\mathcal{P}\frac{1}{\omega_\mathbf{k}\pm\omega_\mathrm{a}}, \tag{2.33}$$

where $\mathcal{P}$ represents the Cauchy Principal Value, such that one finds

$$\dot{\rho} = \sum_{\alpha,\beta=1}^{N} \sum_{\mathbf{k},\lambda} \Bigg(|g_{\mathbf{k}\lambda}|^2 \mathrm{e}^{\mathrm{i}\mathbf{k}\cdot\mathbf{r}_{\alpha\beta}} \Big\{ \left[\pi\delta(\omega_\mathbf{k}-\omega_\mathrm{a}) - \mathrm{i}\mathcal{P}\frac{1}{\omega_\mathbf{k}-\omega_\mathrm{a}}\right]\left[\sigma_-^\beta\rho\sigma_+^\alpha - \sigma_+^\alpha\sigma_-^\beta\rho\right] \\ + \left[\pi\delta(\omega_\mathbf{k}+\omega_\mathrm{a}) - \mathrm{i}\mathcal{P}\frac{1}{\omega_\mathbf{k}+\omega_\mathrm{a}}\right]\left[\sigma_+^\beta\rho\sigma_-^\alpha - \sigma_-^\alpha\sigma_+^\beta\rho\right] \Big\} + \mathrm{H.c.}\Bigg). \tag{2.34}$$

The next step requires us to take the summation over all modes of the reservoir field. In the limit of infinitesimally small spacing between modes, the summation is replaced

by the integral

$$\sum_{\mathbf{k}} \to \frac{\mathcal{V}}{(2\pi)^3} \int_0^\infty \mathrm{d}|\mathbf{k}| \int_0^\pi \mathrm{d}\theta \int_0^{2\pi} \mathrm{d}\phi \, |\mathbf{k}|^2 \sin\theta, \tag{2.35}$$

where $|\mathbf{k}| = \omega_{\mathbf{k}}/c$. This step is justified since we are assuming that all modes of the field have a momentum taken from a continuous distribution. Next, we want to perform the summation over the polarisation modes. The coupling strength can be expressed as

$$\sum_{\lambda} |g_{\mathbf{k}\lambda}|^2 = \frac{|\mathbf{d}|^2 \omega_{\mathbf{k}}}{2\hbar\epsilon_0 \mathcal{V}} \sum_{\lambda=1,2} (\hat{\mathbf{d}} \cdot \hat{\epsilon_{\mathbf{k}\lambda}})^2. \tag{2.36}$$

The two polarisation directions must be orthogonal to the momentum direction, and to each other, therefore for a given momentum we have $(\hat{\mathbf{d}}\cdot\hat{\mathbf{k}})^2+(\hat{\mathbf{d}}\cdot\hat{\epsilon}_{\mathbf{k}1})^2+(\hat{\mathbf{d}}\cdot\hat{\epsilon}_{\mathbf{k}2})^2 = 1$, such that

$$\sum_{\lambda=1,2} (\hat{\mathbf{d}} \cdot \hat{\epsilon}_{\mathbf{k}\lambda})^2 = 1 - (\hat{\mathbf{d}} \cdot \hat{\mathbf{k}})^2. \tag{2.37}$$

We assume that the atomic dipole moments are aligned with the quantisation axis (see Fig. 2.1) such that $(\hat{\mathbf{d}} \cdot \hat{\mathbf{k}})^2 = \cos^2\theta$, hence

$$\sum_{\lambda} |g_{\mathbf{k}\lambda}|^2 = \frac{|\mathbf{d}|^2 \omega_k}{2\hbar\epsilon_0 \mathcal{V}} \sin^2\theta. \tag{2.38}$$

Extracting the constants from the integrals, the master equation becomes

$$\begin{aligned} \dot{\rho} = \sum_{\alpha,\beta=1}^{N} \Bigg(& \frac{|\mathbf{d}|^2}{16\pi^3\hbar\epsilon_0 c^3} \int_0^\infty \mathrm{d}\omega_{\mathbf{k}} \int_0^\pi \mathrm{d}\theta \int_0^{2\pi} \mathrm{d}\phi \, \omega_{\mathbf{k}}^3 \sin^3\theta \mathrm{e}^{\mathrm{i}\mathbf{k}\cdot\mathbf{r}_{\alpha\beta}} \\ & \times \Bigg\{ \left[\pi\delta(\omega_{\mathbf{k}} - \omega_{\mathrm{a}}) - \mathrm{i}\mathcal{P}\frac{1}{\omega_{\mathbf{k}} - \omega_{\mathrm{a}}} \right] \left[\sigma_-^\beta \rho \sigma_+^\alpha - \sigma_+^\alpha \sigma_-^\beta \rho \right] \\ & + \left[\pi\delta(\omega_{\mathbf{k}} + \omega_{\mathrm{a}}) - \mathrm{i}\mathcal{P}\frac{1}{\omega_{\mathbf{k}} + \omega_{\mathrm{a}}} \right] \left[\sigma_+^\beta \rho \sigma_-^\alpha - \sigma_-^\alpha \sigma_+^\beta \rho \right] \Bigg\} + \mathrm{H.c.} \Bigg), \end{aligned} \tag{2.39}$$

which can be simplified further by including the Hermitian adjoint. Firstly, we sepa-

rate the delta functions from the Cauchy principal integrals,

$$\begin{aligned}\dot{\rho} = &\sum_{\alpha,\beta=1}^{N}\left(\frac{|\mathbf{d}|^2}{8\pi^2\hbar\epsilon_0 c^3}\int_0^\infty \mathrm{d}\omega_{\mathbf{k}}\int_0^\pi \mathrm{d}\theta\int_0^{2\pi}\mathrm{d}\phi\;\omega_{\mathbf{k}}^3\sin^3\theta \mathrm{e}^{\mathrm{i}\mathbf{k}\cdot\mathbf{r}_{\alpha\beta}}\right.\\
&\times\left\{\delta(\omega_{\mathbf{k}}-\omega_{\mathrm{a}})\left[\sigma_-^\beta\rho\sigma_+^\alpha-\frac{1}{2}\left\{\sigma_+^\alpha\sigma_-^\beta,\rho\right\}\right]\right.\\
&\left.\left.+\delta(\omega_{\mathbf{k}}+\omega_{\mathrm{a}})\left[\sigma_+^\beta\rho\sigma_-^\alpha-\frac{1}{2}\left\{\sigma_-^\alpha\sigma_+^\beta,\rho\right\}\right]\right\}\right)\\
&+\sum_{\alpha,\beta=1}^{N}\left(\frac{\mathrm{i}|\mathbf{d}|^2}{16\pi^3\hbar\epsilon_0 c^3}\mathcal{P}\int_0^\infty \mathrm{d}\omega_{\mathbf{k}}\int_0^\pi \mathrm{d}\theta\int_0^{2\pi}\mathrm{d}\phi\;\omega_{\mathbf{k}}^3\sin^3\theta \mathrm{e}^{\mathrm{i}\mathbf{k}\cdot\mathbf{r}_{\alpha\beta}}\right.\\
&\left.\times\left\{\frac{\left[\sigma_+^\alpha\sigma_-^\beta,\rho\right]}{\omega_{\mathbf{k}}-\omega_{\mathrm{a}}}+\frac{\left[\sigma_-^\alpha\sigma_+^\beta,\rho\right]}{\omega_{\mathbf{k}}+\omega_{\mathrm{a}}}\right\}\right),\end{aligned}\tag{2.40}$$

where $\{a,b\}=ab+ba$ is the anti-commutator. We then effectuate the delta functions, which removes half of the terms within the first set of integrals, since $-\omega_{\mathrm{a}}$ does not lie within the integral limits, and then we consider the integral over the solid angle

$$I_{\theta\phi}(\omega,\mathbf{r}_{\alpha\beta})=\int_0^{2\pi}\mathrm{d}\phi\int_0^\pi \mathrm{d}\theta\;\sin^3\theta \mathrm{e}^{ib_{\alpha\beta}(\sin\theta\cos\phi r_x+\sin\theta\sin\phi r_y+\cos\theta r_z)},\tag{2.41}$$

where $b_{\alpha\beta}=\omega_{\mathbf{k}}|\mathbf{r}_{\alpha\beta}|/c$ and r_x,r_y,r_z are the weights of the unit vector $\hat{\mathbf{r}}_{\alpha\beta}$. This integral is not easily solvable analytically or computationally. Therefore, we consider a specific instance when $\mathbf{r}_{\alpha\beta}$ is oriented such that $r_x=0, r_y=0$ and $r_z=1$. The integral is simplified and can be solved returning

$$I_{\theta\phi}^z(\omega,\mathbf{r}_{\alpha\beta})=\int_0^{2\pi}\mathrm{d}\phi\int_0^\pi \mathrm{d}\theta\;\sin^3\theta \mathrm{e}^{ib_{\alpha\beta}\cos\theta}=\frac{8\pi(\sin b_{\alpha\beta}-b_{\alpha\beta}\cos b_{\alpha\beta})}{b_{\alpha\beta}^3}.\tag{2.42}$$

In a similar way, for the cases $r_x=1,r_y=0,r_z=0$ and $r_x=0,r_y=1,r_z=0$, we find

$$I_{\theta\phi}^x(\omega,\mathbf{r}_{\alpha\beta})=\int_0^{2\pi}\mathrm{d}\phi\int_0^\pi \mathrm{d}\theta\;\sin^3\theta \mathrm{e}^{ib_{\alpha\beta}\sin\theta\cos\phi}=\frac{4\pi[b_{\alpha\beta}\cos b_{\alpha\beta}+(b_{\alpha\beta}^2-1)\sin b_{\alpha\beta}]}{b_{\alpha\beta}^3},\tag{2.43}$$

and

$$I_{\theta\phi}^y(\omega,\mathbf{r}_{\alpha\beta})=\int_0^{2\pi}\mathrm{d}\phi\int_0^\pi \mathrm{d}\theta\;\sin^3\theta \mathrm{e}^{ib_{\alpha\beta}\sin\theta\sin\phi}=\frac{4\pi[b_{\alpha\beta}\cos b_{\alpha\beta}+(b_{\alpha\beta}^2-1)\sin b_{\alpha\beta}]}{b_{\alpha\beta}^3}.\tag{2.44}$$

Using these results, we must find a solution that reduces to these three equations in the correct limits. Since $I_{\theta\phi}^x=I_{\theta\phi}^y$, we know that the solution is independent of the

azimuthal angle ϕ, and the equation changes as a function of the polar angle θ. This behaviour is incorporated by introducing factors of $(\hat{\mathbf{d}} \cdot \hat{\mathbf{r}}_{\alpha\beta})^2$, and the solution is

$$I_{\theta\phi}(\omega, \mathbf{r}_{\alpha\beta}) = 4\pi \left[q_{\alpha\beta} \frac{\sin b_{\alpha\beta}}{b_{\alpha\beta}} + p_{\alpha\beta} \left(\frac{\cos b_{\alpha\beta}}{b_{\alpha\beta}^2} - \frac{\sin b_{\alpha\beta}}{b_{\alpha\beta}^3} \right) \right] = 4\pi f(\omega, \mathbf{r}_{\alpha\beta}), \quad (2.45)$$

using the definitions $q_{\alpha\beta} = 1 - (\hat{\mathbf{d}} \cdot \hat{\mathbf{r}}_{\alpha\beta})^2$ and $p_{\alpha\beta} = 1 - 3(\hat{\mathbf{d}} \cdot \hat{\mathbf{r}}_{\alpha\beta})^2$. This result further simplifies the master equation

$$\begin{aligned} \dot{\rho} = & \sum_{\alpha,\beta=1}^{N} \frac{3\gamma}{2} f(\omega_{\mathrm{a}}, \mathbf{r}_{\alpha\beta}) \left[\sigma_-^\beta \rho \sigma_+^\alpha - \frac{1}{2} \left\{ \sigma_+^\alpha \sigma_-^\beta, \rho \right\} \right] + \\ & \sum_{\alpha,\beta=1}^{N} \frac{3\mathrm{i}\gamma}{4\pi\omega_{\mathrm{a}}^3} \mathcal{P} \int_0^\infty \mathrm{d}\omega_{\mathbf{k}}\, \omega_{\mathbf{k}}^3 f(\omega_{\mathbf{k}}, \mathbf{r}_{\alpha\beta}) \left(\frac{\left[\sigma_+^\alpha \sigma_-^\beta, \rho \right]}{\omega_{\mathbf{k}} - \omega_{\mathrm{a}}} + \frac{\left[\sigma_-^\alpha \sigma_+^\beta, \rho \right]}{\omega_{\mathbf{k}} + \omega_{\mathrm{a}}} \right), \end{aligned} \quad (2.46)$$

and we can now see the dependence on the single atom decay rate

$$\gamma = \frac{|\mathbf{d}|^2 \omega_{\mathrm{a}}^3}{3\pi\hbar\epsilon_0 c^3}. \quad (2.47)$$

The commutators in the second summation are manipulated by first swapping the atomic indices in the second term. Since $f(\omega_{\mathbf{k}}, \mathbf{r}_{\alpha\beta})$ is symmetric under swapping of α and β, this factor is unchanged and we have $\left[\sigma_-^\alpha \sigma_+^\beta, \rho \right] \to \left[\sigma_-^\beta \sigma_+^\alpha, \rho \right]$. We then use the commutation relation for raising and lowering operators $\left[\sigma_+^\alpha, \sigma_-^\beta \right] = \delta_{\alpha\beta} \sigma_z^\alpha$ to divide the summation over atomic indices into a summation for self interactions ($\alpha = \beta$) and one for pairs of atoms ($\alpha \neq \beta$). For $\alpha = \beta$, we recall that $\sigma_+^\alpha \sigma_-^\alpha = (\sigma_z^\alpha + \mathbb{1}^\alpha)/2$, and for $\mathbf{r}_{\alpha\beta} \to \mathbf{0}$, $f(\omega_{\mathbf{k}}, \mathbf{r}_{\alpha\beta}) \to 1$. When $\alpha \neq \beta$, the operators commute, and we are able to swap their positions. The commutator can be extracted from the integral and combining the two fractions, by making the substituion $\omega_{\mathbf{k}} \to -\omega_{\mathbf{k}}$ in the second term, provides

$$\begin{aligned} \dot{\rho} = & \sum_{\alpha,\beta=1}^{N} \frac{3\gamma}{2} f(\omega_{\mathrm{a}}, \mathbf{r}_{\alpha\beta}) \left[\sigma_-^\beta \rho \sigma_+^\alpha - \frac{1}{2} \left\{ \sigma_+^\alpha \sigma_-^\beta, \rho \right\} \right] \\ & + \sum_{\alpha=1}^{N} \frac{3\mathrm{i}\gamma}{4\pi\omega_{\mathrm{a}}^2} \mathcal{P} \int_0^\infty \mathrm{d}\omega_{\mathbf{k}}\, \frac{\omega_{\mathbf{k}}^3}{\omega_{\mathbf{k}}^2 - \omega_{\mathrm{a}}^2} \left[\sigma_z^\alpha, \rho \right] \\ & + \sum_{\alpha\neq\beta}^{N} \frac{3\mathrm{i}\gamma}{4\pi\omega_{\mathrm{a}}^3} \mathcal{P} \int_{-\infty}^\infty \mathrm{d}\omega_{\mathbf{k}}\, \frac{\omega_{\mathbf{k}}^3 f(\omega_{\mathbf{k}}, \mathbf{r}_{\alpha\beta})}{\omega_{\mathbf{k}} - \omega_{\mathrm{a}}} \left[\sigma_+^\alpha \sigma_-^\beta, \rho \right]. \end{aligned} \quad (2.48)$$

The self-interaction term represents the divergent Lamb shift. This shift in the energy levels, while tending to infinity, is equivalent for all atoms and can be absorbed into

the system Hamiltonian by a rescaling of the energy levels [7]. We therefore neglect this term from our master equation. The Cauchy principal value of the second integral is calculated to be [12]

$$\mathcal{P}\int_{-\infty}^{\infty}\mathrm{d}\omega_{\mathbf{k}}\,\frac{\omega_{\mathbf{k}}^{3}}{\omega_{\mathbf{k}}-\omega_{\mathrm{a}}}f(\omega_{\mathbf{k}},\mathbf{r}_{\alpha\beta})=\pi\omega_{\mathrm{a}}^{3}g(\omega_{\mathrm{a}},\mathbf{r}_{\alpha\beta}), \tag{2.49}$$

with

$$g(\omega_{\mathrm{a}},\mathbf{r}_{\alpha\beta})=q_{\alpha\beta}\frac{\cos b_{\alpha\beta}}{b_{\alpha\beta}}-p_{\alpha\beta}\left(\frac{\sin b_{\alpha\beta}}{b_{\alpha\beta}^{2}}+\frac{\cos b_{\alpha\beta}}{b_{\alpha\beta}^{3}}\right). \tag{2.50}$$

Therefore, the master equation for an N-body system of two-level atoms interacting with a reservoir electromagnetic radiation field is

$$\dot{\rho}=\sum_{\alpha,\beta=1}^{N}\left\{\Gamma_{\alpha\beta}\left[\sigma_{-}^{\beta}\rho\sigma_{+}^{\alpha}-\frac{1}{2}\left\{\sigma_{+}^{\alpha}\sigma_{-}^{\beta},\rho\right\}\right]-\mathrm{i}V_{\alpha\beta}|_{\alpha\neq\beta}\left[\sigma_{+}^{\alpha}\sigma_{-}^{\beta},\rho\right]\right\}, \tag{2.51}$$

where we define

$$\Gamma_{\alpha\beta}=\frac{3\gamma}{2}f(\omega_{\mathrm{a}},\mathbf{r}_{\alpha\beta})=\frac{3\gamma}{2}\left[q_{\alpha\beta}\frac{\sin b_{\alpha\beta}}{b_{\alpha\beta}}+p_{\alpha\beta}\left(\frac{\cos b_{\alpha\beta}}{b_{\alpha\beta}^{2}}-\frac{\sin b_{\alpha\beta}}{b_{\alpha\beta}^{3}}\right)\right], \tag{2.52}$$

$$V_{\alpha\beta}=\frac{-3\gamma}{4}g(\omega_{\mathrm{a}},\mathbf{r}_{\alpha\beta})=\frac{-3\gamma}{4}\left[q_{\alpha\beta}\frac{\cos b_{\alpha\beta}}{b_{\alpha\beta}}-p_{\alpha\beta}\left(\frac{\sin b_{\alpha\beta}}{b_{\alpha\beta}^{2}}+\frac{\cos b_{\alpha\beta}}{b_{\alpha\beta}^{3}}\right)\right], \tag{2.53}$$

and we use the notation $V_{\alpha\beta}|_{\alpha\neq\beta}$ to imply that $V_{\alpha\alpha}=0$.

2.4 Collective behaviour

The master equation [Eq. (2.51)] can be rewritten as

$$\dot{\rho}=-\frac{\mathrm{i}}{\hbar}\left[H_{\mathrm{dd}},\rho\right]+\mathcal{D}(\rho). \tag{2.54}$$

Here, the Hamiltonian is

$$H_{\mathrm{dd}}=\sum_{\alpha\neq\beta}^{N}\hbar V_{\alpha\beta}\sigma_{+}^{\alpha}\sigma_{-}^{\beta}. \tag{2.55}$$

We refer to this as the coherent dipole-dipole interaction, which conserves the number of excitations. The second term in Eq. (2.54) reads

$$\mathcal{D}(\rho)=\sum_{\alpha\beta=1}^{N}\Gamma_{\alpha\beta}\left[\sigma_{-}^{\beta}\rho\sigma_{+}^{\alpha}-\frac{1}{2}\left\{\sigma_{+}^{\alpha}\sigma_{-}^{\beta},\rho\right\}\right], \tag{2.56}$$

and is responsible for collective dissipation in the system. From Eq. (2.51) and Eq. (2.54), we are immediately able to identify features of cooperativity by considering separately the coherent interaction term and the dissipator $\mathcal{D}(\rho)$.

2.4.1 Coherent interactions

We begin by analysing the coherent dipole-dipole interactions, and their strength, contained in $V_{\alpha\beta}$. In Fig. 2.2**(a)**, we sketch the interactions. The de-excitation of one atom (for instance, atom β) creates a virtual photon in the reservoir field, which can in turn be absorbed by a neighbouring atom (α). This process is labelled the dipole-dipole interaction, and is commonly referred to as a "flip-flop" interaction. The likelihood of this process occurring is given by $V_{\alpha\beta}$ and depends on two key parameters: the angle formed between the atomic dipole moment vector and the atomic separation vector [Fig. 2.2**(c)**], and the magnitude of the separation between atoms. $V_{\alpha\beta}$ tells us how strongly atom α couples to atom β as a function of the distance between them, as demonstrated in Fig. 2.2**(d)**. We can clearly see that, for various alignments of the atomic dipole moments, the coupling is strongest for small separations. In fact, this function diverges as $|\mathbf{r}_{\alpha\beta}| \to 0$. As the distance between atoms increases, the coupling strength oscillates and decays to zero. Therefore, for two atoms positioned such that their separation is much larger than the transition wavelength of the atoms ($2\pi/\lambda = \omega_{\mathrm{a}}/c$), the instantaneous exchange of a photon is incredibly unlikely. It is worth noting here that we do not consider retardation effects in these calculations. We assume that the exchange of a virtual photon always happens instantaneously, regardless of the atomic separation. In reality, one might consider the photon travelling over a finite time.

2.4.2 Collective dissipation

Next, we consider the dissipator containing the coefficients $\Gamma_{\alpha\beta}$. Its form is suggestive of a Lindblad dissipator, however this is not exactly the case, since the operators contain different indices α and β. In order to recreate the more familiar case, we proceed to diagonalise the matrix $\bar{\Gamma}$, which contains elements $\Gamma_{\alpha\beta}$, and we find $\bar{\Gamma}_D = \bar{M}^\dagger \bar{\Gamma} \bar{M}$. Here, $\bar{M}$ is a matrix containing the eigenvectors of $\bar{\Gamma}$, and $\bar{M}^\dagger$ is its adjoint. Likewise, we have $\bar{\Gamma} = \bar{M} \bar{\Gamma}_D \bar{M}^\dagger$, where we have utilised the identity $\bar{M}\bar{M}^\dagger = \mathbb{1}$ since $\bar{\Gamma}$ is a positive semi-definite matrix. Expanding $\bar{\Gamma}$ in terms of the diagonalised matrix, as a summation, we find

$$\Gamma_{\alpha\beta} = \sum_{m=1}^{N} M_{\alpha m} \Gamma_D^m M_{m\beta}^\dagger. \tag{2.57}$$

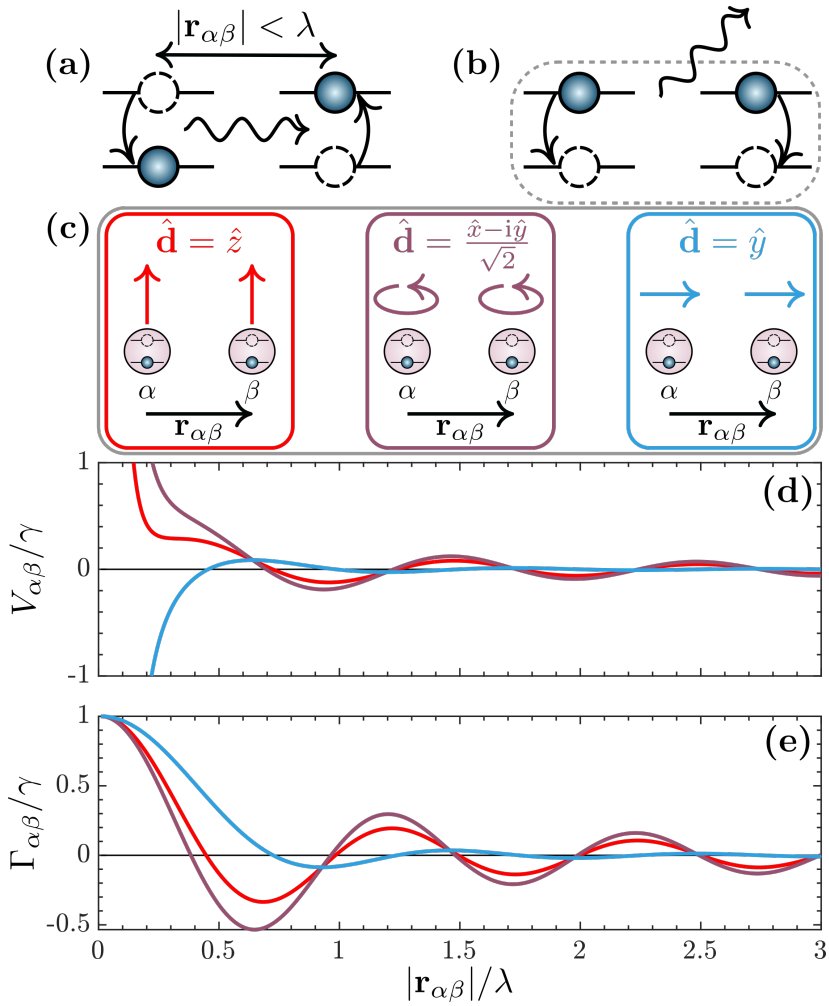

Figure 2.2: **Coherent interactions and dissipation.** A pair of two-level atoms display collective behaviour in the form of **(a)** photon exchange through dipole-dipole interactions, and **(b)** collective dissipation from the system, instead of single atom emission. The behaviour is enhanced for atomic separations that are comparable to, or smaller than, the transition wavelength associated with the two-level atom, $2\pi/\lambda = \omega_{\mathrm{a}}/c$. The collectivity observed is dependent on **(c)** the direction of the atomic dipole moments $\mathbf{d}$, with respect to the atomic separation vector $\mathbf{r}_{\alpha\beta}$, and the distance between the emitters. **(d)** highlights the coherent interaction matrix elements and **(e)** models the dissipation matrix elements, as a function of atomic separation, for three different dipole moment alignments: atom dipole moments perpendicular to their separation (red), circularly polarised dipole moments (purple), and atom dipole moments parallel to their separation (blue).

This expression is substituted into the dissipative term of the master equation

$$\begin{aligned}\mathcal{D}(\rho) &= \sum_{\alpha,\beta=1}^{N} \Gamma_{\alpha\beta}\left[\sigma_-^\beta \rho \sigma_+^\alpha - \frac{1}{2}\left\{\sigma_+^\alpha \sigma_-^\beta, \rho\right\}\right] \\ &= \sum_{\alpha,\beta=1}^{N}\sum_{m=1}^{N} M_{\alpha m}\Gamma_D^m M_{m\beta}^\dagger \left[\sigma_-^\alpha \rho \sigma_+^\beta - \frac{1}{2}\{\sigma_+^\alpha \sigma_-^\beta, \rho\}\right] \\ &= \sum_{m=1}^{N} \Gamma_D^m \Big\{ J_m \rho J_m^\dagger - \frac{1}{2}[J_m^\dagger J_m, \rho]\Big\},\end{aligned} \tag{2.58}$$

where we have defined the collective jump operators

$$J_m = \sum_{\alpha}^{N} \sigma_-^\alpha M_{\alpha m}, \qquad J_m^\dagger = \sum_{\alpha}^{N} M_{m\alpha}^\dagger \sigma_+^\alpha. \tag{2.59}$$

This now has the form of a Lindblad dissipator, where each m corresponds to a different collective mode of decay, with an associated rate Γ_D^m. These rates can be considered as the decay of excitation from the entire system, as opposed to a single atom within this system.

We demonstrate this for the simple case of two atoms in Fig. 2.2**(b)**; these modes are not specific to emission from a single atom within the ensemble, but to the collection as a whole. We can compare the collective decay rates to the single atom decay rate [Eq. (2.47)] and we find two interesting cases:

$$\begin{aligned}&\Gamma_D^m > \gamma : \text{supperradiant}, \\ &\Gamma_D^m < \gamma : \text{subradiant}.\end{aligned} \tag{2.60}$$

When the collective decay rates are larger than the single atom decay rate, we call the states superradiant, since they emit faster hence they have shorter lifetimes. On the other hand, when the rates are smaller than the single atom decay rate, the states are referred to as subradiant. The subradiant states are more slowly emitting and their corresponding decay rates can even approach values very close to zero. These are also called "dark states", due to the rarity of emission from the states and decoupling from the bath photons [87–90]. One can visualise super- and subradiance in a classical setting by considering that each atom emits a plane wave of light. The phenomenon of superradiance is explained here as the constructive interference of the multiple paths of light emitted from the ensemble, while subradiant behaviour is observed when the paths destructively interfere. Perfect destructive interference leads to the above mentioned "dark states", where no light emission is observed.

We can explore how collectivity in the decay rates becomes more prominent by taking the case of two atoms and observing how the off-diagonal elements of $\bar{\Gamma}$ vary

as a function of separation, as shown in Fig. 2.2**(e)**. If we consider the case where the atomic separation is very large, ($|\mathbf{r}_{\alpha\beta}| \to \infty$), and recalling Eq. (2.52), we find that $\Gamma_{\alpha\beta} \to 0$. The diagonal elements of this matrix are equal to the single atom decay rate, therefore in this case, the matrix of dissipation coefficients is already diagonal

$$\bar{\Gamma} = \begin{pmatrix} \gamma & 0 \\ 0 & \gamma \end{pmatrix} = \bar{\Gamma}_D, \tag{2.61}$$

thus the collective decay rates are $\Gamma_D^1 = \Gamma_D^2 = \gamma$. This result informs us that at very large separations the two atoms behave as independent emitters. We could identify this result intuitively, since the two emitters do not "see" each other when they are very far apart and we would not expect to see collectivity.

Now let us consider the converse case when the atoms are brought very close together. From Fig. 2.2**(e)**, we see that the off-diagonal elements approach $\Gamma_{\alpha\beta} = \gamma$ for $|\mathbf{r}_{\alpha\beta}| \to 0$ (which also justifies why the diagonal elements are equal to the single atom decay rate). This leads to

$$\bar{\Gamma} \approx \begin{pmatrix} \gamma & \gamma \\ \gamma & \gamma \end{pmatrix} \Rightarrow \bar{\Gamma}_D \approx \begin{pmatrix} 2\gamma & 0 \\ 0 & 0 \end{pmatrix}, \tag{2.62}$$

hence the collective rates in this case are $\Gamma_D^1 = 2\gamma$ and $\Gamma_D^2 = 0$. These correspond to the decay rates that we can achieve when the atoms are essentially on top of one another, where generally the most superradiant state takes the value $\Gamma_D^{\max} = N\gamma$ and the most subradiant state has $\Gamma_D^{\min} = 0$, for an ensemble of N atoms.

We can better understand the effect of having a many-body system with close spacing by extending the simple two atom case to $N = 10$ atoms in a one-dimensional (1D) chain. We define the dipole moments to be aligned perpendicular to the direction of the chain. The atoms are uniformly spaced with nearest neighbour separation $a \lesssim \lambda$. A matrix of coefficients $\Gamma_{\alpha\beta}$ is constructed for each value of α and β. By diagonalising this matrix, the collective decay rates are determined as a function of the atomic spacing. We demonstrate this in Fig. 2.3, for each mode of decay in ascending order from the most subradiant rate (black) to most superradiant (blue). We confirm here that in the limit where $a \to 0$, we have one superradiant mode with $\Gamma_D^m \to N\gamma$, and the remaining $N - 1$ modes are subradiant with $\Gamma_D^m = 0$. However, this limit is not a physical scenario to consider, since we cannot place the atoms directly on top of one another. As a/λ increases from 0 to 0.5, we gradually see the subradiant rates shift away from $\Gamma_D^m = 0$ one by one. The superradiant rate also decreases. These results once again confirm that the collective nature of the many-body system is highly dependent on the proximity of the atoms to each other. At each half integer value of a/λ we see a shift in the most subradiant modes, due to the periodic trigonometric

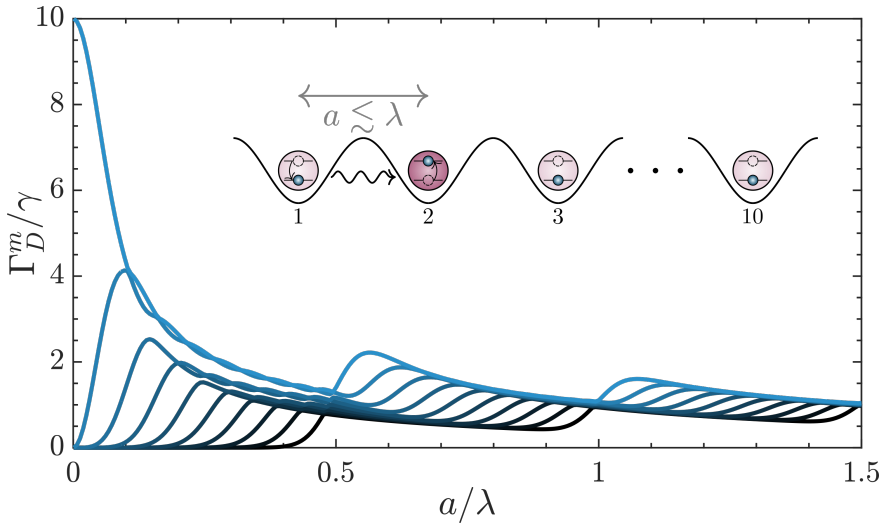

Figure 2.3: **Decay modes of a 1D atomic chain.** The decay rates for an $N = 10$ atomic chain with spacing a less than, or comparable to, the transition wavelength of the atoms, plotted as a function of atomic spacing. At each value of a/λ, there are N decay rates sorted into ascending order from most subradiant (black line) to most superradiant (lightest blue line), with the shade of the intermediate lines demonstrating the increase in decay rate.

functions in $\Gamma_{\alpha\beta}$ [Eq. (2.52)], and overall the curves are tending towards the single atom decay rate.

2.5 Laser driving

We have calculated a master equation that describes the evolution of many-body two-level systems, however this will only present interesting dynamics when there are excitations in the system; there is no process that mediates spontaneous absorption. We therefore explore laser driving techniques utilised in experiments for creating excitations within the atomic system, in order to observe collective behaviour and incorporate this into our model. This is a necessary step to model state preparation so that we can examine the different ways in which the system exhibits cooperative features [15, 16, 91].

In Sec. 2.2, we derived the Hamiltonian describing the interaction of an atom with an external field within the dipole approximation. Using this same form of interaction, we write the interaction due to a laser field as

$$H_{\mathrm{L}} = -\mathbf{D} \cdot \mathbf{E}_{\mathrm{L}}(t), \tag{2.63}$$

recalling that $\mathbf{D}$ is the dipole operator (defined in Sec. 2.3), and $\mathbf{E}_{\mathrm{L}}(t)$ is the laser field driving the system. In this case, we can define the electric field due to the laser

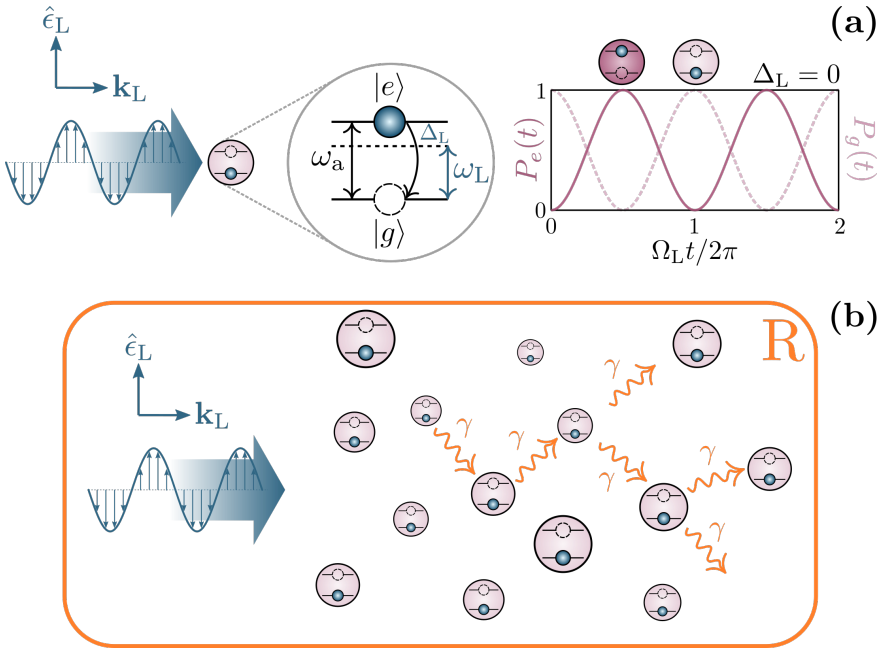

Figure 2.4: **Laser driving.** **(a)** A single two-level atom driven by a laser, with a frequency ω_L that is detuned from the atomic transition ω_a by $\Delta_L = \omega_L - \omega_a$, an electric field amplitude $\hat{\epsilon}_L$ aligned to the atomic dipole moment and laser momentum $\mathbf{k}_L$ perpendicular to this. Without dissipation, the atom has a probability of being excited $P_e(t)$ that smoothly oscillates (within the rotating wave approximation) from 0 to the maximal value of 1 (when $\Delta_L = 0$) at a frequency given by the Rabi frequency Ω_L. **(b)** The system is extended to a collection of two-level atoms that now interact with a reservoir field which introduces dissipation into the dynamics.

classically as $\mathbf{E}_L(t) = \mathbf{E}_0 \cos(\omega_L t)$, where $\mathbf{E}_0 = E_0 \hat{\epsilon}_L$ is the electric field amplitude of the laser and ω_L is the laser frequency. For a single two-level atom interacting with a laser field we can write the Hamiltonian as

$$H = \frac{1}{2}\hbar\omega_a\sigma_z - \hbar\Omega_L \cos(\omega_L t)(\sigma_+ + \sigma_-), \tag{2.64}$$

where $\Omega_L = \mathbf{d} \cdot \mathbf{E}_0/\hbar$ is the Rabi frequency describing the rate of excitation (and de-excitation) due to the laser driving (see Fig. 2.4**(a)**), and we have expanded the dipole operator in terms of atomic operators. We move to a rotating frame by applying the unitary transformation $U_L(t) = e^{i\omega_L\sigma_z t/2}$,

$$H'_L = U_L(t)HU_L^\dagger(t) - i\hbar U_L(t)\frac{\partial}{\partial t}U_L^\dagger(t). \tag{2.65}$$

We then make a rotating wave approximation, justified since $\omega_L \gg \Omega_L$, which allows us to neglect fast oscillating terms and the Hamiltonian becomes

$$H'_L = -\frac{\hbar}{2}\left[\Delta_L\sigma_z + \Omega_L(\sigma_+ + \sigma_-)\right], \tag{2.66}$$

where $\Delta_{\mathrm{L}} = \omega_{\mathrm{L}} - \omega_{\mathrm{a}}$ is the laser detuning. This well-known result can be found in many textbooks regarding light-matter interactions, for example Reference [79]. However, we are interested in the many-body case that is also interacting with a reservoir field, as depicted in Fig. 2.4**(b)**. When we have an ensemble of atoms, we must consider the spatial form of the laser field. For instance, we may excite the entire system uniformly (Chapter 5), or we may only wish to excite specific atoms within the ensemble (Chapter 3). By making the field amplitude spatially dependent, the Hamiltonian due to interaction with the laser becomes

$$H_{\mathrm{L}} = \sum_{\alpha=1}^{N} -\mathbf{D} \cdot \mathbf{E}_{\mathrm{L}}(\mathbf{r}_\alpha, t), \tag{2.67}$$

and using that the rotating wave approximation still holds in this example, the rotated Hamiltonian for the atomic and laser terms becomes

$$H'_{\mathrm{L}} = -\frac{\hbar}{2} \sum_{\alpha=1}^{N} \left\{ \Delta_{\mathrm{L}} \sigma_z^\alpha + \Omega_{\mathrm{L}} [\sigma_+^\alpha(\mathbf{r}_\alpha) + \sigma_-^\alpha(\mathbf{r}_\alpha)] \right\}. \tag{2.68}$$

In this definition, the atomic operators $\sigma_\alpha^{\pm}(\mathbf{r}_\alpha)$ contain factors that describe the spatial dependence of the laser field. We leave this in a general form for now, so that we can adapt it for specific cases in later sections. Note also that the spatial dependence from the laser field only appears on these particular operators, and does not affect the atomic operator behaviour. If we assume that the laser driving is chosen to be on-resonance with the atom transition ($\Delta_{\mathrm{L}} = 0$), we simplify the system Hamiltonian describing the laser drive to

$$H'_{\mathrm{L}} = -\frac{\hbar}{2} \sum_{\alpha=1}^{N} \Omega_{\mathrm{L}} [\sigma_+^\alpha(\mathbf{r}_\alpha) + \sigma_-^\alpha(\mathbf{r}_\alpha)]. \tag{2.69}$$

It can be shown through the derivation of the master equation that the laser Hamiltonian appears in the coherent interaction term [92] such that

$$\dot{\rho} = -\frac{\mathrm{i}}{\hbar} \left[\left(H'_{\mathrm{L}} + \sum_{\alpha \neq \beta}^{N} \hbar V_{\alpha\beta} \sigma_+^\alpha \sigma_-^\beta \right), \rho \right] + \sum_{\alpha,\beta=1}^{N} \Gamma_{\alpha\beta} \left[\sigma_-^\beta \rho \sigma_+^\alpha - \frac{1}{2} \left\{ \sigma_+^\alpha \sigma_-^\beta, \rho \right\} \right], \tag{2.70}$$

however we proceed in later chapters to simply use the result to explore the excitation process in our many-body system, due to the vastly complex nature of this derivation.

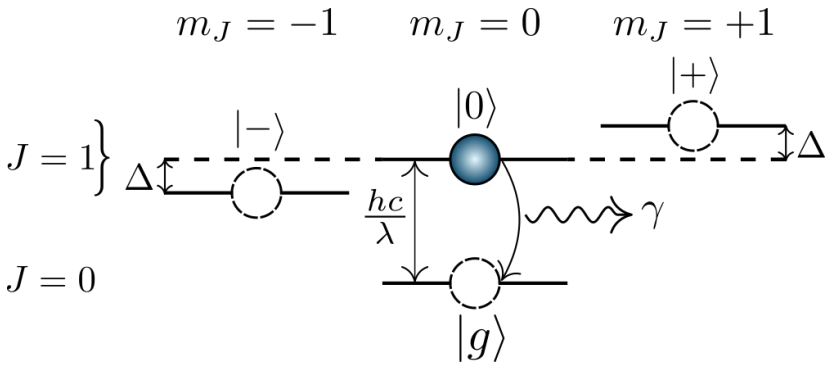

Figure 2.5: **Four-level atom.** We consider the following internal atomic levels in each atom: a ground state $|g\rangle$ and three degenerate excited states $|-\rangle, |0\rangle, |+\rangle$. $\pm, 0$ refer to the total angular momentum projections $m_J = \pm 1, 0$. The transition from ground state to any of these three levels has wavelength λ. The degeneracy is lifted by the shift of $|\pm\rangle$ by $\pm\Delta = \pm\mu_{\mathrm{B}} g\,|\mathbf{B}|$ when an external uniform magnetic field $\mathbf{B}$ is aligned with the dipole moment $\mathbf{d}^0$ of the $|g\rangle \to |0\rangle$ transition (quantisation axis). We assume that the level splitting Δ is small, such that the transition wavelengths to each excited state are still $\approx \lambda$.

2.6 Four-level atom master equation

2.6.1 The model

So far, we have demonstrated the emergence of collective behaviour and introduced laser driving techniques in simple systems of two-level atoms.

While two-level atoms are a good foundation for approximating the dynamics of such many-body systems, it may be more appropriate in some instances to instead model a collection of four-level atoms. This extension may be used as a more physical representation of atomic systems such as strontium atoms [14, 93, 94]. In contrast to the two-level system, our four-level atom contains one ground state and a three-fold degenerate excited state, as shown in Fig. 2.5. Modelling four-level atoms is necessary for spin systems containing one ground state with total orbital angular momentum $J = 0$, and an excited level with $J = 1$. The ground state has $m_J = 0$, which defines the projection of the total angular momentum in the quantisation axis, while the excited level with $J = 1$ has a three-fold degenerate splitting of the level. These three levels are distinguished by their unique projection along the quantisation axis $m_J = -1, 0, +1$ [82, 95]. This is exactly the case for the ${}^3P_0 - {}^3D_1$ transition that we introduced in Sec. 2.3.

This basis is related to the Cartesian basis by $|\mp\rangle = (\pm|x\rangle - \mathrm{i}|y\rangle)/\sqrt{2}$, and $|0\rangle = |z\rangle$, where the $m_J = \pm 1$ states are represented by their corresponding sign.

Generally, it is not necessary that $|g\rangle$ is the atomic ground state, however we do

consider that $|g\rangle$ has a near-infinite lifetime. Since the excited levels are degenerate, if a four-level atom absorbs a photon with frequency matching the transition frequency, depending on the polarisation of the light exciting the atom, any one of the three levels $|\pm, 0\rangle$ can be excited. For instance, circularly polarised light with components of the laser field amplitude in the x- and y-directions excites $|\pm\rangle$, whereas linearly polarised light with a laser field amplitude in the z-direction excites $|0\rangle$.

The derivation of the many-body system master equation follows a similar methodology to the two-level atom case, however now we have three possible transitions that can occur. The atomic operators in Eq. (2.27) are replaced with vector operators that allow the three transitions, $\mathbf{b}_\alpha$ and $\mathbf{b}'_\alpha$. These vectors contain the atomic lowering operators $b_\alpha^{\ i} = |g\rangle_\alpha\langle i|$ and raising operators $b_\alpha{}^{i\dagger} = |i\rangle_\alpha\langle g|$ which describe transitions between ground and excited states, with $i = \pm, 0$ and $\alpha = 1, \ldots, N$:

$$\mathbf{b}_\alpha = \begin{pmatrix} b_\alpha^{\ +} \\ b_\alpha^{\ 0} \\ b_\alpha^{\ -} \end{pmatrix} \quad \text{and} \quad \mathbf{b}'_\alpha = \begin{pmatrix} b_\alpha{}^{+\dagger} \\ b_\alpha{}^{0\dagger} \\ b_\alpha{}^{-\dagger} \end{pmatrix}. \tag{2.71}$$

The Hamiltonian for a system of four-level atoms interacting with an electromagnetic reservoir field is

$$\begin{aligned} H &= \hbar \sum_{\alpha=1}^{N} \omega_{\mathrm{a}} \mathbf{b}'_\alpha \cdot \mathbf{b}_\alpha + \hbar \sum_{\mathbf{k},\lambda} \omega_{\mathbf{k}} a^\dagger_{\mathbf{k}\lambda} a_{\mathbf{k}\lambda} \\ &\quad - \hbar \sum_{\alpha=1}^{N} \sum_{\mathbf{k},\lambda} (\mathbf{b}'_\alpha + \mathbf{b}_\alpha) \left(g_{\mathbf{k}\lambda} a_{\mathbf{k}\lambda} \mathrm{e}^{\mathrm{i}\mathbf{k}\cdot\mathbf{r}_\alpha} + g^*_{\mathbf{k}\lambda} a^\dagger_{\mathbf{k}\lambda} \mathrm{e}^{-\mathrm{i}\mathbf{k}\cdot\mathbf{r}_\alpha} \right) \\ &= H_{\mathrm{a}} + H_{\mathrm{f}} + V_I. \end{aligned} \tag{2.72}$$

2.6.2 The master equation

Analogous calculations to those made for the many-body two-level atom master equation are performed, now using the above initial Hamiltonian. The derivation of this master equation is outlined in Reference [86]. We will not perform this calculation here, since the relevant approximations and justifications made in the previous section still hold. The master equation, once again, takes the form of Eq. (2.54) but now with the coherent evolution described by the Hamiltonian

$$H_{\mathrm{dd}} = \hbar \sum_{\alpha \neq \beta}^{N} \mathbf{b}'_\alpha \cdot \bar{W}_{\alpha\beta} \mathbf{b}_\beta, \tag{2.73}$$

and the dissipator given as [35]

$$\mathcal{D}(\rho) = \sum_{\alpha,\beta=1}^{N} \left[\mathbf{b}_\alpha \cdot \bar{X}_{\alpha\beta} \rho \mathbf{b}'_\beta - \frac{1}{2}\{\mathbf{b}'_\alpha \cdot \bar{X}_{\alpha\beta} \mathbf{b}_\beta, \rho\} \right]. \tag{2.74}$$

By inspecting the Hamiltonian first, we see that the matrix $\bar{W}_{\alpha\beta}$ contains elements that determine the interaction between pairs of states on atoms α and β:

$$\bar{W}_{\alpha\beta} = \begin{pmatrix} W_{\alpha\beta}^{++} & W_{\alpha\beta}^{+0} & W_{\alpha\beta}^{+-} \\ W_{\alpha\beta}^{0+} & W_{\alpha\beta}^{00} & W_{\alpha\beta}^{0-} \\ W_{\alpha\beta}^{-+} & W_{\alpha\beta}^{-0} & W_{\alpha\beta}^{--} \end{pmatrix} = \begin{pmatrix} A_{\alpha\beta} & -C_{\alpha\beta}^{*} & B_{\alpha\beta} \\ -C_{\alpha\beta} & D_{\alpha\beta} & C_{\alpha\beta}^{*} \\ B_{\alpha\beta}^{*} & C_{\alpha\beta} & A_{\alpha\beta} \end{pmatrix}. \tag{2.75}$$

For example, the element $W_{\alpha\beta}^{+0}$ represents the interaction strength between the $m_J = 1$ excited state of atom α and the $m_J = 0$ excited state of atom β. The form of the interaction coefficients is determined in the same way that $V_{\alpha\beta}$ is for the coherent interaction between pairs of two-level atoms. The elements of $\bar{W}_{\alpha\beta}$ are

$$\begin{aligned}
A_{\alpha\beta} &= -\frac{3\gamma}{8}\left[(2-\sin^2\theta)\frac{\cos b_{\alpha\beta}}{b_{\alpha\beta}} - (2-3\sin^2\theta)\Big(\frac{\sin b_{\alpha\beta}}{b_{\alpha\beta}^2} + \frac{\cos b_{\alpha\beta}}{b_{\alpha\beta}^3}\Big)\right], \\
B_{\alpha\beta} &= -\frac{3\gamma}{8}\sin^2\theta \mathrm{e}^{-2\mathrm{i}\phi}\left[\frac{\cos b_{\alpha\beta}}{b_{\alpha\beta}} - 3\Big(\frac{\sin b_{\alpha\beta}}{b_{\alpha\beta}^2} + \frac{\cos b_{\alpha\beta}}{b_{\alpha\beta}^3}\Big)\right], \\
C_{\alpha\beta} &= -\frac{3\gamma}{8\sqrt{2}}\sin 2\theta \mathrm{e}^{\mathrm{i}\phi}\left[-\frac{\cos b_{\alpha\beta}}{b_{\alpha\beta}} + 3\Big(\frac{\sin b_{\alpha\beta}}{b_{\alpha\beta}^2} + \frac{\cos b_{\alpha\beta}}{b_{\alpha\beta}^3}\Big)\right], \\
D_{\alpha\beta} &= -\frac{3\gamma}{4}\left[(1-\cos^2\theta)\frac{\cos b_{\alpha\beta}}{b_{\alpha\beta}} - (1-3\cos^2\theta)\Big(\frac{\sin b_{\alpha\beta}}{b_{\alpha\beta}^2} + \frac{\cos b_{\alpha\beta}}{b_{\alpha\beta}^3}\Big)\right],
\end{aligned} \tag{2.76}$$

where we have used that $\mathbf{r}_{\alpha\beta}$ is represented in spherical polar coordinates as

$$\mathbf{r}_{\alpha\beta} = \begin{pmatrix} |\mathbf{r}_{\alpha\beta}| \sin\theta\cos\phi \\ |\mathbf{r}_{\alpha\beta}| \sin\theta\sin\phi \\ |\mathbf{r}_{\alpha\beta}| \cos\theta \end{pmatrix}. \tag{2.77}$$

Similarly, the dissipator coefficients are expressed as

$$\bar{X}_{\alpha\beta} = \begin{pmatrix} E_{\alpha\beta} & -G_{\alpha\beta}^{*} & F_{\alpha\beta} \\ -G_{\alpha\beta} & H_{\alpha\beta} & G_{\alpha\beta}^{*} \\ F_{\alpha\beta}^{*} & G_{\alpha\beta} & E_{\alpha\beta} \end{pmatrix}, \tag{2.78}$$

with

$$
\begin{aligned}
E_{\alpha\beta} &= \frac{3\gamma}{4}\left[(2-\sin^2\theta)\frac{\sin b_{\alpha\beta}}{b_{\alpha\beta}} + (2-3\sin^2\theta)\Big(\frac{\cos b_{\alpha\beta}}{b_{\alpha\beta}^2} - \frac{\sin b_{\alpha\beta}}{b_{\alpha\beta}^3}\Big)\right], \\
F_{\alpha\beta} &= \frac{3\gamma}{4}\sin^2\theta \mathrm{e}^{-2\mathrm{i}\phi}\left[\frac{\sin b_{\alpha\beta}}{b_{\alpha\beta}} + 3\Big(\frac{\cos b_{\alpha\beta}}{b_{\alpha\beta}^2} - \frac{\sin b_{\alpha\beta}}{b_{\alpha\beta}^3}\Big)\right], \\
G_{\alpha\beta} &= \frac{3\gamma}{4\sqrt{2}}\sin 2\theta \mathrm{e}^{\mathrm{i}\phi}\left[-\frac{\sin b_{\alpha\beta}}{b_{\alpha\beta}} - 3\Big(\frac{\cos b_{\alpha\beta}}{b_{\alpha\beta}^2} - \frac{\sin b_{\alpha\beta}}{b_{\alpha\beta}^3}\Big)\right], \\
H_{\alpha\beta} &= \frac{3\gamma}{2}\left[(1-\cos^2\theta)\frac{\sin b_{\alpha\beta}}{b_{\alpha\beta}} + (1-3\cos^2\theta)\Big(\frac{\cos b_{\alpha\beta}}{b_{\alpha\beta}^2} - \frac{\sin b_{\alpha\beta}}{b_{\alpha\beta}^3}\Big)\right].
\end{aligned}
\tag{2.79}
$$

2.6.3 Applied external magnetic field

From these results, we observe that there could potentially be a substantial amount of mixing between the three different states, for $m_J = -1, 0, +1$. We can reduce the occurrence of these processes by establishing a method to shift the excited levels such that some transitions are brought out of resonance. One way that we can achieve this is to apply an external magnetic field $\mathbf{B} = B_x\hat{x} + B_y\hat{y} + B_z\hat{z}$, where $\hat{x}$, $\hat{y}$ and $\hat{z}$ are unit vectors in the x-, y- and z-directions. Here we have defined these directions with respect to a quantisation axis pointing in the z-direction. The levels become detuned due to the Zeeman effect, therefore it is possible to distinguish between the three levels [96]. By introducing this magnetic field we highlight another reason why the four-level atom description is beneficial. In Fig. 2.2, we discussed how changing the dipole moment with respect to the atom separation changes the form of the interaction and dissipation matrix elements. This model allows us to consider the direction of the dipole moments in a physical sense. The magnetic field used to lift the level degeneracy also allows us to define the direction of the quantisation axis; dipole moments align to the magnetic field [82].

Now let us consider how the master equation is adapted when we introduce the interaction Hamiltonian

$$
H_{\mathbf{B}} = \frac{\mu_{\mathrm{B}} g}{\hbar}\sum_{\alpha=1}^{N}\mathbf{J}_\alpha\cdot\mathbf{B}, \tag{2.80}
$$

which models the coupling between an external magnetic field and an ensemble of four-level atoms [96]. Here, $\mu_{\mathrm{B}} = e\hbar/2m_e$ is the Bohr magneton (with electron charge e and mass m_e), g is the Landé g-factor and $\mathbf{J}_\alpha$ is the spin-1 operator for the

α-th atom:

$$\mathbf{J}_\alpha = \begin{pmatrix} J_x \\ J_y \\ J_z \end{pmatrix}_\alpha = \frac{\hbar}{\sqrt{2}} \begin{pmatrix} 0 & 1 & 0 \\ 1 & 0 & 1 \\ 0 & 1 & 0 \end{pmatrix}_\alpha \hat{x} + \frac{\hbar}{\sqrt{2}\mathrm{i}} \begin{pmatrix} 0 & 1 & 0 \\ -1 & 0 & 1 \\ 0 & -1 & 0 \end{pmatrix}_\alpha \hat{y} + \hbar \begin{pmatrix} 1 & 0 & 0 \\ 0 & 0 & 0 \\ 0 & 0 & -1 \end{pmatrix}_\alpha \hat{z}. \tag{2.81}$$

This contribution to the Hamiltonian can therefore be expressed as

$$H_{\mathbf{B}} = \mu_{\mathrm{B}} g \sum_{\alpha=1}^{N} \begin{pmatrix} B_z & (B_x - \mathrm{i}B_y)/\sqrt{2} & 0 \\ (B_x + \mathrm{i}B_y)/\sqrt{2} & 0 & (B_x - \mathrm{i}B_y)/\sqrt{2} \\ 0 & (B_x + \mathrm{i}B_y)/\sqrt{2} & -B_z \end{pmatrix}_\alpha . \tag{2.82}$$

A constraint, placed on the magnetic field amplitude $\mu_{\mathrm{B}} g \sqrt{B_x^2 + B_y^2 + Bz^2} = \Delta$, maintains the eigenvalues of the magnetic field Hamiltonian at constant values $E_{\mathrm{B}} = \pm\Delta, 0$; our eigenvalues of the magnetic field Hamiltonian always correspond to the same energy, regardless of the magnetic field angle. We can therefore express the magnetic field in polar coordinates such that

$$\mathbf{B} = \begin{pmatrix} B_x \\ B_y \\ B_z \end{pmatrix} = \frac{\Delta}{\mu_{\mathrm{B}} g} \begin{pmatrix} \sin\theta_{\mathrm{B}} \cos\phi_{\mathrm{B}} \\ \sin\theta_{\mathrm{B}} \sin\phi_{\mathrm{B}} \\ \cos\theta_{\mathrm{B}} \end{pmatrix}, \tag{2.83}$$

where the definitions of θ_{B} and ϕ_{B} are equivalent to the angles depicted in Fig. 2.1. This constraint will be important in the analysis that follows. The Hamiltonian that describes all aspects of the problem (atomic states, reservoir field, magnetic field and interactions) is

$$H = H_{\mathrm{a}} + H_{\mathbf{B}} + H_{\mathrm{f}} + V_I. \tag{2.84}$$

The contribution to the master equation due to the external magnetic field is $-\frac{\mathrm{i}}{\hbar}[H_{\mathbf{B}}, \rho]$. The master equation is therefore modified such that

$$\dot{\rho} = -\frac{\mathrm{i}}{\hbar}\left[H'_{\mathbf{B}}, \rho\right] + \mathcal{D}(\rho), \tag{2.85}$$

with the coherent interaction determined by

$$H'_{\mathbf{B}} = H_{\mathrm{dd}} + H_{\mathbf{B}} = \hbar \sum_{\alpha \neq \beta} \mathbf{b}'_\alpha \cdot \bar{W}_{\alpha\beta} \mathbf{b}_\beta + \frac{\mu_B g}{\hbar} \sum_{\alpha=1}^{N} \mathbf{J}_\alpha \cdot \mathbf{B}. \tag{2.86}$$

Finally, we want to write out the magnetic field Hamiltonian in the same form as the

coherent interaction matrix $\bar{W}_{\alpha\beta}$, in order to group the terms. We define the matrix

$$\bar{\Delta}_{\alpha\beta} = \delta_{\alpha\beta}\frac{\mu_{\mathrm{B}}g}{\hbar}\begin{pmatrix} B_z & (B_x - \mathrm{i}B_y)/\sqrt{2} & 0 \\ (B_x + \mathrm{i}B_y)/\sqrt{2} & 0 & (B_x - \mathrm{i}B_y)/\sqrt{2} \\ 0 & (B_x + \mathrm{i}B_y)/\sqrt{2} & -B_z \end{pmatrix}, \quad (2.87)$$

such that

$$H'_{\mathbf{B}} = H_{\mathrm{dd}} + H_{\mathbf{B}} = \hbar \sum_{\alpha,\beta=1} \mathbf{b}'_\alpha \cdot \bar{Y}_{\alpha\beta}\mathbf{b}_\beta, \quad (2.88)$$

where $\bar{Y}_{\alpha\beta} = \bar{W}_{\alpha\beta}|_{\alpha\neq\beta} + \bar{\Delta}_{\alpha\beta}$.

2.6.4 Laser driving

Now let us consider how the Hamiltonian, and hence the master equation, changes when we introduce laser driving to an ensemble of four-level atoms. For a single atom, we no longer have only one transition that can be excited but three. We assume that the laser driving is applied in conjunction with an external magnetic field, such that the three transitions have different detunings matching the magnetic field Hamiltonian eigenvalues $E_{\mathrm{B}} = -\Delta, 0, +\Delta$. Here, the direction of the external magnetic field defines the direction of the quantisation axis. Depending on the direction of the magnetic field (hence the quantisation axis), the eigenstates that correspond to these energies vary. For example, if we want to excite a state with $E_{\mathrm{B}} = 0$, the corresponding eigenstate is

$$\mathbf{U}_{E_{\mathrm{B}}=0}(\theta_{\mathrm{B}}, \phi_{\mathrm{B}}) = \begin{pmatrix} U^+_{E_{\mathrm{B}}=0} \\ U^0_{E_{\mathrm{B}}=0} \\ U^-_{E_{\mathrm{B}}=0} \end{pmatrix} = \frac{1}{\sqrt{2}}\begin{pmatrix} \sin\theta_{\mathrm{B}}(1 - 2\cos\phi_{\mathrm{B}}\mathrm{e}^{-\mathrm{i}\phi_{\mathrm{B}}}) \\ \sqrt{2}\cos\theta_{\mathrm{B}}\mathrm{e}^{-\mathrm{i}\phi_{\mathrm{B}}} \\ \sin\theta_{\mathrm{B}} \end{pmatrix}, \quad (2.89)$$

which is clearly dependent on θ_{B} and ϕ_{B}. When the external magnetic field is aligned in the $\hat{z}$-direction ($\theta_{\mathrm{B}} = 0,\ \phi_{\mathrm{B}} = 0$), this eigenstate is

$$\mathbf{U}_{E_{\mathrm{B}}=0}(0, 0) = \begin{pmatrix} 0 \\ 1 \\ 0 \end{pmatrix}, \quad (2.90)$$

so we need only excite the $|0\rangle$ state. On the other hand, if we were to apply this in the $\hat{x}$-direction, with $\theta_{\mathrm{B}} = \pi/2$ and $\phi_{\mathrm{B}} = 0$, we would find

$$\mathbf{U}_{E_{\mathrm{B}}=0}(\pi/2, 0) = \frac{1}{\sqrt{2}}\begin{pmatrix} -1 \\ 0 \\ 1 \end{pmatrix}, \quad (2.91)$$

which is a superposition of $|+\rangle$ and $|-\rangle$. Therefore, in order to include a laser driving term in the Hamiltonian that drives one of the three eigenstates (with its corresponding energy), we take the dot product of our chosen state with the atomic operator vectors to determine the correct superposition of our $|\pm,0\rangle$ states for a given orientation of the external magnetic field. When we extend to the many-body case, this object will not pick up an atom index since we assume that the external magnetic field is uniform for all atoms. The laser driving Hamiltonian for the many-body four-level atom ensemble is therefore given by

$$H'_{\mathrm{L}} = \sum_{\alpha=1}^{N} -\frac{\hbar\Omega_{\mathrm{L}}}{2}\left[\mathbf{U}_{E_{\mathrm{B}}}(\theta_{\mathrm{B}},\phi_{\mathrm{B}})\cdot\mathbf{b}'_{\alpha}(\mathbf{r}_{\alpha}) + \mathbf{U}'_{E_{\mathrm{B}}}(\theta_{\mathrm{B}},\phi_{\mathrm{B}})\cdot\mathbf{b}_{\alpha}(\mathbf{r}_{\alpha})\right], \tag{2.92}$$

where $\mathbf{U}'_{E_{\mathrm{B}}}(\theta_{\mathrm{B}},\phi_{\mathrm{B}}) = [\mathbf{U}^{\dagger}_{E_{\mathrm{B}}}(\theta_{\mathrm{B}},\phi_{\mathrm{B}})]^{\mathrm{T}}$. Here, we must choose which state to excite and how the magnetic field is aligned. This appears in the master equation as

$$\dot{\rho} = -\frac{\mathrm{i}}{\hbar}\left[H'_{\mathrm{L}} + H'_{\mathbf{B}}, \rho\right] + \mathcal{D}(\rho). \tag{2.93}$$

2.7 Summary

In this chapter, we have described the general protocol required to derive a master equation for a many-body system interacting with a reservoir electromagnetic field. Exploring the simplest system of two-level atoms has allowed us to outline the mathematical techniques and approximations utilised in this process; the justifications made for describing a many-body atomic system, in this way, are better understood. We proceeded to highlight the collective behaviour that arises in the master equation as an introduction to the work that is described in the remainder of this thesis. In addition to this, we discussed the requirement of including laser driving to allow for the excitation of two-level atomic systems which ultimately produces this interesting collective dynamics.

We then extended the two-level atom description to four-level atoms, and introduced an external magnetic field interaction term. This model allows us to describe a specific set of atomic systems, with a transition between a $J = 0$ state and a degenerate $J = 1$ sate. It also enables us to explore the dependence of collective behaviour on the direction of the atomic dipole moment with respect to the atom separation in a physically realisable setting. The application of a laser was also considered for this model, along with the external magnetic field.

We have now introduced the relevant mathematical tools that are necessary for this work, and we continue by further investigation into the features of collective behaviour for various geometries of atoms in the two-level and four-level description.

Chapter 3
Subradiance protected excitation transport

3.1 Introduction

Let us now consider scenarios where it may be useful to harness the collectivity that arises in open many-body atomic systems. For example, the achievement of optical quantum state storage and read-out on demand is an important challenge in the field of quantum information processing [97]. Here, the idea is to transfer the quantum state of an optical signal into the so-called quantum memory such that the information can be stored for a long time before reading it out, transforming it again into optical radiation [98]. Much theoretical and experimental research has been devoted to this field in the recent years, with proposals for the creation of quantum memories based on solid-state platforms [99–103], waveguides [104–107], and atomic ensembles [108–113].

One of the limitations for an atom-based quantum memory is that the storage time of the state is ultimately limited by the decay rate of the atomic states involved. In order to avoid this problem, the use of subradiance seems like the natural choice to make. Hence, subradiance in dense atomic gases is nowadays studied not only theoretically, but also experimentally in an ever-growing number of groups worldwide [20, 21, 23, 25, 28].

A number of proposals have been put forward where the excitation of these so-called subradiant many-body states for the storage of quantum information is sought after, such that the storage time of the light in the atomic gas can be increased [114, 115]. However, it has been recently shown that an even more significant improvement on the lifetime can be achieved when the atoms are trapped in periodic arrangements such as optical lattices or arrays of tweezers [14, 36, 55, 58, 116].

In this chapter we explore excitation dynamics within a one-dimensional chain of atoms where the atomic transition dipoles are coupled to the free radiation field. When the atoms are separated by distances smaller or comparable to the wavelength of the transition, the exchange of virtual photons leads to the transport of the excitation through the lattice. Even though this is a strongly dissipative system, we find that the transport is subradiant, that is, the excitation lifetime is orders of magnitude longer

than the one of an individual atom, hence we describe this realisation as subradiance-protected transport. In particular, we show that a subspace of the decay modes is formed by subradiant states whose corresponding energy spectrum has a linear dispersion relation, which allows for the dispersionless transport of wave packets over long distances with virtually zero decay rate.

Moreover, control over the group velocity and direction of the transport can be attained by effectively changing the orientation of the transition dipoles via an external uniform magnetic field while preserving its subradiant character. In particular, we show that the group velocity of the wave packet can be brought close to zero while preserving its long lifetime. We analyse the effect of disorder, which arises from the width of the external wavefunction of the atoms in each lattice trap and is inevitable in a realistic experimental scenario. Even though this can lead to the suppression of the transport of the wave packet due to localisation [117, 118], we find that the subradiant nature of the dynamics is robust against the presence of disorder [119, 120].

The chapter is organised as follows: we begin by restricting the Hilbert space to the single excitation sector (in Sec. 3.2), in order to derive exact equations for the system dynamics. The importance of carefully selecting the initial state is explored in Sec. 3.3, providing examples of how to further reduce the complexity of the problem. A ring lattice is then introduced in Sec. 3.4, as an approximate form for the linear chain, which allows us to analytically describe the decay spectrum and energy modes of such a system. With this set-up, we are capable of utilising the eigenvalues of the effective Hamiltonian, responsible for the system evolution, to model the dynamics of a ring lattice with a single excitation, as demonstrated in Sec. 3.5. In addition to this, we conduct an investigation in Sec. 3.5.1 into the likelihood of achieving subradiance protected excitation transport using currently available interatomic spacings. The analogous case of the linear chain is then explored in Sec. 3.6, and we probe the potential for light storage by adjusting the external magnetic field parameters in Sec. 3.7. We proceed to investigate the various scenarios introduced throughout this chapter in the presence of disorder to determine the system robustness in each case (Sec. 3.8). Finally, we assess some experimental challenges in Sec. 3.9, particularly the requirement of close proximity between atoms to achieve high fidelity transport. We explore a possible improvement by placing the atomic ensemble close to a layered metallic surface, which changes the properties of the radiation field.

3.2 Single excitation sector dynamics

We consider an ensemble of N atoms at positions $\mathbf{r}_\alpha$ with $\alpha = 1, \ldots, N$, each one tightly trapped in the sites of a one-dimensional lattice with lattice constant a [see

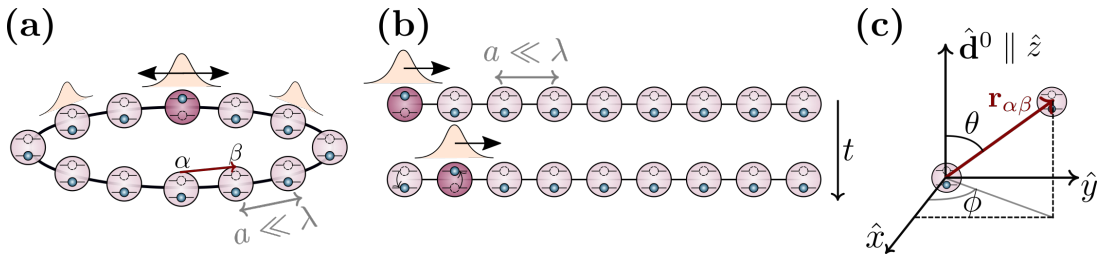

Figure 3.1: **The system.** We consider a one-dimensional chain of atoms with nearest neighbour separation a in **(a)** a ring and **(b)** a linear chain with open boundary conditions. The wave packet that contains the excitation is transported via dipole-dipole interactions induced by the collective coupling to the radiation field at zero temperature. **(c)** The polar angle θ of $\mathbf{r}_{\alpha\beta}$ (separation between the α-th and β-th atoms) controls the strength of the interactions and the collective character of the dissipation.

Fig. 3.1**(a)** and **(b)**]. We treat the system as an ensemble of four-level atoms using the description outlined in Sec. 2.6, and we choose the transition dipole moment $\mathbf{d}^0$ of the $|g\rangle \to |0\rangle$ transition to be aligned with the quantisation axis ($\hat{z}$-axis) [see Fig. 3.1**(c)**].

Let us for now assume that we configure a general, excited state that we want to evolve in time. Throughout, we assume that the initial state contains a single excitation, and the dynamics can be described in a truncated space formed by the many-body ground state $|G\rangle \equiv \bigotimes_{n=1}^{N} |g\rangle$ and the single excitation states $|i\rangle_\alpha \equiv \left(\bigotimes_{n=1}^{\alpha-1} |g\rangle\right) \otimes |i\rangle \otimes \left(\bigotimes_{n=\alpha+1}^{N} |g\rangle\right)$, for all $\alpha = 1 \dots N$ and $i = \pm, 0$. We do not specify here whether the excitation is localised on a single lattice site or whether it is delocalised across many, so we can write the state of the system in the most general form as

$$|\Psi(t)\rangle = c_G(t)|G\rangle + \sum_{i=\pm,0} \sum_{\alpha=1}^{N} c_\alpha^i(t)|i\rangle_\alpha, \tag{3.1}$$

with the coefficients $c_\alpha^i(t)$ describing the probability amplitude of the α-th atom being excited to the $|i\rangle$ state, and $c_G(t)$ is the probability amplitude associated with the ground state being occupied. The norm of this state is

$$\langle\Psi(t)|\Psi(t)\rangle = |c_G(t)|^2 + \sum_{i=\pm,0} \sum_{\alpha=1}^{N} |c_\alpha^i(t)|^2 = 1, \tag{3.2}$$

where $|c_\alpha^i(t)|^2$ represents the population of the i-th state of the α-th atom, and $|c_G(t)|^2$ is the population of the ground state. Here, we have used the fact that our states form an orthonormal basis, such that $\langle G|n\rangle_\beta = 0$, and ${}_\alpha\langle p|n\rangle_\beta = \delta_{\alpha\beta}^{pn}$. In the single excitation sector we fully describe the system with this collection of states, therefore the state is pure and we have $\rho = |\Psi(t)\rangle\langle\Psi(t)|$.

The excitation is transported via the exchange interactions given by H_{dd} [Eq. (2.55)]

which conserve the number of excitations, while the action of dissipation [Eq. (2.56)] can only decrease the number of excitations to zero. Here, the density matrix takes the form

$$\bar{\rho} = \begin{pmatrix} \rho_{GG} & \boldsymbol{\rho}_{Ge} \\ \boldsymbol{\rho}_{eG} & \bar{\rho}_{ee} \end{pmatrix}, \tag{3.3}$$

where $\rho_{GG} = \langle G|\rho|G\rangle$, $\boldsymbol{\rho}_{Ge} = \langle G|\rho|\mathbf{e}\rangle$, $\boldsymbol{\rho}_{eG} = \langle \mathbf{e}|\rho|G\rangle$, and $\bar{\rho}_{ee} = \langle \mathbf{e}|\rho|\mathbf{e}\rangle$, with $|\mathbf{e}\rangle$ being a row vector containing all single excitation states. The truncation dramatically reduces the Hilbert space from a 4^N-dimensional system to one with $3N+1$ dimensions. The density matrix, in this case, is $(3N+1)\times(3N+1)$ in size.

We now want to find expressions for the equations of motion of each component of the truncated density matrix $\bar{\rho}$. We obtain these equations by first noting that the time derivative of the density matrix contains elements that are individually differentiated with respect to time

$$\dot{\bar{\rho}} = \begin{pmatrix} \dot{\rho}_{GG} & \dot{\boldsymbol{\rho}}_{Ge} \\ \dot{\boldsymbol{\rho}}_{eG} & \dot{\bar{\rho}}_{ee} \end{pmatrix}. \tag{3.4}$$

Then we simply substitute the master equation (Eq. (2.85)) into the four components $\dot{\rho}_{GG} = \langle G|\dot{\rho}|G\rangle$, $\dot{\rho}_{Ge^p_\alpha} = \langle G|\dot{\rho}|p\rangle_\alpha$, $\dot{\rho}_{e^p_\alpha G} = {}_\alpha\langle p|\dot{\rho}|G\rangle$ and $\dot{\rho}_{e^p_\alpha e^n_\beta} = {}_\alpha\langle p|\dot{\rho}|n\rangle_\beta$. Taking as an example the matrix of elements containing coherences between excited states, $\dot{\rho}_{e^p_\alpha e^n_\beta} = {}_\alpha\langle p|\dot{\rho}|n\rangle_\beta$, we can demonstrate how the time evolution of each component is calculated.

Firstly, we write the system operators within the master equation in terms of the ground state and single excitation states

$$\dot{\rho} = \sum_{i,\ell=\pm,0}\sum_{\epsilon,\gamma=1}^{N}\left[-\mathrm{i}Y^{\ell i}_{\gamma\epsilon}\left[|\ell\rangle_{\gamma\epsilon}\langle i|,\rho\right] + X^{\ell i}_{\gamma\epsilon}\left(|G\rangle_\epsilon\langle i|\rho|\ell\rangle_\gamma\langle G| - \frac{1}{2}\left\{|\ell\rangle_{\gamma\epsilon}\langle i|,\rho\right\}\right)\right], \tag{3.5}$$

and then we act with the appropriate states on either side

$$\begin{aligned} {}_\alpha\langle p|\dot{\rho}|n\rangle_\beta = \sum_{i,\ell=\pm,0}\sum_{\epsilon,\gamma=1}^{N}\Bigg[& -\mathrm{i}Y^{\ell i}_{\gamma\epsilon}\left({}_\alpha\langle p|\ell\rangle_{\gamma\epsilon}\langle i|\rho|n\rangle_\beta - {}_\alpha\langle p|\rho|\ell\rangle_{\gamma\epsilon}\langle i|n\rangle_\beta\right) \\ & + X^{\ell i}_{\gamma\epsilon}\Bigg({}_\alpha\langle p|G\rangle_\epsilon\langle i|\rho|\ell\rangle_\gamma\langle G|n\rangle_\beta - \frac{1}{2}{}_\alpha\langle p|\ell\rangle_{\gamma\epsilon}\langle i|\rho|n\rangle_\beta \\ & -\frac{1}{2}{}_\alpha\langle p|\rho|\ell\rangle_{\gamma\epsilon}\langle i|n\rangle_\beta\Bigg)\Bigg]. \end{aligned} \tag{3.6}$$

By computing the matrix elements, we find

$$\begin{aligned}\dot{\rho}_{e_\alpha^p e_\beta^n} &= \sum_{i,\ell=\pm,0}\sum_{\epsilon,\gamma=1}^{N} -\mathrm{i}Y_{\gamma\epsilon}^{\ell i}\left(\delta_{\alpha\gamma}^{p\ell}\rho_{e_\epsilon^i e_\beta^n} - \rho_{e_\alpha^p e_\gamma^\ell}\delta_{\epsilon\beta}^{in}\right) - \frac{X_{\gamma\epsilon}^{\ell i}}{2}\left(\delta_{\alpha\gamma}^{p\ell}\rho_{e_\epsilon^i e_\beta^n} + \rho_{e_\alpha^p e_\gamma^\ell}\delta_{\epsilon\beta}^{in}\right) \\ &= -\mathrm{i}\sum_{i=\pm,0}\sum_{\epsilon=1}^{N}\left(Y_{\alpha\epsilon}^{pi} - \frac{\mathrm{i}X_{\alpha\epsilon}^{pi}}{2}\right)\rho_{e_\epsilon^i e_\beta^n} + \mathrm{i}\sum_{\ell=\pm1,0}\sum_{\gamma=1}^{N}\rho_{e_\alpha^p e_\gamma^\ell}\left(Y_{\gamma\beta}^{\ell n} + \frac{\mathrm{i}X_{\gamma\beta}^{\ell n}}{2}\right).\end{aligned} \tag{3.7}$$

We proceed to divide the coherent interaction term back into components of $W_{\alpha\beta}^{pi}$ and $\Delta_{\alpha\beta}^{pi}$

$$\dot{\rho}_{e_\alpha^p e_\beta^n} = \sum_{i=\pm,0} -\mathrm{i}\left[\left(\Delta_{\alpha\alpha}^{pi}\rho_{e_\alpha^i e_\beta^n} - \rho_{e_\alpha^p e_\beta^i}\Delta_{\beta\beta}^{in}\right) + \sum_{\epsilon=1}^{N}\left(Z_{\alpha\epsilon}^{pi}\rho_{e_\epsilon^i e_\beta^n} - \rho_{e_\alpha^p e_\epsilon^i}Z_{\epsilon\beta}^{in*}\right)\right], \tag{3.8}$$

which in matrix form is

$$\dot{\bar{\rho}}_{ee} = -\frac{\mathrm{i}}{\hbar}\left[\bar{H}_{\mathrm{eff}}, \bar{\rho}_{ee}\right], \tag{3.9}$$

obeying the von Neumann equation. Here, we have defined an effective Hamiltonian $\bar{H}_{\mathrm{eff}} = \hbar(\bar{Z} + \bar{\Delta})$ that evolves the excited sector of the density matrix $\bar{\rho}_{ee}$ (a $3N \times 3N$ matrix), and one easily identifies that $\bar{\rho}_{ee}$ is decoupled from the remaining parts. Recall that $\bar{Z}$ and $\bar{\Delta}$ are $3N \times 3N$ matrices whose components for $\alpha, \beta = 1, \ldots, N$ and $p, n = \pm, 0$ are determined by $Z_{\alpha\beta}^{pn} = W_{\alpha\beta}^{pn}|_{\alpha\neq\beta} - \frac{\mathrm{i}X_{\alpha\beta}^{pn}}{2}$ - the coherent Hamiltonian $\bar{W}$ [Eq. (2.75)] and the dissipative coefficients $\bar{X}$ [Eq. (2.78)] - and $\Delta_{\alpha\beta}^{pi}$ [Eq. (2.87)]. The equations for the remaining terms can be calculated using the same method and are

$$\begin{aligned}\dot{\rho}_{GG} &= \sum_{\ell,i=\pm,0}\sum_{\epsilon,\gamma=1}^{N} X_{\gamma\epsilon}^{\ell i}\rho_{e_\gamma^\ell e_\epsilon^i} \;\Rightarrow\; \dot{\rho}_{GG} = \bar{X}\cdot\bar{\rho}_{ee}, \\ \dot{\rho}_{Ge_\alpha^p} &= \mathrm{i}\sum_{i=\pm,0}\sum_{\epsilon=1}^{N}\rho_{Ge_\epsilon^i}Z_{\epsilon\alpha}^{ip*} \;\Rightarrow\; \dot{\boldsymbol{\rho}}_{Ge} = \mathrm{i}\boldsymbol{\rho}_{Ge}\left(\bar{Z}^\dagger + \bar{\Delta}\right), \\ \dot{\rho}_{e_\alpha^p G} &= -\mathrm{i}\sum_{i=\pm,0}\sum_{\epsilon=1}^{N} Z_{\alpha\epsilon}^{pi}\rho_{e_\epsilon^i G} \;\Rightarrow\; \dot{\boldsymbol{\rho}}_{eG} = -\mathrm{i}\left(\bar{Z} + \bar{\Delta}\right)\boldsymbol{\rho}_{eG}.\end{aligned} \tag{3.10}$$

Due to the decoupling of the excited state terms from the ground state terms, and given that our initial state has exactly one excitation and belongs to this subspace, we can consider the evolution of a reduced density matrix alone

$$\bar{\rho}_{ee} = \sum_{\alpha,\beta=1}^{N}\sum_{i,\ell=\pm,0} c_\alpha^i(t)c_\beta^{\ell*}(t)|i\rangle_{\alpha\beta}\langle\ell|. \tag{3.11}$$

Note that the only two possible processes that the excitation can undergo are as follows: Firstly, the excitation can de-excite into the ground state, in which case we no

longer have any system evolution. Alternatively, the excitation transfers to another atom in the chain via coherent exchange interaction.

The time evolution here in the excited state alone is not trace-preserving, whereas the entire density matrix has $\mathrm{Tr}\{\rho\} = 1$. The value of ρ_{GG} increases over time due to the dissipative dynamics generated by the non-Hermitian effective Hamiltonian; the dissipation is constantly reducing the population of the excited states. Therefore, the survival probability $P_{\mathrm{sur(t)}}$, i.e., the probability for not emitting a photon into the radiation field, is given by the trace of $\bar{\rho}_{ee}$

$$P_{\mathrm{sur}}(t) = \sum_{\alpha=1}^{N} \sum_{i=\pm,0} |c_{\alpha}^{i}(t)|^2, \tag{3.12}$$

which decreases as a function of time.

Another useful quantity for us to measure is the instantaneous photon emission rate (also called activity) and is given by

$$\langle K(t) \rangle = \sum_{\alpha,\beta=1}^{N} \langle \mathbf{b}_{\alpha}^{'} \cdot \bar{X}_{\alpha\beta} \mathbf{b}_{\beta} \rangle. \tag{3.13}$$

In the case of an ensemble of two-level atoms ($\bar{X}_{\alpha\beta} \to \Gamma_{\alpha\beta}$ and $\bar{W}_{\alpha\beta} \to V_{\alpha\beta}$) the activity can also be expressed in terms of the dissipation eigenvalues Γ_{m}^{D} introduced in Eq. (2.57) :

$$\langle K(t) \rangle = \sum_{m=1}^{N} \Gamma_{D}^{m} \langle J_{m}^{\dagger} J_{m} \rangle, \tag{3.14}$$

where $J_{m}^{\dagger}$ and J_{m} are jump operators from Eq. (2.59). Each term inside the summation describes the rate of decay due to a particular mode. When we take the sum over all rates, we return the total rate of decay at a given time.

A value of the activity larger (smaller) than the single atom decay rate γ is indicative of collective superradiant (subradiant) behaviour of the photon emission. For example, for a single two-level atom excited to $|e\rangle$, the activity at $t = 0$ is simply $\langle K(0) \rangle = \gamma$: the single atom emission rate. Extending this system now to $N = 2$ two-level atoms, with an initial state that is either a symmetric $(+)$ or anti-symmetric $(-)$ superposition of each atom being excited $|\psi(0)\rangle = \frac{1}{\sqrt{2}} (|e\rangle_1 \pm |e\rangle_2)$, the initial activity is $\langle K(0) \rangle = \frac{1}{2} (\Gamma_{11} \pm \Gamma_{12} \pm \Gamma_{21} + \Gamma_{22})$. As we explored in Sec. 2.4.2, in the limit of non-interacting atoms the coefficients tend towards $\Gamma_{\alpha\alpha} = \gamma$ and $\Gamma_{\alpha\neq\beta} = 0$. The activity in this case is therefore $\langle K(0) \rangle = \gamma$ as one would expect; the atomic separation is large enough for the atoms to behave as independent emitters. Conversely, when $a \to 0$ all coefficients are $\Gamma_{\alpha\beta} \approx \gamma$. The symmetric initial state then has associated a large activity $\langle K(0) \rangle = 2\gamma$, while the anti-symmetric state yields $\langle K(0) \rangle = 0$, hence

demonstrating cooperative effects in the form of super- and subradiant emission rates.

As an additional interpretation, it is worth noting that while we have calculated the evolution of the density matrix in the form of a von Neumann equation given above, we may consider the time evolution of the state containing only the excitation sector (without the ground state)

$$|\psi(t)\rangle = \sum_{i=\pm,0} \sum_{\alpha=1}^{N} c_\alpha^i(t)|i\rangle_\alpha, \tag{3.15}$$

in the Schrödinger picture

$$|\dot{\psi}(t)\rangle = -\frac{\mathrm{i}}{\hbar} H_{\mathrm{eff}}|\psi(t)\rangle. \tag{3.16}$$

This equation of motion has the solution

$$|\psi(t)\rangle = \mathrm{e}^{-\mathrm{i}H_{\mathrm{eff}}t/\hbar}|\psi(0)\rangle, \tag{3.17}$$

where we take the matrix exponential of the effective Hamiltonian; this state also evolves under the non-hermitian effective Hamiltonian H_{eff}. Given Eq. (3.15), we also deduce that the probability amplitudes for each atom being excited evolve in the same way

$$\mathbf{c}(t) = \mathrm{e}^{-\mathrm{i}\bar{H}_{\mathrm{eff}}t/\hbar}\mathbf{c}(0), \tag{3.18}$$

where $\mathbf{c}(t)$ is a $(3N \times 1)$ vector containing elements $c_\alpha^i(t)$ and $\bar{H}_{\mathrm{eff}}$ is the effective Hamiltonian in matrix form.

3.3 Simplifying the four-level atom model

The assumption that our system exists in the single excitation sector has allowed us to vastly reduce the Hilbert space, hence the complexity, of the problem that we are exploring. In this way, we are able to model the dynamics of this many-particle atomic system. We now explore another simplification to the description of our system; we constrain the positions of the atoms to exist only in the plane perpendicular to the direction of the dipole moments associated with the $|g\rangle \rightarrow |0\rangle$ transition (see Fig. 3.2).

Generally, for a pair of atoms α and β, a 3×3 subsection of the matrix $\bar{W}$ contains all possible forms of interaction between the two atoms. The diagonal elements are the interaction strengths between two of the same type of excited state ($++$, 00 and $--$), while the off-diagonal elements are the interactions between mixed pairs of states, $+0$ for instance. We now consider the case where the atoms are constrained to the $\hat{x}$-$\hat{y}$ plane, the atomic dipole moment for the $|g\rangle \rightarrow |0\rangle$ transition is aligned in the

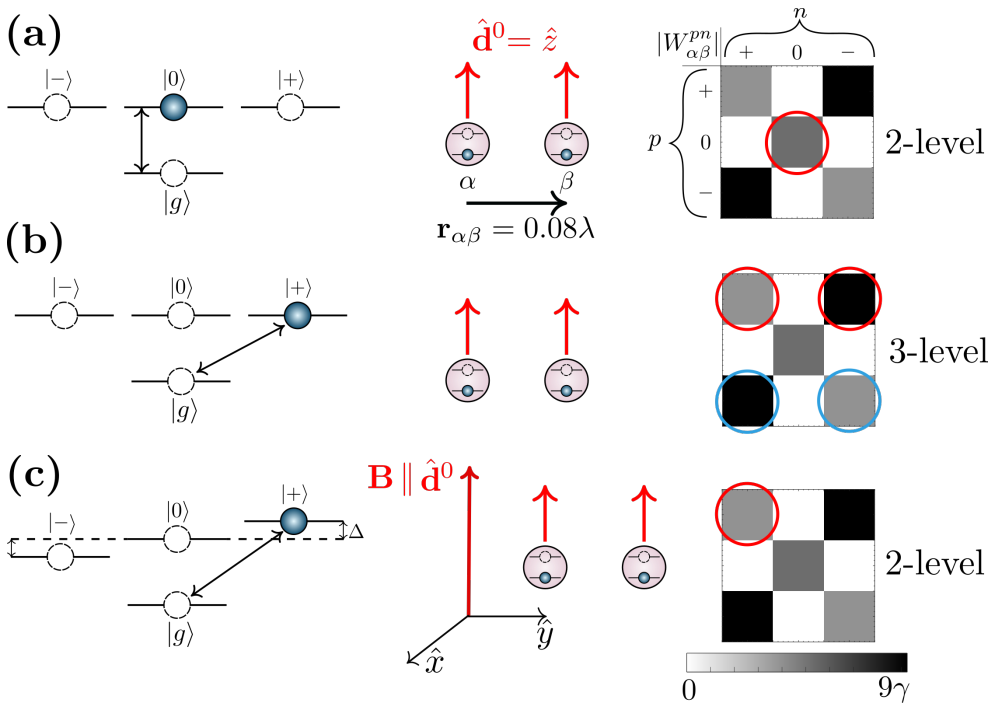

Figure 3.2: **Coupling between states.** An excited four-level atom (α), with dipole moment for the $|g\rangle \rightarrow |0\rangle$ transition $\mathbf{d}^0$, interacts with a neighbouring atom (β) such that the separation vector $\mathbf{r}_{\alpha\beta}$ lies on the plane perpendicular to the dipole moment. On the right-hand side the 3×3 grids represent the magnitudes of the coupling strengths between each pair of excited states for the two atoms. For demonstration, the strengths correspond to atoms separated by $\mathbf{r}_{\alpha\beta} = 0.08\lambda$ and the white to black colour scheme demonstrates increasing coupling strength from $0 \rightarrow 9\gamma$. **(a)** Atom α is excited to $|0\rangle_\alpha$ and only transfers the excitation to $|0\rangle_\beta$, since $W^{\pm 0}_{\alpha\beta} = 0$. **(b)** Atom α is excited to $|+\rangle_\alpha$ and can transfer the excitation to both $|\pm\rangle_\beta$. This ultimately allows further coupling from $|+\rangle$ states and $|-\rangle$ states. **(c)** An external magnetic field is applied to the system, shifting the $|\pm\rangle$ levels by $\pm\Delta$, and atom α is excited to $|+\rangle_\alpha$. The elements of $W^{pn}_{\alpha\beta}$ are unchanged, however the shift decouples the states such that we only see $W^{++}_{\alpha\beta}$ coupling.

$\hat{z}$-direction $\mathbf{d}^0 || \hat{z}$ and the dipole moments for the $|g\rangle \rightarrow |\pm\rangle$ transitions extend in the $\hat{x}$-$\hat{y}$ plane. In this scenario, all elements of $\bar{W}$ that represent interactions between $|\pm\rangle$ and $|0\rangle$ are reduced to zero, $W^{\pm 0}_{\alpha\beta} = W^{0\pm}_{\alpha\beta} = 0$: the state $|0\rangle_\alpha$ is decoupled from $|\pm\rangle_\beta$. This informs us that an excited atom in $|0\rangle_\alpha$ can only transfer its excitation to other $|0\rangle_\beta$ [Fig. 3.2**(a)**]. We can therefore reduce the description of the four-level atoms to the two-level model, in this case, provided that the state is initialised only in $m_J = 0$. The coupling coefficient between $m_J = 0$ states $D_{\alpha\beta}$, defined in Eq. (2.76), is in agreement with the coupling between two-level atoms $V_{\alpha\beta}$ [Eq. (2.53)].

Now we take the initial excited state to be $|+\rangle_\alpha$, for example in Fig. 3.2**(b)**. The dipole moment associated with this transition is $\mathbf{d}^+ = (-\hat{x} - \mathrm{i}\hat{y})/\sqrt{2}$. While we maintain decoupling from $|0\rangle_\beta$, we now experience mixing between the $|\pm\rangle$ states and we

have the equivalent of a three level system (one ground state and two-fold degenerate excited states). In this case, we can only describe the system with two-level atoms by applying an external magnetic field [Fig. 3.2**(c)**]. The field shifts the energy levels such that $|+\rangle_\alpha$ becomes off-resonant with $|-\rangle_\beta$ (and also $|0\rangle_\beta$), hence the atoms only experience coupling of the form $W_{\alpha\beta}^{++}$. Once again, this situation is well represented by two-level systems where we must take care to define the dipole moment appropriately for modelling these states. We can apply an external magnetic field to detune the levels and decouple all three excited states for any system geometry, regardless of the transition dipole moment direction with respect to the atom separation. In this way, we remove the necessity for a specific geometry that sets $W_{\alpha\beta}^{pn} \to 0$, for $p \neq n$.

Utilising the external magnetic field to simplify the four-level description, combined with the assumption that we can model the system dynamics within the single excitation sector, allows us to explore other properties of our many-body systems such as the decay spectrum and dispersion relation.

3.4 Spectrum and decay rates

For illustration purposes, we take the first case depicted in Fig. 3.2**(a)**, where only the $|0\rangle$ state is excited initially. Both the coherent and incoherent couplings between $|0\rangle$ and $|\pm\rangle$ vanish ($W_{\alpha\beta}^{\pm 0} = 0$ and $X_{\alpha\beta}^{\pm 0} = 0$), hence the dynamics is determined solely by $W_{\alpha\beta}^{00}$ and $X_{\alpha\beta}^{00}$; the system is approximated by an ensemble of two-level atoms. The effective Hamiltonian is therefore reduced to

$$\bar{H}_{\text{eff}} = \hbar \bar{Z}, \tag{3.19}$$

where $\bar{Z} = \bar{V} - \mathrm{i}\frac{\bar{\Gamma}}{2}$ is the non-Hermitian Hamiltonian, containing interaction and dissipation elements defined in the two-level atom case by Eq. (2.53) and Eq. (2.52).

We briefly demonstrated how cooperativity arises in the decay modes of a many-body system of two-level atoms, in Sec. 2.4.2; we diagonalised $\bar{\Gamma}$ analytically for $N = 2$ atoms and numerically for an $N = 10$ atom chain. We can further our understanding of the appearance of super- and subradiance by exploring the shape of the decay spectrum for N-body systems in one dimension. We begin by exploring a ring lattice, where the ring plane is perpendicular to the dipole moment $\mathbf{d}^0$ (i.e. $\theta = \pi/2$), as illustrated in Fig. 3.1(a) [60–62]. We utilise this model due to its simplicity: the ring lattice has periodic boundary conditions and translational invariance in the separation between pairs of atoms, such that the interaction and dissipation matrices, $\bar{V}$ and $\bar{\Gamma}$, both have a circulant, symmetric form. These properties allow the eigenstates and eigenvalues to be determined analytically, and the ring geometry also provides a good approximation for a long finite chain of atoms when we are observing modes

away from the boundaries.

The eigensystems for the interaction and dissipation matrices are calculated, as follows: the form of these matrices for a ring of atoms is

$$\bar{M} = \begin{pmatrix} j_0 & j_1 & j_2 & \cdots & j_1 \\ j_1 & j_0 & j_1 & \cdots & j_2 \\ j_2 & j_1 & j_0 & \cdots & j_3 \\ \vdots & \vdots & \vdots & \ddots & \vdots \\ j_1 & j_2 & j_3 & \cdots & j_0 \end{pmatrix}, \tag{3.20}$$

where the element index is given by $\xi = |\alpha - \beta|$, and $j_{N-\xi} = j_\xi$. This is an example of a Toeplitz matrix since the elements are the same on each diagonal, and in this instance it is also circulant because each row of the matrix is simply the previous row shifted by one element to the right. For our system, we also find that this matrix is symmetric due to the invariance of $V_{\alpha\beta}$ and $\Gamma_{\alpha\beta}$ under the exchange of α and β.

Interestingly circulant matrices all share the same set of eigenvectors

$$U_k = \frac{1}{\sqrt{N}} \begin{pmatrix} 1 \\ \mathrm{e}^{\mathrm{i}\frac{2\pi}{N}(k-1)} \\ \mathrm{e}^{\mathrm{i}\frac{2\pi}{N}(k-1)2} \\ \vdots \\ \mathrm{e}^{\mathrm{i}\frac{2\pi}{N}(k-1)(N-1)} \end{pmatrix}, \tag{3.21}$$

with eigenvalues related to the matrix elements j_ξ [121, 122]:

$$\lambda_k = \sum_{\xi=1}^{N} j_{\xi-1} \mathrm{e}^{-\mathrm{i}\frac{2\pi}{N}(k-1)(\xi-1)}. \tag{3.22}$$

While the symmetry in our system simplifies the form of the eigenvalues, since $j_{\xi-1} = j_\xi$, it is not a necessary condition to find these solutions. The eigenvectors and eigenvalues given by Eq. (3.21) and Eq. (3.22) hold for any circulant matrix.

Furthermore, this result tells us that the same set of eigenstates diagonalises both $\bar{V}$ and $\bar{\Gamma}$ for a ring configuration. The diagonalised form of $\bar{\Gamma}$ returns a spectrum of decay modes for our dissipative system Γ_k, whereas the eigenvalues found by diagonalising $\bar{V}$ represent the energy of the different modes V_k [1]. The simultaneous eigenstates for

[1] Γ_k and Γ_D^m are both the eigenvalues of $\bar{\Gamma}$, however k is related to the momentum space whereas m represents ordering of the modes from most subradiant to most superraidant.

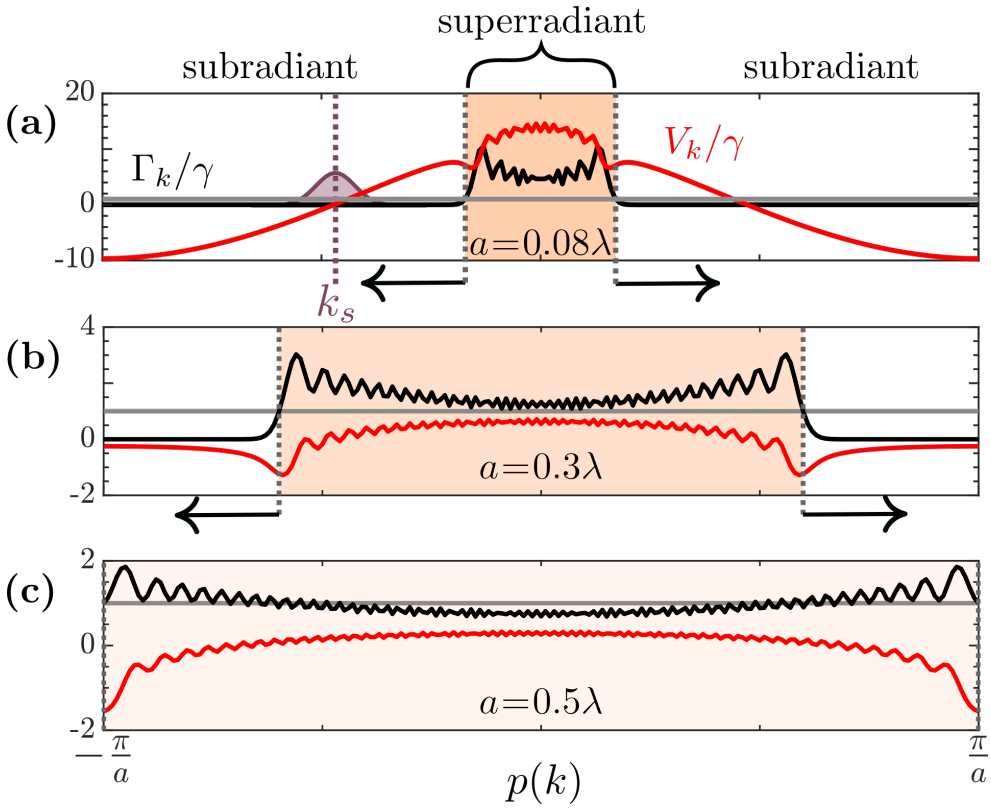

Figure 3.3: **Decay rates and the energy spectrum.** The decay rates Γ_k (black) and corresponding energies V_k (red), as a function of momentum $p(k) = 2\pi k/(Na)$, of the eigenstates associated with a ring lattice of $N = 201$ two-level atoms, scaled by the single atom decay rate γ (solid grey line). For each case, the interatomic spacing is **(a)** $a = 0.08\lambda$, **(b)** $a = 0.3\lambda$ and **(c)** $a = 0.5\lambda$. The orange shaded area indicates states which are superradiant, i.e. $\Gamma_k > \gamma$, and its intensity decreases as the subradiant manifold is diminished. The purple shaded region in **(a)** demonstrates an example excited state that takes the form of a Gaussian wave packet, centred at k_s (purple dotted vertical line).

both matrices can be expressed in terms of the plane waves

$$|\varphi_k\rangle = \frac{1}{\sqrt{N}} \sum_{\alpha=1}^{N} \mathrm{e}^{\mathrm{i}\frac{2\pi}{N}(\alpha-1)(k-q)} |e\rangle_\alpha, \tag{3.23}$$

with $k = -\lfloor N/2 \rfloor, \ldots \lfloor (N-1)/2 \rfloor$ and $q = \lfloor N/2 \rfloor$, where we have shifted the momentum $p(k) = 2\pi k/(Na)$ of these states by applying an overall phase factor.

Let us now observe the energy spectrum and decay modes of a chain of $N = 201$ atoms, for various atomic spacings (see Fig. 3.3). We see that for small interatomic spacing [Fig. 3.3**(a)**], the majority of the decay modes have a subradiant character with near-zero rates. These regions are here separated from the superradiant rates by the grey dotted vertical lines. By increasing the separation [Fig. 3.3**(b)**] we reduce the value of the superradiant rates whilst pushing the boundaries between the regions

outwards (reducing the subradiant manifold). When the spacing approaches $a = 0.5\lambda$ [Fig. 3.3**(c)**], the rates with values around $k = 0$ drop below the single atom decay rate, and the original superradiant boundary reaches the edges of the momentum space. Now the decay rates are comparable to the single atom decay rate across the momentum space.

We can also gain a physical intuition behind the energy modes from Fig. 3.3 by considering the gradient of V_k. By plotting the energy eigenvalues in momentum space, we are able to extract the group velocity of a wave packet in k-space. Consider the instance depicted in Fig. 3.3**(a)**: if we excite a Gaussian wave packet, centred at k_s within the subradiant manifold such that $\mathrm{sgn}(p(k_s)) = -1$, this would be the equivalent of preparing a state in real space with a momentum 'kick' in one direction. In contrast, taking the same state on the opposite side of the spectrum creates propagation in the other direction. It is worth noting that we can only consider the wave packet to travel with a group velocity for the conditions described in Fig. 3.3**(a)**; the gradient of V_k is linear and the excited eigenstates in this superposition travel with the same associated velocity. Otherwise, the system exhibits dispersive propagation of the excitation which quickly spreads across many lattice sites. We will explore this further by analysing the dynamics of such systems.

3.5 Subradiant transport on a ring lattice

An initial state prepared in the single excitation sector can be written as

$$|\psi(0)\rangle = \sum_{\alpha=1}^{N} c_\alpha(0)|e\rangle_\alpha = \frac{1}{\sqrt{N}}\sum_{k=1}^{N} c_k(0)|\varphi_k\rangle, \tag{3.24}$$

where the coefficients $c_\alpha(0)$ and $c_k(0)$ represent the probability amplitude distribution of the initial state in real and momentum space, respectively. The coefficients are related by

$$\begin{aligned}\frac{1}{\sqrt{N}}c_k(0) = \sum_{\alpha=1}^{N} c_\alpha(0)\langle\varphi_k|e\rangle_\alpha &= \frac{1}{\sqrt{N}}\sum_{\alpha,\beta=1}^{N} c_\alpha(0)\mathrm{e}^{-\mathrm{i}\frac{2\pi}{N}(\beta-1)(k-q)}{}_\beta\langle e|e\rangle_\alpha \\ &= \frac{1}{\sqrt{N}}\sum_{\alpha=1}^{N} c_\alpha(0)\mathrm{e}^{-\mathrm{i}\frac{2\pi}{N}(\alpha-1)(k-q)},\end{aligned} \tag{3.25}$$

where we have substituted in the eigenstate $|\varphi_k\rangle$ given by Eq. (3.23). Recalling that the time evolved state is related to the effective Hamiltonian by Eq. (3.17), we can

write

$$|\psi(t)\rangle = \frac{1}{\sqrt{N}} \sum_{k=1}^{N} c_k(0) \mathrm{e}^{-\mathrm{i}Zt} |\varphi_k\rangle = \frac{1}{\sqrt{N}} \sum_{k=1}^{N} c_k(0) \mathrm{e}^{-\mathrm{i}\left(V_k - \mathrm{i}\frac{\Gamma_k}{2}\right)t} |\varphi_k\rangle, \tag{3.26}$$

where V_k and Γ_k are the eigenvalues of the matrices $\bar{V}$ and $\bar{\Gamma}$, respectively. We can contain the time evolution within the coefficients such that $c_k(t) = c_k(0)\mathrm{e}^{-\mathrm{i}(V_k - \mathrm{i}\frac{\Gamma_k}{2})t}$, and the state is

$$|\psi(t)\rangle = \frac{1}{\sqrt{N}} \sum_{k=1}^{N} c_k(t) |\varphi_k\rangle. \tag{3.27}$$

Let us start by considering the initial state to be $|e\rangle_1$, i.e. an excitation localised on a single site of the lattice such that $c_\alpha(0) = \delta_{\alpha 1}$. This state [Eq. (3.23)] can be written as a symmetric superposition of all plane waves [see Fig. 3.4**(a)**], i.e.

$$|\psi(0)\rangle = \frac{1}{\sqrt{N}} \sum_{k=1}^{N} |\varphi_k\rangle, \tag{3.28}$$

and its time evolution is then given by

$$|\psi(t)\rangle = \frac{1}{\sqrt{N}} \sum_{k=1}^{N} \mathrm{e}^{-\mathrm{i}\left(V_k - \mathrm{i}\frac{\Gamma_k}{2}\right)t} |\varphi_k\rangle. \tag{3.29}$$

The dynamics in real space is depicted in Fig. 3.4**(c)**, where we observe that the initial wave packet splits into two that travel in opposite directions. The splitting of the excitation is caused by the symmetric energy spectra in Fig. 3.3. These states in real space disperse quickly due to the non-linearity of V_k as a function of momentum. More importantly, the superradiant components (with large Γ_k) decay very fast [Fig. 3.4**(b)**] and only the subradiant ones remain populated. In all cases considered, the lifetime of the excitation is dramatically longer than in the case of a single atom. This result is highlighted in Fig. 3.4**(d)**, which shows a plateau in the survival probability $P_{\mathrm{sur}}(t)$, and near-zero emission rate $\langle K(t)\rangle$ after a rapid initial decay. The height of the plateau of $P_{\mathrm{sur}}(t)$ is approximately given by the number of subradiant eigenstates divided by the total number of modes N, as demonstrated in Fig. 3.4**(f)**. This approximation is valid for large system sizes and only holds for values of $a/\lambda \leq 0.5$. For a fixed value of a/λ, the height of the plateau remains almost constant when increasing the number of atoms N. For a fixed size of the system N, on the other hand, reducing a/λ increases the relative number of subradiant eigenstates and hence the survival probability, as can be seen in Fig. 3.4**(e)**.

While this result is interesting in itself, we can also modify the propagation of the wave packet around the ring by investigating further the energy spectra. As can

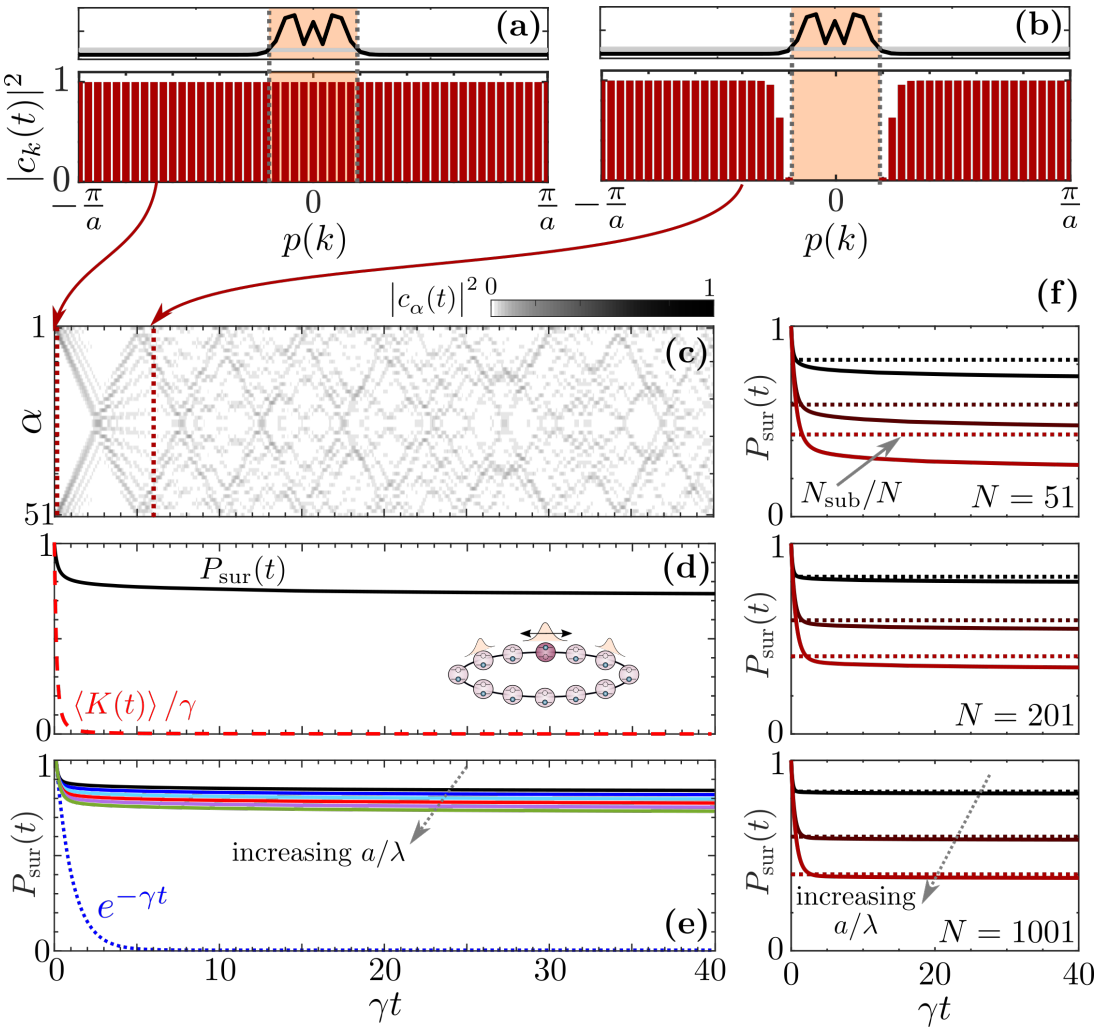

Figure 3.4: **Subradiance on a ring.** A lattice formed by $N = 51$ atoms and $a/\lambda = 0.08$. The ring is initialised with a single excitation on site $\alpha = 1$, such that the population of eigenstates in momentum space $|c_k(t)|^2$ is an equal superposition for all $p(k)$ at **(a)** $\gamma t = 0$. After some elapsed time **(b)** $\gamma t = 6$, the state has evolved and the superradiant states have quickly vanished. The decay rates are provided in the upper panels with the superradiant region shaded in orange. **(c)** The corresponding excitation probability $|c_\alpha(t)|^2$, in real space, at site α as a function of time given by Eq. (3.18). **(d)** Probability of survival of the initial excitation $P_{\rm sur}$ (black solid line) and activity $\langle K\rangle$ (red dashed line) as a function of time. **(e)** Survival probability as a function of time varying the ratio a/λ from 0.05 to 0.1. The exponential decay of a single atom (dashed blue line) is shown for comparison. **(f)** Survival probability for $N = 51$ (top), $N = 201$ (middle) and $N = 1001$ (bottom), as a function of time. For each panel, various nearest neighbour atomic separations are explored, $a/\lambda = 0.08$, 0.2 and 0.3 (black to red). The horizontal dashed lines of the same colour represent the fraction of subradiant rates of all of the rates.

be observed in Fig. 3.3**(a)** and Fig. 3.5**(a)**, the dispersion relation in the subradiant part of the spectrum is approximately linear (excluding the states with momentum $p(k)$ close to $\pm\pi/a$ and near the superradiant region). Therefore, one can expect to

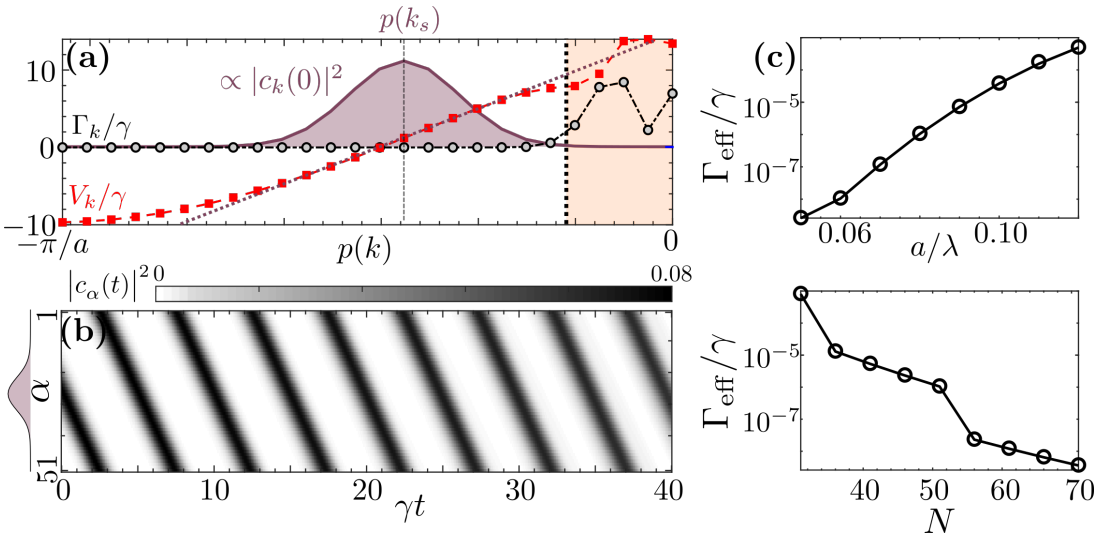

Figure 3.5: **Subradiance-protected wave packet. (a)** Decay rates Γ_k and energy V_k of each mode $|\varphi_k\rangle$ as a function of the momentum $p(k) = 2\pi k/(Na)$ for a lattice formed by $N = 51$ atoms and $a/\lambda = 0.08$. The initial wave packet's probability distribution in momentum space $|c_k(0)|^2$ (proportional to the purple solid line) is centred at $p(k_s) \approx -0.43\pi/a$, with width $\sigma_k = \pi/(16a)$. Here, the dispersion relation is approximately linear (purple dashed line to guide the eye). **(b)** Excitation probability $|c_\alpha(t)|^2$ at site α as a function of time. The initial wave packet's probability distribution in real space is sketched on the left. **(c)** Effective decay rate $\Gamma_{\rm eff}/\gamma$ of the excitation for $N = 51$ as a function of a/λ (top panel) and for $a/\lambda = 0.08$ as a function of N (bottom panel). The apparent jumps in the lower panel arise from the discrete nature of k_s: its value differs depending on system size to achieve the closest approximation of $p(k_s) \approx -0.43\pi/a$.

have lossless-propagating wave packets with a constant group velocity (given by the gradient of V_k) without dispersing. We illustrate this by initialising the system with a Gaussian wave packet centered in momentum space at $p(k_s)$ (centre of the linear dispersion manifold) and width σ_k small enough to ensure that most components of the wave packet $|c_k(0)|^2$ are located in the linear dispersion regime [see solid purple line in Fig. 3.5**(a)**]:

$$|\psi(0)\rangle = \frac{1}{\sqrt{\sqrt{2\pi}\sigma_k}} \sum_{k=1}^{N} \mathrm{e}^{-\frac{[p(k)-p(k_s)]^2}{4\sigma_k^2}} |\varphi_k\rangle. \tag{3.30}$$

In real space this is also a Gaussian wave packet

$$|\psi(0)\rangle = \sqrt{\frac{\sigma_k}{\sqrt{2\pi}}} \sum_{\alpha=1}^{N} \mathrm{e}^{-\mathrm{i}p(k_s)a(\alpha-1)} \mathrm{e}^{-\frac{(\alpha-1)^2a^2}{4/\sigma_k^2}} |e\rangle_\alpha, \tag{3.31}$$

whose probability distribution is sketched on the left hand side of Fig. 3.5**(b)**. Here, it is shown that such a wave packet travels indeed without appreciable dispersion around

the ring and we observe in this case that the wave packet only propagates in one direction. This result is achieved since the initial Gaussian wave packet only occupies a small region on the left side of the momentum space with an approximately constant gradient of V_k. Moreover, the lifetime of the excitation is extremely long: its effective decay rate Γ_{eff}, determined by fitting an exponential decay to the survival probability, is many orders of magnitude smaller than the single atom decay rate γ. A similar reduction of the decay rate Γ_{eff} is also achieved for different system sizes N and ratios a/λ, as it can be observed in Fig. 3.5**(c)**.

3.5.1 Transport at larger interatomic spacing

Let us now take a closer inspection at the transport properties of a single excitation initialised as a Gaussian wave packet in both momentum and real space for a chain of length $N = 201$. Here we will investigate the likelihood of achieving transport for larger experimentally relevant interatomic spacings (see Sec. 5.2), by analysing the decay rates and energy spectra. While one can theoretically model a system with interatomic spacing $a \ll \lambda$, experimentally there are limitations on the nearest neighbour separation due to factors such as the laser wavelengths required to trap the atoms and the ability to load the lattice traps with one atom per site. We discuss these limitations further in Chapter 5.

The following analysis allows us to identify the most appropriate region in k-space, with a subradiant manifold and linear dispersion relation, which leads to coherent propagation of a wave packet.

We calculate the eigenvalues of the dissipation and interactions matrices $\bar{\Gamma}$ and $\bar{V}$ for a ring of two-level atoms, for simplicity, with three different nearest neighbour spacings: $a/\lambda = 0.08$, 0.34 and 0.6. From the previous section, we know that a Gaussian wave packet, initialised in k-space with centre at momentum $p(k_s) \approx -0.43\pi/a$ and width $\sigma_k = \pi/(16a)$, exists within the subradiant manifold with a linear dispersion relation. We reiterate that this result still holds for $N = 201$ and $\sigma_k = \pi/(32a)$, in this case in Fig. 3.6**(a)**, where we observe the vast number of subradiant states that allow us the freedom to choose an appropriate momentum to create dispersionless propagation. With the initial state prepared in this regime, the excitation propagates around the ring for long times without losing its form or decaying. This is clear from the survival probability which remains at $P_{\text{sur}}(t) \sim 1$ over timescales that allow for the propagation of the wave packet around the ring multiple times. Here, for instance, we observe very little spreading of the wave packet over five complete cycles around the ring, with $P_{\text{sur}}(t) \sim 1$ after a time duration of $\gamma t = 100$. For comparison, the excitation in a single atom will decay to $P_{\text{sur}}(t) \sim 0.37$ in $\gamma t = 1$. If we consider a ring of strontium atoms with decay rate $\gamma = 290$ kHz, this set-up easily stores a single

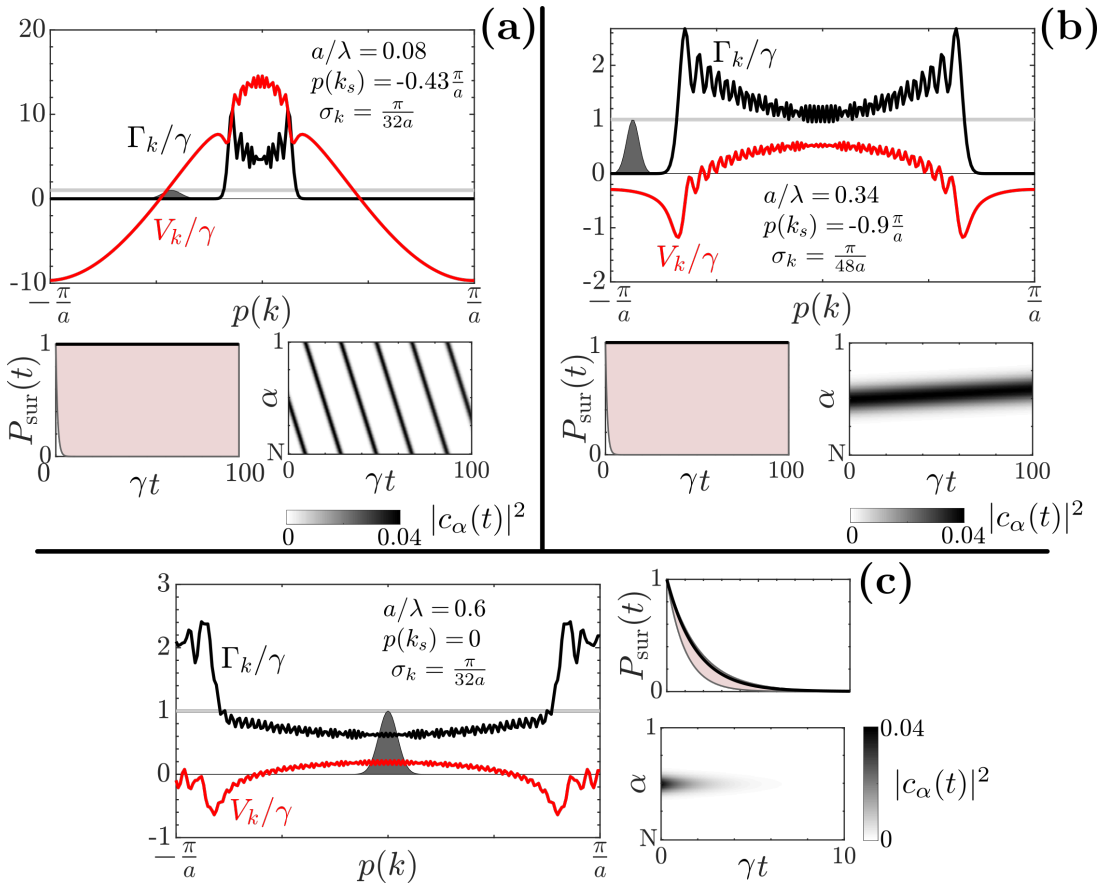

Figure 3.6: **Testing for transport in an experimentally realisable chain.** A ring of two-level atoms with nearest neighbour separations **(a)** $a/\lambda = 0.08$, **(b)** $a/\lambda = 0.34$ and **(c)** $a/\lambda = 0.6$. The top panels of **(a)** and **(b)**, and the left panel of **(c)** are the decay (black) and energy (red) spectra calculated by finding the eigenvalues of $\bar{\Gamma}$ and $\bar{V}$. The horizontal grey line is an indicator of the single atom decay rate γ, and the grey filled Gaussian wave packets are the initial states, selected in k-space, to create a subradiant wave packet, with minimal dispersion. The bottom left panels of **(a)** and **(b)** and the top right panel of **(c)** show the survival probability $P_{\rm sur}(t)$ as a function of time for the system initialised with Gaussian wave packets in real space, that correspond to those in k-space. The pink shaded regions demonstrate the bounds between the single atom decay rate (lower limit) and the most subradiant decay rate (upper limit). The populations of each atom $|c_\alpha(t)|^2$ as a function of time, for each case, are given in the bottom right panels.

excitation for timescales of the order of $\sim 100\ \mu$s. Implementation of this system would allow for light storage that is comparable to – and has potential to accompany – storage protocols achieved in experiments [123, 124].

Let us now consider a greater nearest neighbour separation $a/\lambda = 0.34$. We know from Fig. 3.3 that the inner edges of the subradiant manifold push outwards, decreasing their number. We see this also in Fig. 3.6**(b)**, where we are restricted to creating a Gaussian wave packet at the edges of k-space [$p(k_s) \approx -0.9\pi/a$]. In this example,

we have also created a narrower wave packet, with $\sigma_k = \pi/(48a)$, to ensure that the boundaries do not break the symmetry of the wave packet. While this wave packet is also very robust [$P_{\text{sur}}(t) \sim 1$ for all times] with little spatial decoherence, the propagation around the ring is greatly reduced. This result is caused by the much flatter band representing the energy of the interaction modes. V_k varies much less as a function of momentum in this subradiant regime, therefore the velocity of the wave packet is very small.

Finally, we take the separation to $a/\lambda = 0.6$. In this case, the boundaries of the subradiant manifold have pushed entirely to the edges of momentum space, as shown in Fig. 3.6**(c)**. Now, the most subradiant rates exist in the centre of the band, at $p(k) = 0$. The decay rates in this regime are indeed slower than the single atom decay rate, however we cannot expect to see infinitely long-lived states, since the most subradiant mode is $\Gamma_{k_{\min}} \approx 0.6\gamma$. The slowest decay dynamics that one could achieve are highlighted by the upper limit of the pink shaded region of the survival probability plot in Fig. 3.6**(c)**. Moreover, the accompanying interaction energy in this regime is essentially flat, which means that a Gaussian state prepared with this momentum will remain localised spatially, while decaying at a rate comparable to the single atom decay rate. These results suggest that we cannot identify an initial state that is both long-lived with respect to the single atom lifetime and exhibits transport when $a > 0.5\lambda$, and we are also unlikely to observe notable transport.

3.6 Subradiant transport on a finite 1D chain

We will now focus on subradiant excitation transport on a linear one-dimensional chain with open boundary conditions, as depicted in Fig. 3.7**(a)** [57–59, 71]. We consider the initial state to be $|e\rangle_1$, representing one excitation at the leftmost site with the rest of the atoms in the ground state. We further assume that a uniform magnetic field $\mathbf{B}$ is applied perpendicularly to the chain (which lies on the $\hat{y}$-axis) and parallel to $\mathbf{d}^0$, such that the angle extending between the direction of the magnetic field and the direction of atom separation is $\theta_{\mathbf{r}-\mathbf{B}} = \pi/2$. Once again, this ensures that our treatment of the atoms as two-level systems is valid.

The initial excitation is transported to the right of the chain via the dipole-dipole interactions [see Fig. 3.7**(b)**] until it reaches the other edge of the lattice and bounces back. As in the case of the ring, the excitation quickly disperses, and acquires a subradiant character when reaching the bulk of the chain [see Fig. 3.7**(c)**]. However, as the excitation reaches the other edge, the survival probability decays faster, accompanied by an increase of the activity. The plateau can be maintained for longer by increasing the system size, demonstrated in Fig. 3.7**(d)**, yet this does not alter the survival prob-

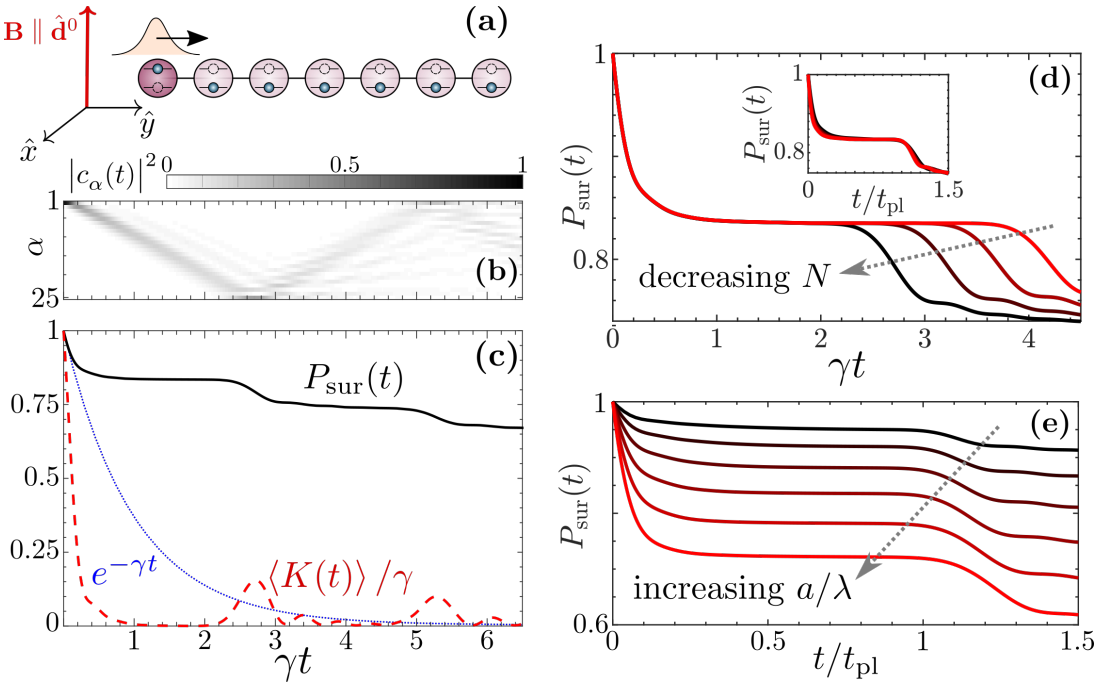

Figure 3.7: **Subradiance on a linear chain.** **(a)** Dynamics of a single excitation, initially on the leftmost atom ($\alpha = 1$) with transition dipole moment perpendicular to the chain, propagating through the chain of $N = 25$ atoms with $a/\lambda = 0.08$. **(b)** Excitation probability $|c_\alpha(t)|^2$ at each site α as a function of time. **(c)** Survival probability $P_{\text{sur}}(t)$ (solid black) and activity $\langle K(t)\rangle/\gamma$ (dashed red) as a function of time. The blue dotted line represents the survival probability in a non-interacting case. **(d)** Survival probability as a function of time for $a/\lambda = 0.08$, varying the system size N from 25 to 40. The inset displays the same results with time given in units of t_{pl} (see main text). **(e)** Survival probability as a function of time for a chain of length $N = 25$, varying the ratio a/λ from 0.05 to 0.1. The time is given in units of t_{pl}.

ability within the bulk. On the other hand, analogously with the case of the ring, the height of the plateau in $P_{\text{sur}}(t)$ can be increased by reducing the ratio a/λ, as illustrated in Fig. 3.7**(e)**. Here, in order to facilitate the comparison, the time is scaled by $t_{\text{pl}} = N/(2V_{12})$, which is approximately the time that the excitation takes to reach the middle of the chain (inversely proportional to the nearest neighbour exchange rate). The same scaling of time is provided in the inset of Fig. 3.7**(d)**, where we observe the collapse onto a single curve. This result confirms that the group velocity of the wave packet is independent of the system size.

Since the excitation has almost zero decay rate within the bulk of the chain, its lifetime is ultimately limited by the time it takes for it to reach the other boundary, i.e. by size of the system and the rate of excitation exchange (roughly given by the nearest neighbour rate V_{12}) which determines the approximate excitation transport velocity.

3.7 Storage and transport control via magnetic field switching

We aim now to freeze the transport of the wave packet and confine it in the subradiant states of the bulk by changing the value of V_{12}. This can be done by introducing an external magnetic field and adiabatically changing its direction such that the dipole moment $\mathbf{d}^0$ follows. To do so, we exploit that the strength and sign of the exchange interactions depends on the angle $\theta_{\mathbf{r}-\mathbf{B}}$. This angle extends between the direction of the transition dipole moment $\mathbf{d}^0$, hence $\mathbf{B}$, and the direction of the atomic separation $\mathbf{r}_{\alpha\beta}$ [see Fig. 3.8**(a)**].

Let us consider how this process is modelled dynamically. At $t = 0$, the external magnetic field is aligned perpendicular to the direction of the chain $\theta_{\mathbf{r}-\mathbf{B}} = \pi/2$, such that the nearest neighbour interactions are larger than the single atom decay rate γ [as shown in Fig. 3.8**(b)**, orange line], and make the excitation propagate into the bulk [see Fig. 3.9**(b)**]. When the activity reaches a minimum at $\gamma t_{\min} = 1.79$, the direction of the magnetic field is changed within the $\hat{y}$-$\hat{z}$ plane. The change of the magnetic field direction is mathematically equivalent to a rotation of the angle θ between the quantisation axis and the chain (defined in Fig. 2.1) from its initial value $\theta_{\text{in}} = \pi/2$ to a final value θ_{f}, which leads in turn to modified interactions. In particular, in order to slow down the excitation transport in the bulk, we fix the final value such that the nearest-neighbour interaction coefficient is zero, $V_{\alpha\alpha+1}(a, \theta_{\text{f}}) = 0$ [see Fig. 3.8**(b)**, blue line].

The change in direction of the magnetic field cannot be realised instantaneously, therefore we quantify the rate of rotation as κ_{B} and define the magnetic field during the rotation as

$$\mathbf{B}(t) = \frac{\Delta}{\mu_{\text{B}} g} \begin{pmatrix} 0 \\ \mathrm{e}^{-\kappa_{\text{B}} t} \\ \sqrt{1 - \mathrm{e}^{-2\kappa_{\text{B}} t}} \end{pmatrix}, \tag{3.32}$$

such that $B_y = 0,\ B_z = \frac{\Delta}{\mu_{\text{B}} g}$ when $t = 0$ and the field components tend to $B_y = \frac{\Delta}{\mu_{\text{B}} g},\ B_z = 0$ when $t \to \infty$. Recalling from Eq. (2.83) that $B_y = \frac{\Delta}{\mu_{\text{B}} g} \sin\theta_{\text{B}}$ and $B_z = \frac{\Delta}{\mu_{\text{B}} g} \cos\theta_{\text{B}}$, we determine that the time taken to rotate to a given angle $\theta_{\mathbf{r}-\mathbf{B}}$ is

$$t = \frac{-\ln(\cos\theta_B)}{\kappa_{\text{B}}} = \frac{-\ln(\cos\left(\frac{\pi}{2} - \theta_{\mathbf{r}-\mathbf{B}}\right))}{\kappa_{\text{B}}}. \tag{3.33}$$

Therefore, to achieve a rotation of $\theta_{\mathbf{r}-\mathbf{B}} = \theta_{\text{f}}$ we must rotate the magnetic field for the duration of

$$\tau = \frac{-\ln[\cos\left(\frac{\pi}{2} - \theta_{\text{f}}\right)]}{\kappa_{\text{B}}}. \tag{3.34}$$

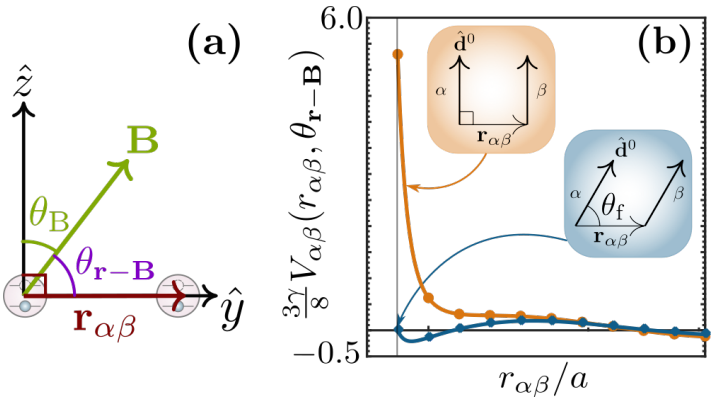

Figure 3.8: **Minimising the interaction. (a)** The angle extending from the atom separation vector to the direction of the applied external magnetic field $\theta_{\mathbf{r}-\mathbf{B}} = \frac{\pi}{2} - \theta_{\mathrm{B}}$ for all cases where the atoms are positioned in the $\hat{x}$-$\hat{y}$ plane. **(b)** Interaction strengths in the 1D chain between a pair of two-level atoms: at $t = 0$, with the dipole moments of the atoms aligned perpendicular to the atom separation (orange) and after the change of direction of the magnetic field, when the dipole moments have followed the change adiabatically and are aligned at an angle θ_{f} in order to minimise the coupling between nearest neighbours (blue).

Let us now determine an appropriate timescale for rotation of the magnetic field. In Fig. 3.9**(a)** we calculate the probability of survival as a function of both time and κ_{B} for a chain of $N = 25$ four-level atoms, detuned by $\Delta = 100\gamma$, with nearest neighbour separation $a = 0.08\lambda$. In all cases, the direction of the magnetic field is fixed until $\gamma t = 1.79$, when it is then rotated at a rate given by each value of κ_{B}. When this quantity is small ($\kappa_{\mathrm{B}} = 0.1\gamma$), the time taken to rotate to θ_{f} is very large and appears not to store the excitation at all [see the top panel of Fig. 3.9**(b)**]. By the time the angle reaches θ_{f}, the excitation has already reached the other boundary of the chain and the state loses its subradiant nature. We see an improvement in the probability of survival as κ_{B} is increased, because the storage angle is achieved while the excitation remains within the bulk. However, for even larger values of κ_{B} the survival probability begins to decline more quickly again. On closer inspection of the lower panel of Fig. 3.9**(b)**, we also observe rapidly fluctuating probabilities of excitation for individual sites. This result suggests that the rotation of the magnetic field happens too quickly for the dipole moments to follow, leading to population mixing of the three eigenstates $E_{\mathrm{B}} = \pm\Delta, 0$. Moreover, while we know that θ_{f} minimises the interaction between $|0\rangle$ states, this is not the case for the $|\pm\rangle$ states. It is also worth noting that mixing between eigenstates is more likely to occur when the detuning between levels is small and could potentially be avoided by increasing Δ.

We conclude from these results that in order to adiabatically switch the field direction, such that it is followed by the transition dipole moment of the excitation, the switching time must be $\tau \gg 1/\Delta$. By doing this, we ensure that we remain in the

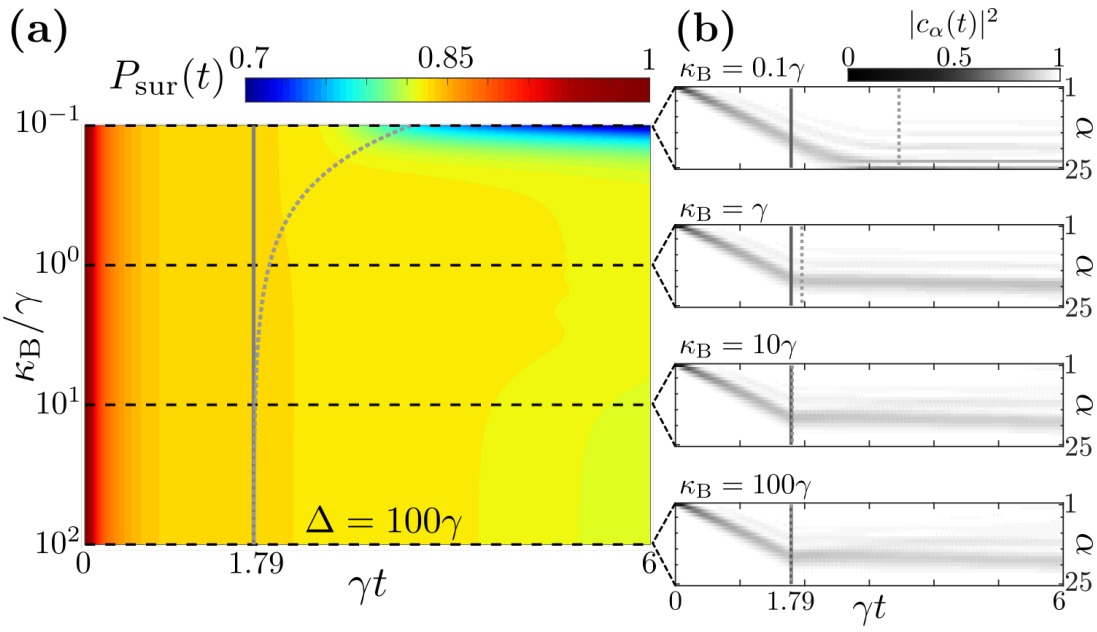

Figure 3.9: **Adiabatic magnetic field rotation.** A chain of $N = 25$ four-level atoms that extends in the $\hat{y}$-direction with interatomic spacing $a = 0.08\lambda$. The excited states are detuned by $\Delta = 100\gamma$ and the atomic dipole moments $\mathbf{d}^0$ are initially aligned to the $\hat{z}$-direction such that $\theta_{\mathbf{r}-\mathbf{B}} = \pi/2$. At $\gamma t = 1.79$ (solid grey line), the direction of the magnetic field is rotated into the $\hat{y}$-$\hat{z}$ plane until $\theta_{\mathbf{r}-\mathbf{B}} = \theta_{\mathrm{f}}$ (dotted grey line), at a rate determined by κ_{B}. **(a)** Survival probability as a function of time along the x-axis and κ_{B} along the y-axis. **(b)** Excitation probability $|c_\alpha(t)|^2$ at each site α as a function of time, for rotation rates $\kappa_{\mathrm{B}} = [0.1, 1, 10, 100]\gamma$ from top to bottom.

eigenstate of the magnetic field Hamiltonian with $E_{\mathrm{B}} = 0$. Conversely, the switch must still be quick enough to keep the excitation from leaving the bulk of the lattice, such that τ should generally be kept smaller than $1/\gamma$ (depending also on the size of the lattice and the ratio a/λ). We apply these constraints to an example protocol in Fig. 3.10 for the same parameters used in Fig. 3.7, now with detuning $\Delta = 1000\gamma$ to minimise the possibility of mixing and allow for a shorter switch time.

While the change in magnetic field does not freeze the excitation transport entirely due to the non-zero values of the exchange rates beyond nearest neighbours, it does slow it down notably, as one can see in Fig. 3.10**(a)**. Most importantly, the subradiant character of the propagation is preserved, reflected in a constant survival probability P_{sur} and vanishing activity, as shown in Fig. 3.10**(b)**.

The versatility of the system using the change in the magnetic field direction is further illustrated in Fig. 3.10**(c)**. Here, we show an example where several changes in the direction of the magnetic field allow us to switch the direction of travel of the excitation. Most importantly, the activity remains close to zero throughout all of these changes, as long as the excitation stays in the bulk of the chain.

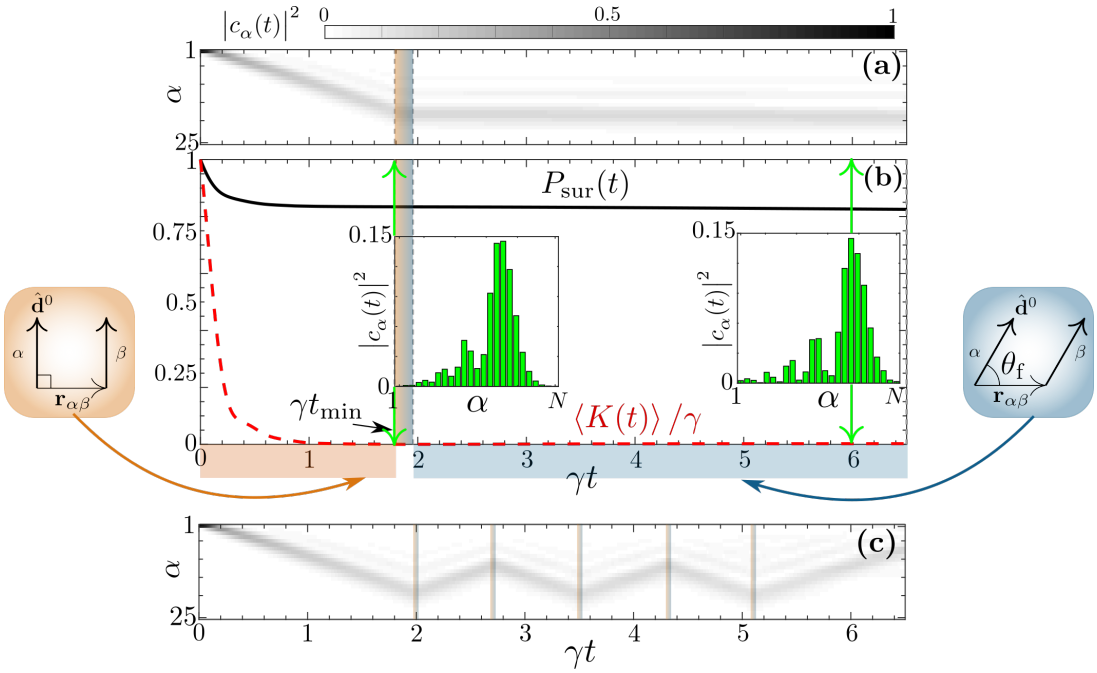

Figure 3.10: **Excitation freezing.** Dynamics of a single excitation, initially under the same conditions as Fig. 3.4. At the time when the activity is minimised, $t_{\rm min}$, the magnetic field ($\Delta = 10^3\gamma$) is rotated adiabatically (orange-blue shaded region between dashed lines) to the optimal angle for storage $\theta_{\rm f}$. **(a)** Excitation probability $|c_\alpha(t)|^2$ at each site α as a function of time. **(b)** Survival probability $P_{\rm sur}(t)$ (solid black) and activity $\langle K(t)\rangle/\gamma$ (dashed red) as a function of time. The insets show individual atom populations at $\gamma t_{\rm min} = 1.79$ and $\gamma t = 6$. **(c)** Excitation probability $|c_\alpha(t)|^2$ at each site α as a function of time, where the magnetic field is repeatedly switched from $\theta_{\mathbf{r}-\mathbf{B}} = \pi/2$ to an angle where the nearest neighbour interactions change sign and viceversa.

3.7.1 Initial state preparation

We can utilise the adaptability of the magnetic field direction further in the state preparation of the system. The above described protocol presents interesting subradiant dynamics that appear naturally from a simple initial state, however up to this point we have not made any considerations about how to initialise the system with an excitation. We will now start from the system ground state and introduce a laser driving term (as discussed in Sec. 2.6.4). This modification allows us to prepare the system with a single excitation in the leftmost atom of the chain which is closer to the experimentally realistic situation. Preparation of this initial state is complicated because of the propagation into the bulk, so we use again the fact that the interactions have an angular dependence that can be controlled with an external magnetic field.

In the previous section, we assumed that the chain is initialised with an excitation in $|0\rangle_1$, we want to model this scenario for the remainder of the section. Once

the excitation is created, we require that the external magnetic field is aligned to the dipole moment associated with the $|g\rangle \rightarrow |0\rangle$ transition, in the $\hat{z}$-direction. From our discussions in Sec. 2.6.4, we know that this corresponds to an excitation in the $E_{\mathrm{B}} = 0$ eigenstate of the magnetic field Hamiltonian. In addition to this, we assume that the precision of the laser allows single atom resolution, hence we illuminate only the first atom.

$$H'_{\mathrm{L}} = -\frac{\hbar\Omega_{\mathrm{L}}}{2}\left[\mathbf{U}_{E_{\mathrm{B}}=0}(\theta_{\mathrm{B}},\phi_{\mathrm{B}})\cdot\mathbf{b}'_1 + \mathbf{U}'_{E_{\mathrm{B}}=0}(\theta_{\mathrm{B}},\phi_{\mathrm{B}})\cdot\mathbf{b}_1\right]. \tag{3.35}$$

By introducing this Hamiltonian into the master equation, we can calculate the change to the equations of motion that describe the time evolution of the density matrix in Sec. 3.2:

$$\begin{aligned}
\dot{\rho}_{GG} =& \bar{X}\cdot\bar{\rho}_{ee} + \frac{\mathrm{i}\Omega_{\mathrm{L}}}{2}\left(\mathbf{v}^\dagger\boldsymbol{\rho}_{eG} - \boldsymbol{\rho}_{Ge}\mathbf{v}\right),\\
\dot{\boldsymbol{\rho}}_{Ge} =& \mathrm{i}\boldsymbol{\rho}_{Ge}\left(\bar{Z}^\dagger + \bar{\Delta}\right) + \frac{\mathrm{i}\Omega_{\mathrm{L}}}{2}\left(\mathbf{v}^\dagger\bar{\rho}_{ee} - \rho_{GG}\mathbf{v}^\dagger\right),\\
\dot{\boldsymbol{\rho}}_{eG} =& -\mathrm{i}\left(\bar{Z} + \bar{\Delta}\right)\boldsymbol{\rho}_{eG} - \frac{\mathrm{i}\Omega_{\mathrm{L}}}{2}\left(\bar{\rho}_{ee}\mathbf{v} - \mathbf{v}\rho_{GG}\right),\\
\dot{\bar{\rho}}_{ee} =& -\mathrm{i}\left[\bar{Z} + \bar{\Delta}, \bar{\rho}_{ee}\right] - \frac{\mathrm{i}\Omega_{\mathrm{L}}}{2}\left(\boldsymbol{\rho}_{eG}\mathbf{v} - \mathbf{v}^\dagger\boldsymbol{\rho}_{Ge}\right),
\end{aligned} \tag{3.36}$$

where the contribution due to the laser driving is contained in the additional red terms highlighted. Here, we have used

$$\mathbf{v} = \begin{pmatrix} 1\\0\\0\\\vdots\\0\end{pmatrix} \otimes \mathbf{U}_{E_{\mathrm{B}}=0}(\theta_{\mathrm{B}},\phi_{\mathrm{B}}), \tag{3.37}$$

which is a vector of length $3N$, defined to ensure that there is only action due to the laser driving on the first atom; the first factor in the tensor product is an $(N\times 1)$ vector containing zeros representing non-driven atoms and a one in the position of the driven atom. Finally, throughout the dynamics we rotate the magnetic field along the $\hat{y}$-$\hat{z}$ plane, such that Eq. (2.89) reduces to

$$\mathbf{U}_{E_{\mathrm{B}}=0}(\theta_{\mathrm{B}},\pi/2) = \frac{1}{\sqrt{2}}\begin{pmatrix}\sin\theta_{\mathrm{B}}\\ -\sqrt{2}\mathrm{i}\cos\theta_{\mathrm{B}}\\ \sin\theta_{\mathrm{B}}\end{pmatrix}. \tag{3.38}$$

In Sec. 3.2, due to the decoupling between the ground state and excited state dynamics, we were able to consider a reduced density matrix that only evolved the excited sector. The laser driving terms break this condition, therefore we must now evolve the entire density matrix. Without a clear analytical solution, we calculate the time evolution

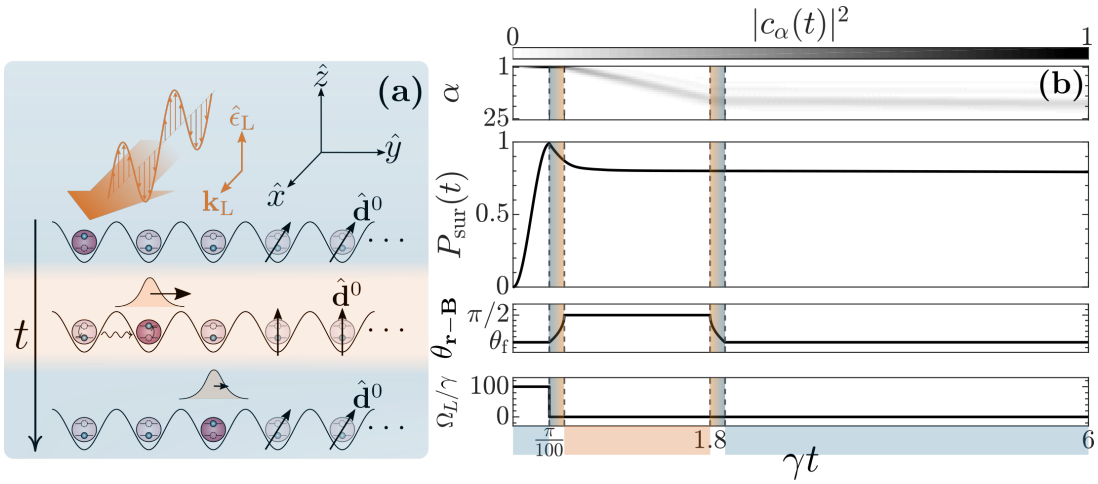

Figure 3.11: **State Preparation.** The system dynamics for a chain of $N = 25$ atoms and $a/\lambda = 0.08$ where the leftmost atom is initially driven by a laser with $\omega_{\rm L} = \omega_{\rm a}$ and Rabi frequency $\Omega_{\rm L} = 100\gamma$. **(a)** A π-pulse is applied to the end atom to populate the excited state, with the atom dipole moments initially oriented at an angle $\theta_{\rm f}$ from the direction of the chain. The external magnetic field defining the dipole direction (with $\Delta = 100\gamma$) is then adiabatically rotated to the $\hat{z}$-axis allowing propagation through the chain. Once the excitation is within the bulk, the magnetic field is rotated back to $\theta_{\rm f}$ for storage. **(b)** From top to bottom the panels demonstrate the excitation probability $|c_\alpha(t)|^2$ at site α, survival probability $P_{\rm sur}(t)$, the angle $\theta_{\mathbf{r}-\mathbf{B}}$ between the external magnetic field (and dipole moment $\mathbf{d}^0$) and the direction of atom separation, and the Rabi frequency of the laser, as a function of time. The orange and blue shading represent the dipole angles as defined in Fig. 3.10. Note that the linear timescale for the laser driven sector has been extended in order to observe the driving dynamics.

of the density matrix using numerical methods. Using the fourth order Runge-Kutta method, the time evolution of each sector of the density matrix is calculated by starting from $t = 0$ and then determining its change at a small increment of time later. Completing this iteratively produces the time evolved dynamics [125].

Intuitively, the simplest way to drive a state that evolves only through the $|0\rangle$ states would be to align the magnetic field in the $\hat{z}$ direction such that the $E_{\rm B} = 0$ state corresponds to $|0\rangle$. However, in order to recreate the initial state that we have explored in previous sections, we must find a way to drive the first atom only, without the excitation propagating to neighbouring atoms before we have achieved a starting survival probability of $P_{\rm sur}(t) = 1$. In parallel with this condition, we must also ensure that we do not create an initial state with more than one excitation. The dynamics that we have derived are only valid in the single excitation sector, which means that we must ensure that we only drive the system to this limit. We can ascertain that we meet these conditions by driving the leftmost atom with all dipole moments aligned to the magic angle $\theta_{\rm f}$, introduced in Sec. 3.7 [see Fig. 3.11**(a)**]. Here, we minimise the interactions between atoms such that the excitation being created in the first atom remains there

for the duration of the laser driving. By assuring that we are only populating the first atom, we are then able to determine the appropriate laser driving time required. For a single atom, we can apply a π-pulse which inverts the atom population from the ground to the excited state. The duration of this type of pulse is related to the laser Rabi frequency such that $t_\pi = \pi/\Omega_{\mathrm{L}}$.

Once the π-pulse has been applied, the angle of the external magnetic field can be adiabatically rotated back into alignment with the $\hat{z}$-axis. At this point, we have created the initial excitation in the first atom and the dynamics corresponds to the one of a chain of two-level atoms with the dipole moment of the $|g\rangle \rightarrow |0\rangle$ transition. The laser driving is then switched off and we achieve the same "storage" protocol as before in Fig. 3.11**(b)**.

It is worth noting that these calculations were performed using $\Omega_{\mathrm{L}} = 100\gamma$ which might be too large when considering an experimentally realistic situation. By implementing a high Rabi frequency, the excitation is created very quickly in comparison to the timescale associated with dissipation, hence allowing us to reach $P_{\mathrm{sur}} \sim 1$. A smaller Rabi frequency would mean that the time taken to drive the system would need to be increased. However, we find that reducing the Rabi frequency by an order of magnitude ($\Omega_{\mathrm{L}} = 10\gamma$), while preventing us from exciting the system entirely to $P_{\mathrm{sur}}(t) = 1$, still allows us to store the excitation with a very similar survival probability of

$$\frac{P_{\mathrm{sur}}^{\Omega_L=10\gamma}(6/\gamma)}{P_{\mathrm{sur}}^{\Omega_L=100\gamma}(6/\gamma)} = \frac{0.7844}{0.7924} = 0.9899. \tag{3.39}$$

Further investigation is required here to determine an appropriate range of values for the Rabi frequency that can excite the system to a high enough population, for high fidelity storage, whilst modelling physical lasers with sensible driving timescales.

3.8 Disorder

We now briefly consider the effect of disorder on the subradiant transport discussed in the previous sections. In particular, we consider the disorder introduced due to the finite width of the external wave function of each atom, which we model as a three-dimensional Gaussian with width σ centered in the respective lattice sites. We take this approach because we assume that each atom sits at the bottom of a potential well within the optical lattice such that each well can be modelled as a harmonic oscillator, and the wave function describing an atom's position within a harmonic oscillator is given by a Gaussian distribution. We will consider the quantum nature of the atom positions in Chapter 4, however here we make a "classical" approximation of this disorder as an initial investigation by selecting three random numbers from a normal

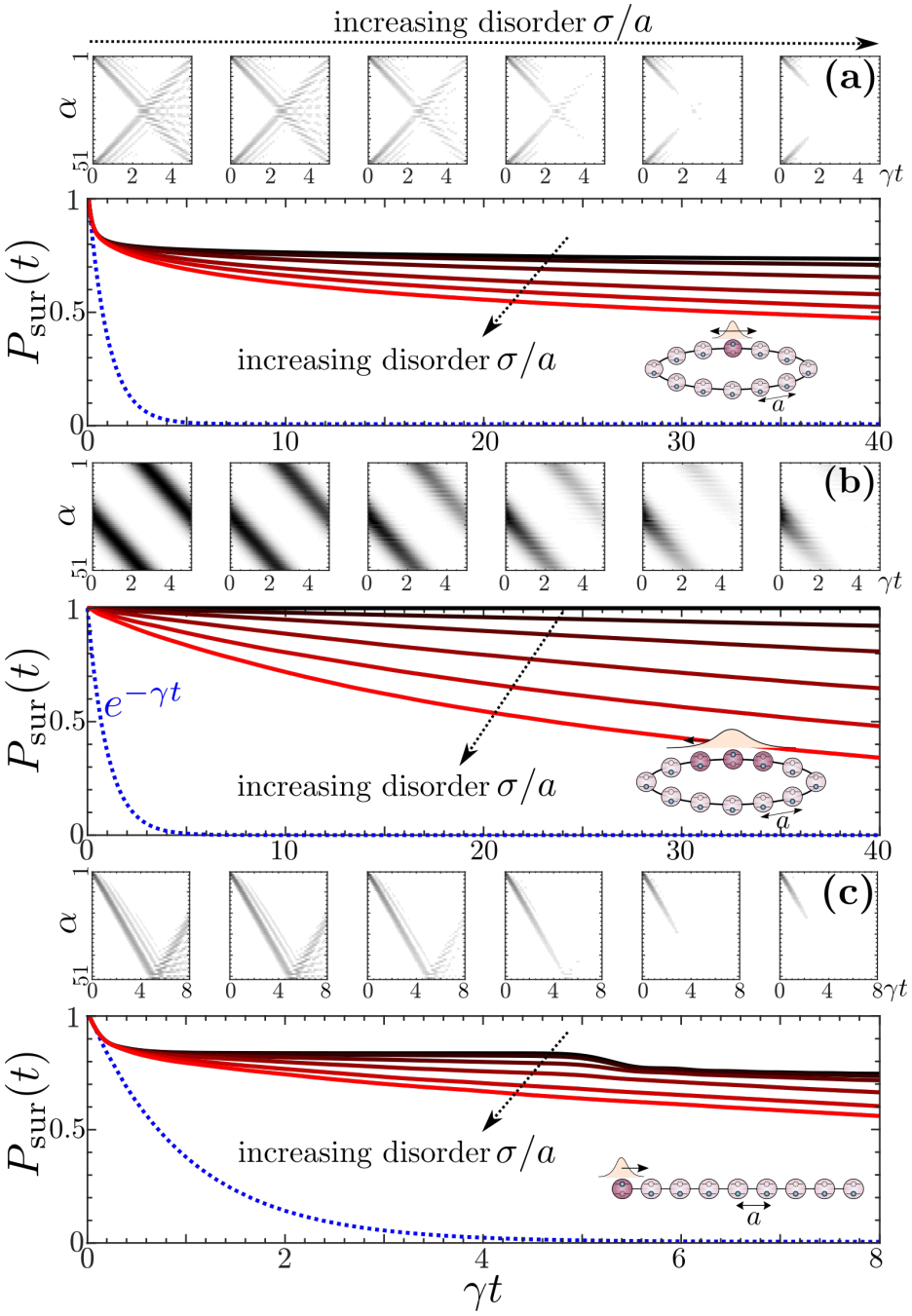

Figure 3.12: **Disorder.** Survival probability for an initial excitation on a chain of $N = 51$ atoms and $a/\lambda = 0.08$ **(a)** on a single site on a ring lattice, **(b)** on an extended gaussian wave packet on a ring lattice and **(c)** on a single site on a linear 1D lattice. All panels show the excitation probability $|c_\alpha(t)|^2$ at site α as a function of time and the survival probability without disorder (leftmost panel, black solid line) and in the presence of disorder (rest of panels and solid red lines). The disorder is modelled by a gaussian distribution of the positions of the atoms around the centre of each site with widths $\sigma = 0.01a \rightarrow 0.05a$ (average over 100 iterations of the disorder). The blue dashed line in all cases represents an exponential decay with single atom decay rate γ for comparison.

distribution for each atom: each number acts as a shift in the atomic position away from the centre of its site in each of the three directions. The dynamics is determined for this set of randomly shifted atomic positions and we perform this step over many iterations. The dynamics is then calculated as an average over all iterations of disorder.

Since the long-ranged exchange interactions $\bar{V}$ [given by Eq. (2.53)] are functions of the separation between the atoms, the uncertainty in the atomic positions translates into disorder in the hopping rates in the exchange Hamiltonian H given by Eq. (2.55). This kind of positional disorder in Hamiltonians with long-ranged hopping has been recently studied and found to give rise to localisation [117]. Consistently with this, we find that as we increase σ the eigenstates of the Hamiltonian become localised, inhibiting transport. This can be seen in the top panels of Figs. 3.12**(a)**, **(b)** and **(c)**, where we show the excitation probability $|c_\alpha(t)|^2$ as a function of time for increasing disorder (ratio σ/a) from left to right.

Moreover, in each lower panel in Fig. 3.12**(a)**, **(b)** and **(c)** one can observe that, while increasing disorder has a detrimental effect on the subradiant state manifold, in all cases considered the excitation features lifetimes dramatically longer than the ones of an individual atom. We predict that this robustness arises because we are not exciting a single subradiant state, but many.

We explore the effect of disorder further in Chapter 4. However, instead of modelling the exact position of each atom by randomly choosing a Gaussian distributed offset from the site, we define the atomic positions to have an extension in space represented by Gaussian motional wave functions.

3.9 1D chain between metallic surfaces

There are a number of experimental challenges to overcome when considering the realisation of such long lived excitation storage in a dissipative system. One is to achieve a sufficiently small ratio a/λ such that highly subradiant states emerge. An example of such a system, using a transition in the triplet series of alkaline earth metal atoms with a particularly long wavelength (2.6 μm in strontium), was introduced in Reference [14]. With a single atom decay rate of $\gamma = 290$kHz for the ${}^3P_0 - {}^3D_1$ transition, a chain of strontium atoms would require quite fast switching times τ for the magnetic field direction of the order of microseconds or tens of microseconds (longer switching times are possible for a larger system size and ratio a/λ, as the excitation takes longer to leave the bulk). The trapping of these alkaline earth metal atoms is currently realised experimentally both in optical lattices [126, 127] and tweezer arrays [128]. Even smaller ratios a/λ can be achieved by using Rydberg states, where the transition wavelengths are much longer than in low-lying states. Using rubidium-87

as an example, transition wavelengths on the order of $\lambda \sim 1$ mm, associated with the interactions between Rydberg atoms in an $n = 60$ state [129, 130], far exceed the wavelength of the low-lying D2 transition $\lambda = 780$ nm. An alternative approach that allows subradiant states to emerge for large ratios a/λ is changing the radiation field's boundary conditions by placing, e.g., a surface or a waveguide [53, 58, 131–137] near the atoms, which in turn modifies the exchange interaction and dissipation.

We explore this phenomenon for a one-dimensional chain of atoms brought into proximity with metallic surfaces. When a chain of atoms is brought close to a metallic surface, we observe a modification to the coherent interaction and collective dissipation in the atomic system, due to the surface plasmon polaritons (SPPs) that occur at the air-metal interface. These SPPs are electromagnetic waves that are guided along the interface. The emitted radiation from the decay of an excitation near to the surface can couple to the surface plasmon polaritons that carry energy between the atoms. This radiation can in turn be reabsorbed. A derivation of the modified coupling and dissipation coefficients is presented in Reference [53]. The remainder of this section outlines our specific contribution to this paper.

Here, we consider a linear chain of atoms with system size $N = 20$ and atomic spacing $a/\lambda = 0.08$. In the same manner as the previous examples, we may start with a four-level atom description which is reduced to the two-level picture by applying an external magnetic field to detune the energy levels and lift the degeneracy. In this case, we consider a situation where the dipole moment for the $|g\rangle \rightarrow |0\rangle$ transition is aligned parallel to the direction of the chain ($\mathbf{d}^0||\hat{y}$), and the state is initialised with a single excitation in the leftmost atom [see Fig. 3.13**(a)**].

From Fig. 3.13**(b)** and the solid black line in Fig. 3.13**(e)**, we observe that the dynamics in free space - with parallel dipole moments - transports the excitation across the chain while maintaining a higher survival probability in comparison to the perpendicular dipole moment aligned explored in Fig. 3.7. Additionally, the top panel of the left inset also demonstrates that this transport is indeed still dispersive.

Let us now consider the effect of bringing the chain close to metallic surfaces. Reference [53] explores how the presence of a metallic or dielectric surface changes the radiation field to which the atoms are coupled, and determines the modified long-range coherent interactions and the dissipative nature of collective atomic systems. Here, we use the modified coefficients $V_{\alpha\beta}$ and $\Gamma_{\alpha\beta}$ to simulate the excitation dynamics for the chain in the presence of one silver surface [Fig. 3.13**(c)**] and in the presence of two with the chain placed between them [Fig. 3.13**(d)**]. The relevant experimental parameters are provided in [53].

For the single surface case, we observe further improvement on the transport efficiency from the higher survival probability, demonstrated in Fig. 3.13**(c)**. Along with this, we still see features of the collective character in the form of faster decay rates at

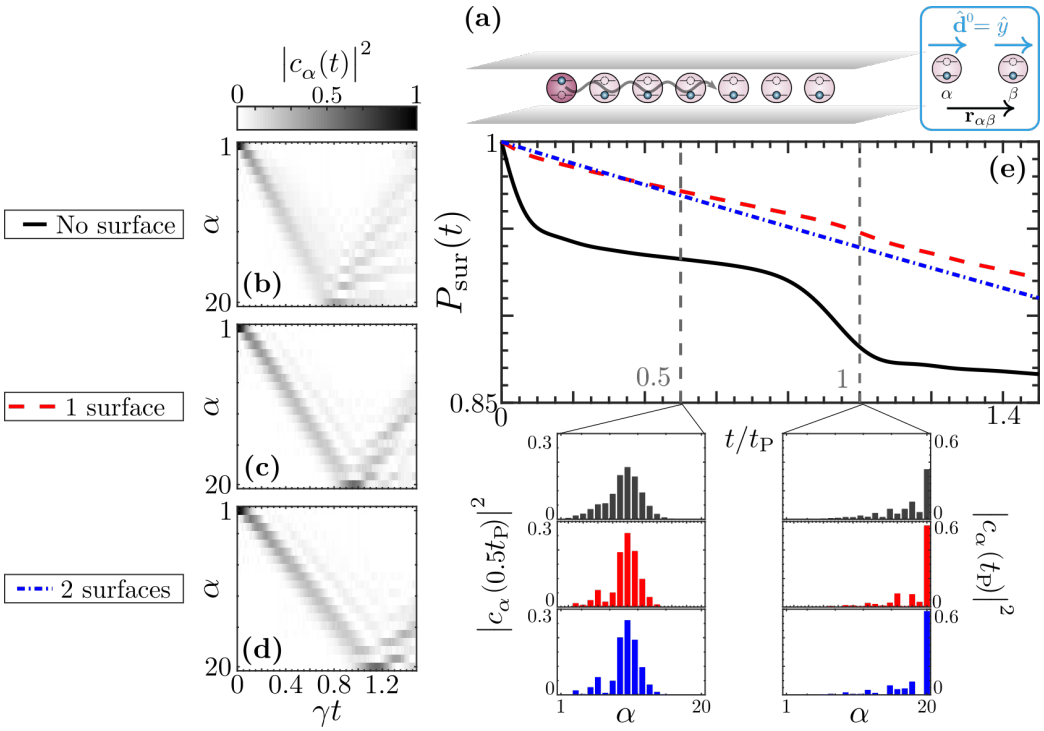

Figure 3.13: **Modified interactions between two surfaces.** **(a)** A one-dimensional linear chain of $N = 20$ two-level atoms with nearest neighbour separation $a/\lambda = 0.08$. The transition dipole moment $\mathbf{d}^0$ is parallel to the direction of the chain (given by $\hat{\mathbf{r}}_{\alpha\beta}$). The leftmost atom is excited with the rest in the ground state. The population of each atom is plotted as a function of time for **(b)** the chain in free space (black); **(c)** the chain placed parallel to one silver surface at a distance of $z = 100\text{nm}$ (red); **(d)** the chain placed equidistantly between two parallel silver surfaces with $z = 100\text{nm}$ (blue). **(e)** Survival probability for each case as a function of time scaled by $t_{\rm P}$: the time taken for the excitation to propagate and maximally excite the rightmost atom. The insets show the excitation probability $|c_\alpha(t)|^2$ at site α midway through transport ($t = 0.5t_{\rm P}$), and once the excitation has reached the other end of the chain ($t = t_{\rm P}$).

the boundaries in comparison to the decay within the chain bulk. In contrast, while the presence of two surfaces improves the survival probability, we do not observe equivalent collectivity; the survival probability is fitted with an exponential decay, and the results of [53] determine that this is simply due to an effective decay rate smaller than the single atom decay rate.

A comment can also be made on the speed of transport across the chain. We have scaled the time in Fig. 3.13**(e)** by $t_{\rm P}$ which represents the time taken for the excitation to propagate to the other side of the chain. We define this by extracting the time corresponding to the highest population of the N-th atom. For reference, a chain of $N = 20$ atoms in free space with perpendicular dipole alignment to the chain direction has $\gamma t_{\rm P} = 2.15$. In free space, with parallel alignment [Fig. 3.13**(b)**], we find $\gamma t_{\rm P} = 0.82$; in the presence of one surface [Fig. 3.13**(c)**] $\gamma t_{\rm P} = 0.97$; and with two

surfaces [Fig. 3.13**(d)**] $\gamma t_{\mathrm{P}} = 1.15$. So while changing to a parallel alignment in free space decreases the transport time, by modifying the radiation field with the presence of metallic surfaces, one can slow the transport to some extent.

3.10 Conclusions and outlook

With the aim of exploring collective dynamics for an ensemble of atoms, we have introduced a number of restrictions on the system geometry and excitation number in order to derive the state equation of motion.

We have investigated the transport of an excitation in a one-dimensional atomic lattice that occurs due to the coupling of the atoms to the radiation field. In particular, we have shown that there is a high dimensional subradiant manifold that allows for dispersionless transport of wave packets that is robust against positional disorder.

The question of whether excitation transport persists at interatomic spacing relevant to experiments was explored and answered from a theoretical understanding. We confirmed that the energy spectra and collective decay rates would not allow for both dispersionless and dissipationless transport.

Our investigation into disorder, while providing a general picture of how the system may respond, will be extended in Chapter 4. Here we have modelled the disorder as a classical uncertainty in the atomic positions, whereas Chapter 4 presents the possibility of modelling disorder intrinsically on a more fundamental level.

We briefly explored experimental difficulties associated with the requirement of close proximity between emitters, and provided examples of how this may alleviated. Another experimental challenge is the preparation of the subradiant wave packets. In particular, preparing states with one excitation localised on one or a few sites will require single-site resolution and addressability, which has been achieved experimentally in optical lattices and tweezer arrays [138–142]. Moreover, creating a wave packet with a linear dispersion relation will require a phase imprinting mechanism, which may be challenging to implement experimentally.

Chapter 4
Robustness of subradiance against motion and disorder

4.1 Introduction

So far in this thesis, we have derived the appropriate master equation to model the dynamics of many-body atomic systems separated by lengthscales shorter than or comparable to the transition wavelength associated with the atoms. This regime is nowadays in reach experimentally, e.g. trapping of atomic gases in cavities [24], magneto-optical traps [21, 22, 26, 28, 143, 144], optical lattices [36, 59, 91] and optical tweezers [139–142]. This has motivated a growing interest in utilising the collective effects for quantum information purposes, such as exploiting subradiance for the long-lived storage and transport of light [36, 53, 55, 57, 106, 108, 115, 145]. However, such applications require robustness against, for instance, positional disorder and atomic motion [146]. Various experimental groups have investigated the impact that temperature has on collective effects that arise naturally in dilute thermal gases of atoms [147, 148]. Current findings suggest that, for a dilute cloud of rubidium-87 atoms trapped in a MOT, subradiance is robust up to temperatures of several millikelvins. With these experimental results, there is demand for a theoretical understanding to shed light on the dynamics in these systems. If subradiance is robust, insight into the cause would create the possibility of optimising light storage, for example, by exploiting specific geometries and initial configurations which promote the survival of the desired state. Progress has been made in this area both classically [149] and for quantised motion [77].

In this chapter, following the formalism presented in Reference [77], atomic motion and positional disorder are introduced at the level of the Hamiltonian. We introduce this Hamiltonian in Sec. 4.2, where we apply a similar methodology to the one described in Sec. 2.3 to systematically derive a quantum master equation under the Born and Markov approximations by treating the external atomic degrees of freedom as part of the bath. We reiterate the appearance of super- and subradiant emission of photons for the case neglecting external atomic motion, in Sec. 4.2.1.

The master equation for quantum systems, where we now incorporate the atomic

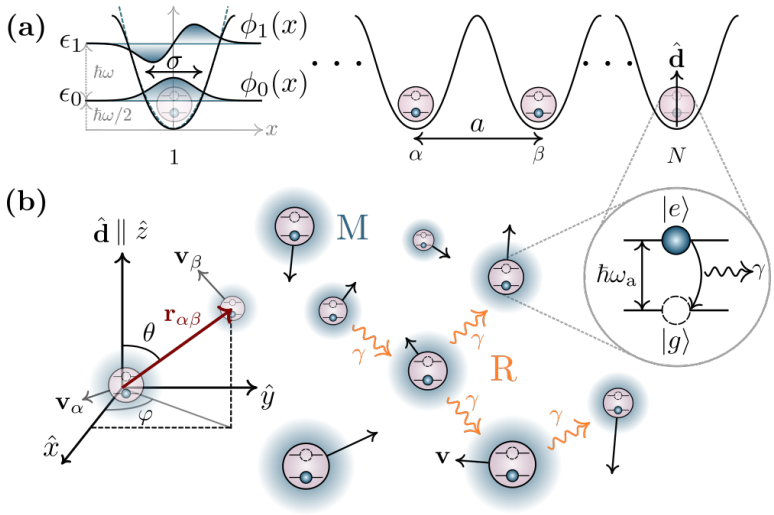

Figure 4.1: **The system.** A cold ensemble of two-level atoms with single atom decay rate γ and atomic dipole moments $\mathbf{d}$ directed along the $\hat{z}$-direction. **(a):** When the atoms are trapped in a one-dimensional lattice, fluctuations in the atomic position are determined by the trapping frequency, ω. Each trap is modeled as a quantum harmonic oscillator, with states $\phi_0(\mathbf{r})$ and $\phi_1(\mathbf{r})$ occupied in a statistical mixture. **(b)** A three-dimensional disordered gas, where the atoms have temperature-dependent velocities.

motional effects, is generalised for the examination of a variety of geometries, such as a chain of atoms trapped within an optical lattice, and dilute thermal gases in magneto-optical traps (see Fig. 4.1). We build on the results presented in Chapter 3 for a one-dimensional chain of atoms by studying the impact of the residual motion of atoms on the onset of collective behaviour (in Sec. 4.3). Here, we specifically consider the form of the atomic motional states to be well represented by three-dimensional harmonic oscillators, and the existence of collective emission is investigated for different temperatures. We first assume cold enough temperatures for all atoms to exist in their motional ground state, before increasing the temperature. Ultimately, the atoms will occupy higher energy oscillator states when the temperature is larger. The requirement for a description including a greater number of motional energy levels is investigated as a function of temperature.

In Sec. 4.4, we continue to explore how the form of the master equation must be adapted for the case of indistinguishable atoms. This is particularly important, for instance in an optical lattice, if the wells overlap and allow hopping between sites. We therefore make this modification to the description of the atoms, in order to derive an equivalent master equation.

Moreover, we consider the atoms as indistinguishable when all atoms are in the same trap, as is the case in a 3D MOT. We introduce this case in Sec. 4.4.1, and explore how the master equation changes depending on the description of the atoms within a single trap. Once again, we make various considerations regarding the temperature of

the gas. We conclude with an outlook for this project, which is currently open-ended.

4.2 System and master equation

We consider a system of N atoms interacting with the free three-dimensional radiation field (in the same way as Chapter 2). The dynamics is determined by the Hamiltonian

$$H = H_{\rm a} + H_{\rm f} - \sum_{\alpha=1}^{N} \mathbf{D}_\alpha \cdot \mathbf{E}(\mathbf{r}_\alpha, t). \tag{4.1}$$

This equation is identical to Eq. (2.17), however the first term, $H_{\rm a} = H_{\rm a}^{\rm in} + H_{\rm a}^{\rm ex}$, now models the dynamics of the internal and external atomic degrees of freedom. For simplicity, the electronic structure of each atom is modelled here as a two-level system (see Fig. 4.1), such that the internal atomic degrees of freedom [identical to Eq. (2.18)] are represented by

$$H_{\rm a}^{\rm in} = \frac{\hbar\omega_{\rm a}}{2} \sum_{\alpha=1}^{N} \sigma_z^\alpha. \tag{4.2}$$

The external atomic dynamics is determined by

$$H_{\rm a}^{\rm ex} = \sum_{\alpha=1}^{N} \left[\frac{\mathbf{p}_\alpha^2}{2M} + V(\mathbf{r}_\alpha) \right], \tag{4.3}$$

where $\mathbf{r}_\alpha$ and $\mathbf{p}_\alpha$ represent the centre of mass position and momentum operators for each atom, respectively, and $V(\mathbf{r}_\alpha)$ is the external trapping potential experienced by the atoms. The second term in Eq. (4.1) contains the radiation field degrees of freedom, given by Eq. (2.22), and the final term of Eq. (4.1) represents the interaction between atoms and the radiation field within the dipole approximation. The interaction also remains unchanged from the case described in Sec. 2.3, with the exception that we must now be careful with the ordering of terms containing $\mathbf{r}_\alpha$ since these are now operators for the external atomic degrees of freedom.

Our goal is to obtain an equation of motion that describes the internal dynamics of the atoms only, treating the internal degrees of freedom as the system and both the external atomic motion and the radiation field as a bath:

$$\begin{aligned} H_{\rm s} &= H_{\rm a}^{\rm in}, \\ H_{\rm b} &= H_{\rm a}^{\rm ex} + H_{\rm f}. \end{aligned} \tag{4.4}$$

To do so, it is convenient to first switch into the interaction picture with respect to $H_{\rm s} + H_{\rm b}$. Using the methodology presented in Sec. 2.1, we make this transformation to the interaction picture using the unitary operator $U(t) = U_{\rm s}(t)U_{\rm b}(t) = U_{\rm a}^{\rm in}(t)U_{\rm a}^{\rm ex}(t)U_{\rm f}(t)$

such that the Hamiltonian after the transformation reads

$$V_I(t) = -\mathrm{i}\hbar \sum_{\alpha=1}^{N} \sum_{\mathbf{k},\lambda} (\sigma_+^\alpha \mathrm{e}^{\mathrm{i}\omega_\mathrm{a} t} + \sigma_-^\alpha \mathrm{e}^{-\mathrm{i}\omega_\mathrm{a} t}) \left\{ g_{\mathbf{k}\lambda} a_{\mathbf{k}\lambda} \mathrm{e}^{\mathrm{i}[\mathbf{k}\cdot\mathbf{r}_\alpha(t) - \omega_\mathbf{k} t]} - \mathrm{H.c.} \right\}, \tag{4.5}$$

with the position operators becoming time-dependent

$$\mathbf{r}_\alpha(t) = \mathrm{e}^{\mathrm{i}H_\mathrm{a}^\mathrm{ex} t/\hbar} \mathbf{r}_\alpha \mathrm{e}^{-\mathrm{i}H_\mathrm{a}^\mathrm{ex} t/\hbar}. \tag{4.6}$$

Introducing this Hamiltonian into a Liouville-von Neumann equation for the full density matrix $\rho_I(t)$, formally integrating over time, and tracing over the bath degrees of freedom, yields an analogous equation to Eq. (2.8)

$$\dot{\rho}(t) = -\frac{1}{\hbar^2} \int_0^t \mathrm{d}t' \, \mathrm{Tr}_\mathrm{b} \left\{ [V_I(t), [V_I(t'), \rho_I(t')]] \right\}, \tag{4.7}$$

where $\rho(t) = \mathrm{Tr}_\mathrm{b} \{\rho_I(t)\}$ is the density matrix for the internal atomic degrees of freedom. It is now assumed that $\rho_I(t') \approx \rho(t') \otimes \rho_\mathrm{b}$ is valid when the coupling between the bath and the internal degrees of freedom is weak, such that the bath density operator is not significantly changed by the coupling. This is indeed the case for the radiation field, and also the external motion of the atoms, since the temperature of the atomic gas does not change appreciably during the timescale of the internal dynamics. Moreover, we also assume that the correlation time of the bath is much shorter than the one of the atomic dynamics. Within these (Born-Markov) approximations, we can substitute in the right hand side of (4.7) $\rho_I(t') \to \rho(t) \otimes \rho_\mathrm{b}$ and bring the upper limit of the integral $t \to \infty$. Finally, substituting $t' = t - \tau$ leads to

$$\dot{\rho}(t) = -\frac{1}{\hbar^2} \int_0^\infty \mathrm{d}\tau \, \mathrm{Tr}_\mathrm{b} \left\{ [V_I(t), [V_I(t-\tau), \rho(t) \otimes \rho_\mathrm{b}]] \right\},$$

which, after the rotating wave approximation, can be rewritten as

$$\begin{aligned} \dot{\rho} = \sum_{\alpha,\beta=1}^{N} \Big\{ & X_{\alpha\beta}(\omega_\mathrm{a}, t) \left[\sigma_-^\beta \rho \sigma_+^\alpha - \sigma_+^\alpha \sigma_-^\beta \rho \right] + \\ & X_{\alpha\beta}(-\omega_\mathrm{a}, t) \left[\sigma_+^\beta \rho \sigma_-^\alpha - \sigma_-^\alpha \sigma_+^\beta \rho \right] + \mathrm{H.c.} \Big\}, \end{aligned} \tag{4.8}$$

where we treat the time-dependence of the internal system density matrix implicitly $\rho(t) \to \rho$. Here, $X_{\alpha\beta}(\omega, t) = \int_0^\infty \mathrm{d}\tau \; \mathcal{C}_{\alpha\beta}^\mathrm{b}(\mathbf{k}, t, \tau) \mathrm{e}^{\mathrm{i}\omega\tau}$ with the bath correlation function $\mathcal{C}_{\alpha\beta}^\mathrm{b}(\mathbf{k}, t, \tau) = \mathrm{Tr}_\mathrm{b} \{B_\alpha(t) B_\beta(t-\tau) \rho_\mathrm{b}(0)\}$, where we have used the definition [77]

$$B_\alpha(t) = \sum_{\mathbf{k},\lambda} \left\{ -\mathrm{i} g_{\mathbf{k}\lambda} a_{\mathbf{k}\lambda}^\dagger \mathrm{e}^{-\mathrm{i}[\mathbf{k}\cdot\mathbf{r}_\alpha(t) - \omega_\mathbf{k} t]} + \mathrm{H.c.} \right\}. \tag{4.9}$$

In order to find an explicit expression for $X_{\alpha\beta}(\omega, t)$, we assume that the state of the bath can be separated as $\rho_{\mathrm{b}} = \rho_{\mathrm{F}} \otimes \rho^{\mathrm{ex}}$. The correlation function $\mathcal{C}^{\mathrm{b}}_{\alpha\beta}$ can then be further simplified by assuming that the radiation field is in the vacuum state. In this case the only non-zero expectation value is $\langle a_{\mathbf{k}\lambda} a^{\dagger}_{\mathbf{k}'\lambda'} \rangle = \delta_{\mathbf{k}\mathbf{k}'}\delta_{\lambda\lambda'}$ which reduces the bath correlation function to

$$X_{\alpha\beta}(\omega_{\mathrm{a}}, t) = \sum_{\mathbf{k},\lambda} |g_{\mathbf{k}\lambda}|^2 \int_0^{\infty} \mathrm{d}\tau \, C_{\alpha\beta}(\mathbf{k}, t, \tau) \mathrm{e}^{-\mathrm{i}(\omega_{\mathbf{k}} - \omega_{\mathrm{a}})\tau}, \tag{4.10}$$

where $C_{\alpha\beta}(\mathbf{k}, t, \tau) = \langle \mathrm{e}^{\mathrm{i}\mathbf{k}\cdot\left[\mathbf{r}_{\alpha}(t) - \mathbf{r}_{\beta}(t-\tau)\right]} \rangle_{\mathrm{ex}}$ is the motional correlation function, and $\langle \cdot \rangle_{\mathrm{ex}}$ denotes the expectation value over the external (motional) atomic degrees of freedom.

4.2.1 In the classical limit

Until now, we have considered the case where the trapping potential is not explicitly taken into account and the external motion of the atoms is considered frozen throughout the dynamics. Here, the time-dependence of the motional correlation function can be neglected, such that

$$C^{\mathrm{cl}}_{\alpha\beta}(\mathbf{k}) = \mathrm{e}^{\mathrm{i}\mathbf{k}\cdot\mathbf{r}_{\alpha\beta}}, \tag{4.11}$$

with separation vector $\mathbf{r}_{\alpha\beta} = \mathbf{r}_{\alpha} - \mathbf{r}_{\beta}$. We give this quantity a superscript to describe it as "classical" i.e. the atomic positions are exactly known (fixed in place). Substitution of this correlation function in (4.10) and subsequently in (4.8) results in the well known quantum master equation for the internal degrees of freedom, recovering Eq. (2.51) [12, 13].

The scenario presented above has been shown to be very useful for the theoretical study of subradiance, superradiance and dipole-dipole interactions and their applications [16, 57, 88]. However, this idealised scenario is not well-suited for the study of these effects in experimentally realistic situations. For example, in the case of a cold atomic gas trapped in an optical lattice, for finite values of the trap width the (quantised) motional state has an extension in space associated that needs to be considered. The atomic positions are not fixed and have an uncertainty determined by the size of the trap. On the other hand, in the case of a thermal gas of atoms at non-zero temperature, we cannot assume the motion of the atoms to be frozen: it is not given that the atoms remain in their initial positions throughout the internal dynamics. In the following, we apply the framework presented in this section to these two specific examples, chosen due to their experimental relevance [21, 28, 150].

4.3 Atoms on a lattice: quantum motional states

We consider now that N atoms are tightly trapped in the sites of an optical lattice or a tweezer array (for any regular atomic arrangement), such that each site is occupied by a single atom, and the trap width is narrow enough that there is no overlap between neighbouring sites (i.e. no hopping). Here, we can also assume the motion of the atoms to be frozen such that the motional correlation function is simplified and yields

$$C^{\mathrm{qu}}_{\alpha\beta}(\mathbf{k}) = \langle \mathrm{e}^{\mathrm{i}\mathbf{k}\cdot\mathbf{r}_{\alpha\beta}} \rangle_{\mathrm{ex}}, \tag{4.12}$$

for $\alpha \neq \beta$ and $C_{\alpha\alpha} = 1$. In the classical case, we treated the atomic position operators simply as vectors describing the exact position of the atoms, which removed the necessity of the expectation value. Now that the positions retain their operator form, we are required to find the expectation value over the external states and we will label the correlation function as "quantum". By taking this average over possible states for the external degrees of freedom, we are implying that there is some uncertainty to the atomic position and momentum. Therefore, to calculate the correlation function and, consequently, the master equation for the internal degrees of freedom, we need to determine the motional (or external) state of the atoms, ρ^{ex}. For distinguishable atoms, we write this state in its most general form as a statistical mixture of single-atom wave functions,

$$\rho^{\mathrm{ex}} = \sum_{\ell=1}^{L^N} p_\ell |\psi_\ell\rangle\langle\psi_\ell|, \tag{4.13}$$

where $\ell = (n_1, n_2, \cdots, n_N)$ denotes the index of the motional state that contains the state of each individual atom n_α, and L is the number of states that each atom can occupy. Hence, $p_\ell = \prod_{\alpha=1}^{N} p_{n_\alpha}$ is the probability of the system being in the many-body tensor product state

$$|\psi_\ell\rangle = \bigotimes_{\alpha=1}^{N} |\phi_{n_\alpha}\rangle. \tag{4.14}$$

Tracing over all atom indices $\neq \alpha, \beta$ returns the motional correlation function

$$\begin{aligned} C^{\mathrm{qu}}_{\alpha\beta}(\mathbf{k}) &= \sum_{\ell'=1}^{L^2} p_{\ell'} \langle\phi_{n_\alpha}|\mathrm{e}^{\mathrm{i}\mathbf{k}\cdot\mathbf{r}_\alpha}|\phi_{n_\alpha}\rangle\langle\phi_{n_\beta}|\mathrm{e}^{-\mathrm{i}\mathbf{k}\cdot\mathbf{r}_\beta}|\phi_{n_\beta}\rangle \\ &= \sum_{\ell'=1}^{L^2} p_{\ell'} \int_{\mathbb{R}^3} \mathrm{d}\mathbf{r}\ |\phi_{n_\alpha}(\mathbf{r})|^2 \mathrm{e}^{\mathrm{i}\mathbf{k}\cdot\mathbf{r}} \int_{\mathbb{R}^3} \mathrm{d}\mathbf{r}'\ |\phi_{n_\beta}(\mathbf{r}')|^2 \mathrm{e}^{-\mathrm{i}\mathbf{k}\cdot\mathbf{r}'}, \end{aligned} \tag{4.15}$$

where the summation is now performed over $\ell' = (n_\alpha, n_\beta)$ and $\phi_{n_\alpha}(\mathbf{r}) = \langle\mathbf{r}|\phi_{n_\alpha}\rangle$ is the external wavefunction in position space. Due to the tight confinement of the

atoms, we model each lattice site as a three-dimensional harmonic oscillator with frequencies $(\omega_x, \omega_y, \omega_z)$. Hence, each external atomic state can be factorised into three one-dimensional harmonic oscillator states

$$\phi_{n_\alpha^u}(\mathbf{r}) = \frac{\mathrm{e}^{-\frac{(u-u_\alpha)^2}{4\sigma_u^2}}}{\sqrt{2^{n_\alpha^u} n_\alpha^u! \sqrt{2\pi}\sigma_u}} H_{n_\alpha^u}\left(\frac{u-u_\alpha}{\sqrt{2}\sigma_u}\right), \tag{4.16}$$

with $u = x, y, z$. Here, $n_\alpha = (n_\alpha^x, n_\alpha^y, n_\alpha^z) \in \mathbb{N}_0^3$ are the three motional quantum numbers and $\mathbf{r}_\alpha = (x_\alpha, y_\alpha, z_\alpha)$ are the oscillator centres. $\boldsymbol{\sigma} = (\sigma_x, \sigma_y, \sigma_z)$, which has elements defined as $\sigma_u = \sqrt{\hbar/(2M\omega_u)}$ in each direction, represents the width of the oscillator and is dependent on the trapping frequency ω_u and the atomic mass M. We also define the n-th Hermite polynomial

$$H_n(\nu) = (-1)^n \mathrm{e}^{\nu^2} \frac{\mathrm{d}^n}{\mathrm{d}\nu^n}(\mathrm{e}^{-\nu^2}). \tag{4.17}$$

Neglecting the time-dependence of the motional correlation function allows us to extract it from the time integration in Eq. (4.10), such that

$$X_{\alpha\beta}(\omega_\mathrm{a}) = \sum_{\mathbf{k},\lambda} |g_{\mathbf{k}\lambda}|^2 C_{\alpha\beta}^{\mathrm{qu}}(\mathbf{k}) \left[\pi\delta(\omega_\mathbf{k} - \omega_\mathrm{a}) - \mathrm{i}\mathcal{P}\frac{1}{\omega_\mathbf{k} - \omega_\mathrm{a}}\right], \tag{4.18}$$

where $\mathcal{P}$ represents the Cauchy Principal Value. Hence, following the usual steps for the derivation, such as the one outlined in Sec. 2.3, we find a modified quantum master equation with an identical structure to Eq. (2.51) but with dissipation $\Gamma_{\alpha\beta}^\sigma$ and coherent interaction $V_{\alpha\beta}^\sigma$ coefficients modified as

$$\Gamma_{\alpha\beta}^\sigma = \frac{3\gamma}{8\pi\omega_\mathrm{a}^3} \int_0^\pi \mathrm{d}\theta \sin^3\theta \int_0^{2\pi} \mathrm{d}\phi \int_0^\infty \mathrm{d}\omega_\mathbf{k} \omega_\mathbf{k}^3 C_{\alpha\beta}^{\mathrm{qu}}(\mathbf{k}) \delta(\omega_\mathbf{k} - \omega_\mathrm{a}), \tag{4.19}$$

and

$$V_{\alpha\beta}^\sigma = -\frac{3\gamma}{16\pi^2\omega_\mathrm{a}^3} \int_0^\pi \mathrm{d}\theta \sin^3\theta \int_0^{2\pi} \mathrm{d}\phi \, \mathcal{P}\int_0^\infty \mathrm{d}\omega_\mathbf{k} \frac{\omega_\mathbf{k}^3}{\omega_\mathbf{k} - \omega_\mathrm{a}} C_{\alpha\beta}^{\mathrm{qu}}(\mathbf{k}), \tag{4.20}$$

respectively, with the components for the unit vector of the field mode being $\hat{\mathbf{k}} = (\sin\theta\cos\phi, \sin\theta\sin\phi, \cos\theta)$.

4.3.1 Low temperature: motional ground state

If the temperature of the atoms is sufficiently low, one can consider that all atoms are in the ground state of their respective traps, i.e.

$$\phi_{(0,0,0)_\alpha}(\mathbf{r}) = \prod_{u=x,y,z} \frac{\mathrm{e}^{-\frac{(u-u_\alpha)^2}{4\sigma_u^2}}}{\sqrt{\sqrt{2\pi}\sigma_u}} \tag{4.21}$$

for all $\alpha = 1, \ldots, N$. Using this external atomic state in Eq. (4.15), the motional correlation function reads

$$C^{\mathrm{qu}}_{\alpha\beta}(\mathbf{k}) = \mathrm{e}^{\mathrm{i}\mathbf{k}\cdot\mathbf{r}_{\alpha\beta}}\mathrm{e}^{-(\mathbf{k}\cdot\boldsymbol{\sigma})^2}, \tag{4.22}$$

which reduces to the classical function (4.11) in the limit $\boldsymbol{\sigma} \to (0,0,0)$, as the uncertainty of the atomic positions is reduced.

In the case of an isotropic trap, i.e. $\sigma_x = \sigma_y = \sigma_z = \sigma$, the motional correlation function simplifies to

$$C^{\mathrm{qu}}_{\alpha\beta}(\mathbf{k}) = \mathrm{e}^{\mathrm{i}\mathbf{k}\cdot\mathbf{r}_{\alpha\beta}}\mathrm{e}^{-(\omega_\mathbf{k}\sigma/c)^2} = C^{\mathrm{cl}}_{\alpha\beta}(\mathbf{k})\mathrm{e}^{-(\omega_\mathbf{k}\sigma/c)^2}. \tag{4.23}$$

The exponential factor multiplying the classical correlation function becomes independent of θ and ϕ, hence the integral over the solid angle is unaffected by the positional disorder. The resulting master equation is

$$\dot{\rho} = \sum_{\alpha,\beta=1}^{N} \Gamma^{\sigma}_{\alpha\beta}\left[\sigma^{\beta}_{-}\rho\sigma^{\alpha}_{+} - \frac{1}{2}\left\{\sigma^{\alpha}_{+}\sigma^{\beta}_{-}, \rho\right\}\right] - \mathrm{i}\sum_{\alpha\neq\beta=1}^{N} V^{\sigma}_{\alpha\beta}\left[\sigma^{\alpha}_{+}\sigma^{\beta}_{-}, \rho\right], \tag{4.24}$$

with $V^{\sigma}_{\alpha\beta} = \mathrm{e}^{-\omega_\mathrm{a}^2\sigma^2/c^2}V_{\alpha\beta}$ and $\Gamma^{\sigma}_{\alpha\beta} = \mathrm{e}^{-\omega_\mathrm{a}^2\sigma^2/c^2}\Gamma_{\alpha\beta}$ [dependent on the classical interaction and dissipation matrix elements defined in Eq. (2.53) and Eq. (2.52), respectively], unless $\alpha = \beta$ in which case $\Gamma_{\alpha\alpha} = \gamma$. Defining the matrices containing these coefficients as $\bar{V}^{\sigma}$ and $\bar{\Gamma}^{\sigma}$, it is evident that $\sigma \neq 0$ results in a reduction in the off-diagonal matrix elements for the classical interaction $\bar{V}$ and the classical dissipation $\bar{\Gamma}$ by a constant value for all pairs of atoms. To illustrate the effect of the atoms' confinement on the collective behaviour of the system, we focus from here onwards on a one-dimensional chain of atoms, which we can easily compare to the classical results outlined in Chapter 3.

Collective modified properties

We first calculate the eigenvalues of the dissipation matrix $\bar{\Gamma}^{\sigma}$ which, as we discussed before, represent the collective single-photon decay rates in the system. These are

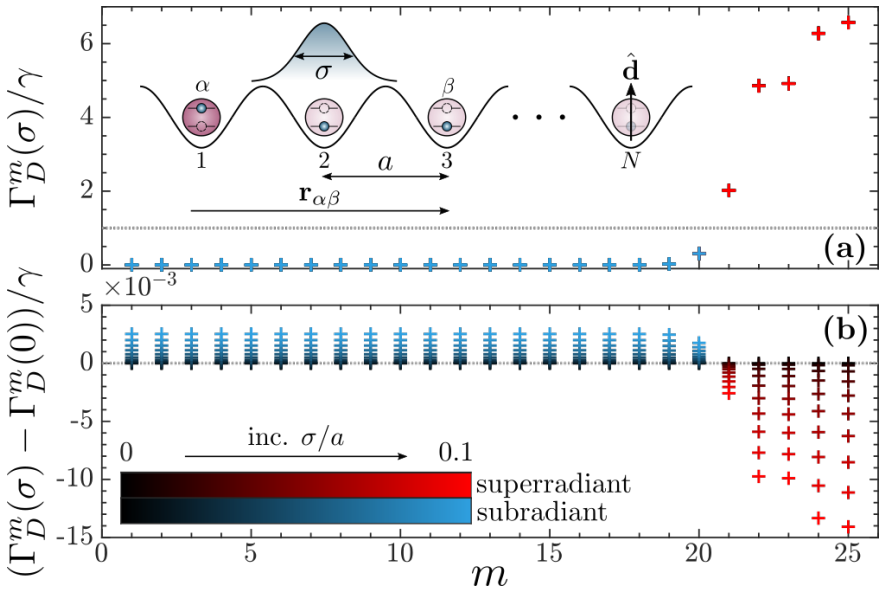

Figure 4.2: **Collective decay rates for a 1D chain. (a)** Collective decay rates $\Gamma_D^m(\sigma)$ for atomic positions determined by a Gaussian of width $\sigma = 0 \rightarrow 0.1a$ in a one-dimensional chain of $N = 25$ atoms with $a/\lambda = 0.08$. The variation is not visible in the figure due to the small differences with respect to the values for $\sigma = 0$. These differences are shown in **(b)**. The crosses ranging in colour from black to blue [subradiant rates, $\Gamma_D^m(\sigma) < \gamma$], and black to red [superradiant rates, $\Gamma_D^m(\sigma) > \gamma$] represent the increasing width of the Gaussian distribution.

presented in Fig. 4.2**(a)** for a system of $N = 25$ atoms, with interatomic spacing $a = 0.08\lambda$ and for values of the oscillator width σ between 0 and $0.1a$. In contrast to the eigenvalue analysis described in Sec. 3.4, we calculate the eigenvalues of the dissipation and interaction matrices numerically for the finite chain, such that the rates are ordered from smallest to largest (see Sec. 2.4.2). Interestingly, we find that both super- (red) and subradiant (blue) rates are almost completely unaffected by increasing σ. In order to make this change more appreciable, in Fig. 4.2**(b)** we depict the difference between the collective decay rates with respect to their values in the classical limit $\sigma \rightarrow 0$. It is here evident that increasing the uncertainty of the atomic position causes the collective decay rates to tend toward the single-atom value: the subradiant rates increase in magnitude whereas the superradiant ones decrease. However, while as one would expect that the uncertainty in atomic position reduces the collective character of the emission, it is surprisingly robust.

A similarly small effect is also observed in the energy spectrum of the system, here explored via the eigenvalues $V_D^m(\sigma)$ of the interaction matrix $\bar{V}^\sigma$, which contains the coherent dipole-dipole interactions among the atoms. These values and the differences with respect to the $\sigma \rightarrow 0$ limit are shown in Fig. 4.3**(a)** and **(b)**, respectively for a chain with the same parameters as in Fig. 4.2. In this case, an increase

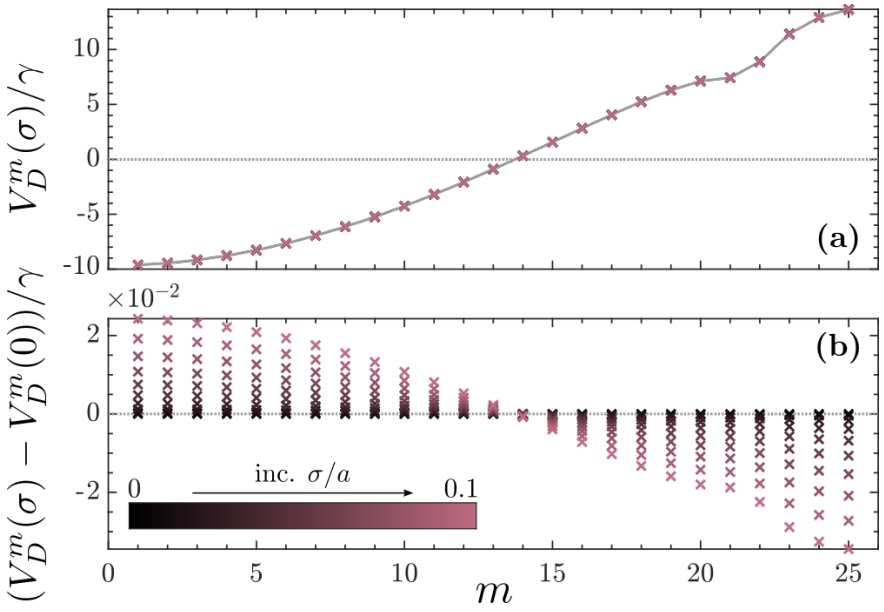

Figure 4.3: **Energy spectrum for a 1D chain. (a)** Energy spectrum $V_D^m(\sigma)$ for atomic positions determined by a Gaussian of width $\sigma = 0 \rightarrow 0.1a$, in a one-dimensional chain of $N = 25$ atoms with $a/\lambda = 0.08$. The variation is not visible in the figure due to the small differences with respect to the values for $\sigma = 0$. These differences are shown in **(b)**. The crosses ranging in colour from black to purple represent the increasing width σ.

of σ shifts all eigenvalues closer to 0: all negative values increase and all positive values decrease. This reduction in the energy eigenvalues corresponds to a decreasing interaction strength between atoms, leading to a reduced probability of an excitation hopping between sites. For example, in the case of a Gaussian wave packet prepared in the linear dispersion regime (Sec. 3.5), reduced interactions are equivalent to a smaller group velocity during transport.

Modified dynamics: excitation transport

We will now illustrate the effects described above by simulating dynamics on a lattice. The form of the master equation, for atoms trapped in lattice wells of finite width, is reminiscent of the master equation for classically fixed atoms with modified dissipation and interaction coefficients. This allows dynamics to be be calculated in the same way for both scenarios. The system is considered to be in a pure state containing a single excitation [151]. We refer to Sec. 3.2 for justification of this assumption. Hence, using these arguments the density matrix can be expressed as $\dot{\rho} = |\psi(t)\rangle\langle\psi(t)|$ where the time-dependent state is

$$|\psi(t)\rangle = \sum_{\alpha=1}^{N} c_\alpha(t)|e\rangle_\alpha. \tag{4.25}$$

Here, we recall that $|e\rangle_\alpha = |g\rangle_1 \otimes |g\rangle_2 \cdots |e\rangle_\alpha \cdots \otimes |g\rangle_N$ is shorthand for one excitation in atom α while the rest of the atoms are in their ground state. The coefficients $c_\alpha(t)$ are such that the modulus squared gives the probability of the α-th atom being populated which leads, for a single excitation, to $\sum_{\alpha=1}^{N} |c_\alpha(0)|^2 = 1$. The time dependence of these coefficients is determined by the initial state $|\psi(0)\rangle$ and the effective Hamiltonian

$$\bar{H}^\sigma_{\text{eff}} = \bar{V}^\sigma - \mathrm{i}\frac{\bar{\Gamma}^\sigma}{2}, \tag{4.26}$$

as

$$c^\sigma_\alpha(t) = \mathrm{e}^{\mathrm{i}\bar{H}^\sigma_{\text{eff}}t} c_\alpha(0). \tag{4.27}$$

Note that the effective Hamiltonian reduces to $\bar{H}_{\text{eff}} = \bar{V} - \mathrm{i}\frac{\bar{\Gamma}}{2}$ when $\sigma \to 0$. The form of this state is such that the initial state $c_\alpha(0)$ describes which lattice sites are occupied and $\bar{H}^\sigma_{\text{eff}}$ handles the implicit extension of the positional wave function in each site.

The non-hermitian nature of this effective Hamiltonian reduces the total number of excitations in the system, through dissipation. Since there is initially only one excitation, the effective Hamiltonian acts to either exchange the position of the excitation with another atom, or to emit a photon to the environment, with a probability dependent on the decay modes occupied. The probability of survival of the excitation is therefore,

$$P^\sigma_{\text{sur}}(t) = \sum_{\alpha=1}^{N} |c^\sigma_\alpha(t)|^2, \tag{4.28}$$

which is a simplified definition of Eq. (3.12) for a system of two-level atoms. In Chapter 3, we explored an initial state containing a single excitation modelled in two ways: as a single excited atom, or a Gaussian wave packet delocalised across a number of atoms. We now consider these initial states for a ring lattice geometry in Fig. 4.4**(a)** and **(b)** and a finite chain in Fig. 4.4**(c)**. These results replicate the three scenarios outlined in Chapter 3, this time considering a finite width of the trapping wells.

It is clear in all three cases (upper left panels), that introducing uncertainty in the positions of the atoms appears to have an almost negligible effect on the survival probability. We therefore provide a ratio of survival probabilities for finite σ against the classical case $\sigma \to 0$, in the lower left panels, to observe this small change. One can see that in comparison with the classical case the survival probability decreases with increasing σ. In addition to these results, the right panels demonstrate the time evolution of the atomic population for a non-zero Gaussian width. These plots are qualitatively, almost identical to the ones for atoms in fixed positions, further enforcing the minute effect that positional disorder has on the propagation and dissipation of an excitation in a 1D chain with and without periodic boundaries. This result differs significantly from the one discussed in Sec. 3.8, which suggests that positional disor-

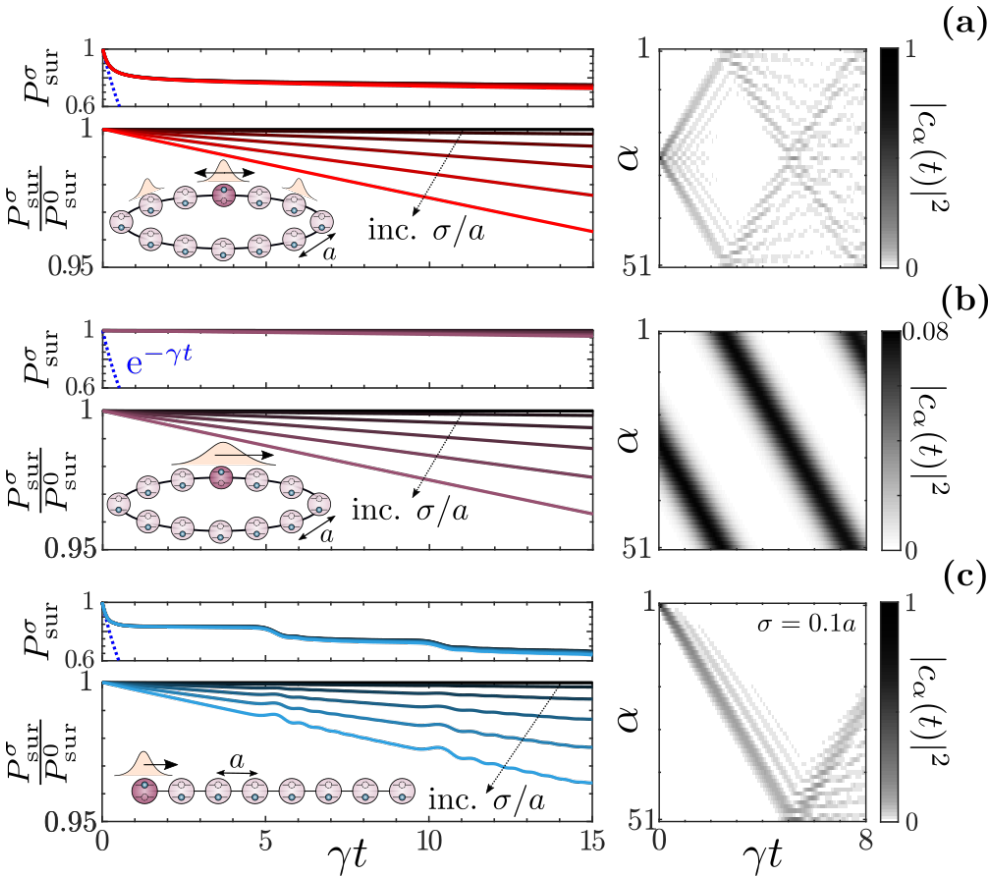

Figure 4.4: **Frozen regime disorder.** Top left is the survival probability for a single excitation initialised on a chain of $N = 51$ atoms with $a/\lambda = 0.08$ **(a)** on one site of a ring, **(b)** as an extended Gaussian wave packet on a ring and **(c)** on one site of a linear 1D chain, in comparison to the single atom decay (blue dashed). Bottom left are the ratios of survival probabilities with $\sigma = 0 \to 0.1a$ to the case with fixed atomic positions ($\sigma = 0$), and the right panels are the excitation probabilities $|c_\alpha(t)|^2$ at site α as a function of time for $\sigma = 0.1a$ which vary by an insignificant amount from $\sigma = 0$.

der of the atoms has a detrimental effect on subradiant transport. We hypothesise from this that some quantum effect may be responsible for robustness to positional disorder.

Quantitatively, one can explore how the excitation propagation has been altered by considering the case of a 1D chain with open boundaries. We conduct this investigation as an illustration of the modified interaction eigenvalues. As previously stated, the disorder appears to reduce interaction energy, which would suggest slower propagation. The results presented in Fig. 4.5 confirm this. Here the propagation time from one side of the chain to the other $t^{\sigma}_{\rm pr}$ is measured as a function of disorder σ, for various atomic spacings (red circles) and chain lengths (blue circles). In both cases [Fig. 4.5**(b)** and **(d)**], increasing the width of the wells describing the lattice sites slows the propagation of the excitation such that $t_{\rm pr}$ increases. Fig. 4.5**(a)** and **(c)** are the propagation times for the classical case as a function of interatomic spacing and

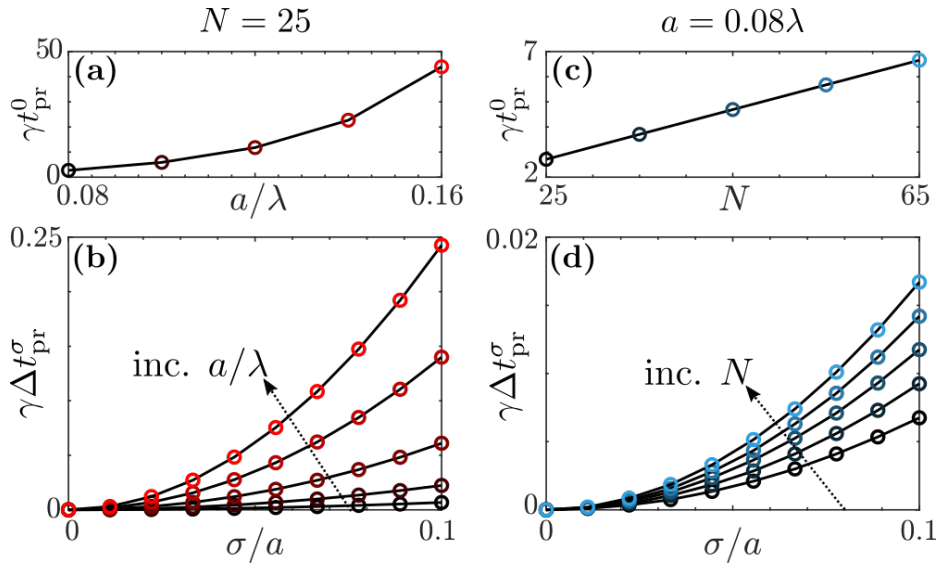

Figure 4.5: **Propagation time.** A single excitation propagates from the leftmost to rightmost atom, for width σ of the Gaussian distribution describing the position of the atoms in time $t^\sigma_{\rm pr}$. The top panels represent the propagation time for $\sigma = 0$ with **(a)** varying atomic spacing (black to red circles) with a fixed number of atoms $N = 25$ and **(c)** varying number of atoms in the chain (black to blue circles) with fixed atomic spacing $a = 0.08\lambda$. The bottom panels show the difference in propagation time from the classical case (with fixed positions) as a function of the Gaussian width σ for **(b)** increasing atomic spacing and **(d)** increasing number of atoms.

system size, respectively, as a reference point.

Our analysis so far has provided interesting results to support suppression of collective behaviour under positional disorder, while maintaining that the system is generally robust. However, by only considering the atomic positions to be described by the ground state of their corresponding 3D harmonic oscillator, we are restricted to a low temperature regime; the model only holds for temperatures that guarantee near-zero occupation of higher energy levels.

4.3.2 Extending the temperature limit: higher motional energy levels

The above case is now extended to a description that allows for higher temperatures of the lattice gas, by including higher energy levels. The 3D harmonic oscillators representing each lattice site are assumed to be identical in each direction ($\omega_u = \omega$ and $\sigma_u = \sigma$) and behave independently for each atom. Therefore, each direction is described by a 1D oscillator with an infinite number of energy levels. For a 1D oscillator (on one site), the probability of occupation for a given state n is P_n and the sum of all possible states is unity $\sum_{n=0}^{\infty} P_n = 1$, where the ratio of probabilities for

pairs of energy levels is defined using the Boltzmann distribution

$$\frac{P_n}{P_j} = \mathrm{e}^{\frac{\epsilon(j)-\epsilon(n)}{k_\mathrm{B}T}}, \tag{4.29}$$

with energy $\epsilon(n) = (n + \frac{1}{2})\hbar\omega$. These two relations allow the occupation probability of an arbitrary excited level to be expressed in terms of the ground state probability $P_0 = 1 - \exp(-\hbar\omega/k_\mathrm{B}T)$, as

$$P_n = \exp(-n\hbar\omega/k_\mathrm{B}T)P_0. \tag{4.30}$$

To calculate the correlation function, it is only necessary to evaluate energies of pairs of atoms, we therefore define the energy corresponding to the α-th atom in a given u-direction as $\epsilon(n_{\alpha,u})$, where $n_{\alpha,u}$ is the occupied energy level of that oscillator. The summation over all three directions and both atoms therefore returns

$$E_d^{\alpha\beta} = \sum_{\xi=\alpha,\beta} \sum_{u=x,y,z} \epsilon(n_{\xi,u}), \tag{4.31}$$

where $d = \sum_{\xi=\alpha,\beta} \sum_{u=x,y,z} n_{\xi,u}$ is the energy level corresponding to a particular set of oscillator states, for α and β, in all three directions. The total ground state of this system has energy $E_0^{\alpha\beta} = 6\epsilon(0) = 3\hbar\omega$ and probability $P_0^{\mathrm{tot}} = P_0^6$ of being occupied. In this definition, each excited energy level is degenerate, since it is possible for the excitations to exist in any of the six 1D oscillators. See Fig. 4.6**(a)** for example: to achieve $d = 2$, the α-th and β-th atoms could both be in the $\epsilon(1)$ state of the $\hat{x}$-oscillator, and the ground states of the $\hat{y}$- and $\hat{z}$- oscillators, such that the combined energy is

$$E_2^{\alpha\beta} = \sum_{\xi=\alpha,\beta} \sum_{u=x,y,z} \epsilon(n_{\xi,u}) = 2\epsilon(1) + 4\epsilon(0) = (2+3)\hbar\omega. \tag{4.32}$$

Alternatively, the α-th atom could be excited to the $\epsilon(2)$ energy level of the $\hat{y}$-oscillator, for example, but in the ground state of the remaining oscillators [see Fig. 4.6**(b)**]. In this case the combined energy is

$$E_2^{\alpha\beta} = \sum_{\xi=\alpha,\beta} \sum_{u=x,y,z} \epsilon(n_{\xi,u}) = \epsilon(2) + 5\epsilon(0) = (2+3)\hbar\omega. \tag{4.33}$$

We extract from these examples that the energy of the system can also be expressed as

$$E_d^{\alpha\beta} = (d+3)\hbar\omega. \tag{4.34}$$

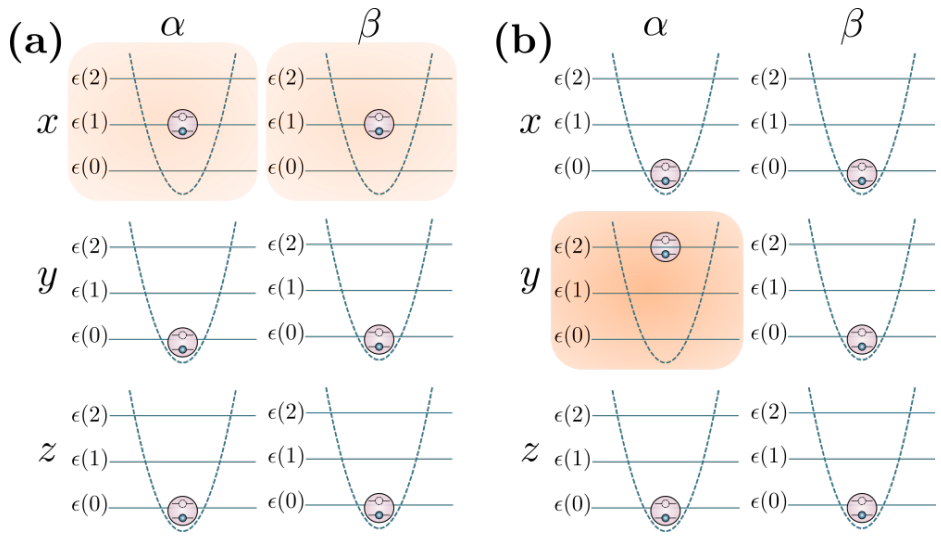

Figure 4.6: **Indistinguishable nature of the oscillator states.** The six harmonic oscillators that model the lattice sites for atoms α and β in the $\hat{x}$-, $\hat{y}$- and $\hat{z}$-directions. The total energy of the atoms occupying an excited state within these oscillators is degenerate. For example, a state with total energy $E_2^{\alpha\beta}$ can be achieved by **(a)** having both α and β in the $\epsilon(1)$ energy level of the $\hat{x}$-oscillators and in the ground states of the remaining oscillators. Alternatively, we can achieve this energy by **(b)** having only atom α in the $\epsilon(2)$ energy level of the $\hat{y}$-oscillator (and the ground states of $\hat{x}$- and $\hat{z}$-), and atom β in the ground states of all three oscillators. In total, there are 15 configurations with this energy.

In this way, the motional states of the atoms are being modelled as statistically indistinguishable, in terms of oscillator energy levels. Regardless of which ones are excited, all states with energy $E_d^{\alpha\beta}$ have the same probability of excitation

$$P(E_d^{\alpha\beta}) = \exp\left(-d\hbar\omega/k_{\mathrm{B}}T\right)P_0^6. \tag{4.35}$$

Previously, the definition of the motional correlation function for a 1D lattice in Eq. (4.15) contained a summation over all possible states of atoms α and β. The summation is now rewritten such that each term is a possible energy level of the six oscillators, and the sum of all states with that energy is incorporated into the rest of the motional correlation function,

$$C_{\alpha\beta}^{\mathrm{qu}}(\mathbf{k}) = \sum_{d=0}^{\infty} P(E_d^{\alpha\beta}) \sum_{\ell'(d)} \int_{\mathbb{R}^3} \mathrm{d}\mathbf{r}\ |\phi_{n'_\alpha}(\mathbf{r})|^2 \mathrm{e}^{\mathrm{i}\mathbf{k}\cdot\mathbf{r}} \int_{\mathbb{R}^3} \mathrm{d}\mathbf{r}'\ |\phi_{n'_\beta}(\mathbf{r}')|^2 \mathrm{e}^{-\mathrm{i}\mathbf{k}\cdot\mathbf{r}'}, \tag{4.36}$$

where $\ell'(d) = (n'_\alpha, n'_\beta)$ is the index representing states with energy $E_d^{\alpha\beta}$. The wave function for the 3D quantum harmonic oscillator [Eq. (4.16)] along with the definition of Hermite polynomials is now substituted into the motional correlation function. In

each direction (here we use $\hat{x}$ for illustration), the integral for one of the atoms is

$$\int_{-\infty}^{\infty} \mathrm{d}x \, \frac{1}{2^n n!} \frac{1}{\sqrt{2\pi}\sigma} \mathrm{e}^{-(x-x_\alpha)^2/2\sigma^2} \mathrm{e}^{\mathrm{i}k_x x} H_n\left(\frac{x-x_\alpha}{\sqrt{2}\sigma}\right)^2 = L_n(k_x^2\sigma^2)\mathrm{e}^{\mathrm{i}k_x x_\alpha}\mathrm{e}^{-\frac{k_x^2\sigma^2}{2}}, \tag{4.37}$$

which is dependent on the Laguerre polynomial, defined by

$$L_n(\nu) = \sum_{k=0}^{n} \binom{n}{k} \frac{(-1)^k}{k!} \nu^k. \tag{4.38}$$

Here, the binomial coefficient $\binom{n}{d} = \frac{n!}{d!(n-d)!}$ has been used. Taking all three directions and both atoms into account, one finds

$$C_{\alpha\beta}^{\mathrm{qu}}(\mathbf{k}) = \mathrm{e}^{\mathrm{i}\mathbf{k}\cdot\mathbf{r}_{\alpha\beta}}\mathrm{e}^{-|\mathbf{k}|^2\sigma^2} \sum_{d=0}^{\infty} \left\{ P(\epsilon_d^{\alpha\beta}) \sum_{\ell'(d)} \prod_{u=x,y,z} L_{n_u^\alpha}(k_u^2\sigma^2) L_{n_u^\beta}(k_u^2\sigma^2) \right\}. \tag{4.39}$$

By multiplying the six Laguerre polynomials, and taking the summation over all possible states with a particular energy level, it becomes evident that the solution is a polynomial in $|\mathbf{k}|^2\sigma^2$. It can be determined that the coefficients of this polynomial are related to the entries of Pascal's triangle from the fifth row, onwards (starting from the fifth column and inclusive of the remaining entries to the right). Expressing these in terms of the binomial coefficients, the motional correlation function is determined

$$C_{\alpha\beta}^{\mathrm{qu}}(\mathbf{k}) = \mathrm{e}^{\mathrm{i}\mathbf{k}\cdot\mathbf{r}_{\alpha\beta}}\mathrm{e}^{-|\mathbf{k}|^2\sigma^2} \sum_{d=0}^{\infty} \mathrm{e}^{-d\frac{\hbar\omega}{k_\mathrm{B}T}} \left(1 - \mathrm{e}^{-\frac{\hbar\omega}{k_\mathrm{B}T}}\right)^6 \sum_{n=0}^{d} \binom{5+d}{5+n} (-1)^n \frac{2^n}{n!} \left(|\mathbf{k}|^2\sigma^2\right)^n. \tag{4.40}$$

By expressing the energy level probabilities explicitly, as we have done above, we can observe which quantities the quantum motional correlation function is dependent on for the thermal states. These parameters include the trap frequency (hence trap width) the temperature of the lattice gas, the wave vector and the spacing between the atoms.

The classical motional correlation function can be factored out of Eq. (4.40)

$$C_{\alpha\beta}^{\mathrm{qu}}(|\mathbf{k}|) = C_{\alpha\beta}^{\mathrm{cl}}(|\mathbf{k}|) \sum_{d=0}^{\infty} J_d(|\mathbf{k}|), \tag{4.41}$$

such that we define the modification to the classical correlation function, for each energy level d, as

$$J_d(|\mathbf{k}|) = \mathrm{e}^{-|\mathbf{k}|^2\sigma^2}\mathrm{e}^{-d\frac{\hbar\omega}{k_\mathrm{B}T}} \left(1 - \mathrm{e}^{-\frac{\hbar\omega}{k_\mathrm{B}T}}\right)^6 \sum_{n=0}^{d} \binom{5+d}{5+n} (-1)^n \frac{2^n}{n!} \left(|\mathbf{k}|^2\sigma^2\right)^n. \tag{4.42}$$

This form of the motional correlation function is substituted into Eq. (4.18) to find the master equation. Once again, since $J_d(|\mathbf{k}|)$ is independent of θ and ϕ, the form of the master equation mirrors the classical case, and we find

$$\begin{aligned}\dot{\rho} = \sum_{d=0}^{\infty} J_d\left(\frac{\omega_{\mathrm{a}}}{c}\right)\Bigg\{ \sum_{\alpha\neq\beta=1}^{N} \Gamma_{\alpha\beta}\left[\sigma_-^{\beta}\rho\sigma_+^{\alpha} - \frac{1}{2}\left\{\sigma_+^{\alpha}\sigma_-^{\beta},\rho\right\}\right] \\ - \mathrm{i}\sum_{\alpha\neq\beta=1}^{N} V_{\alpha\beta}\left[\sigma_+^{\alpha}\sigma_-^{\beta},\rho\right]\Bigg\} + \sum_{\alpha=1}^{N}\gamma\left[\sigma_-^{\alpha}\rho\sigma_+^{\alpha} - \frac{1}{2}\left\{\sigma_+^{\alpha}\sigma_-^{\alpha},\rho\right\}\right],\end{aligned} \tag{4.43}$$

with only the assumption that each lattice site can be modelled by a 3D isotropic harmonic oscillator. This assumption may not be entirely accurate for high temperatures, since the lattice sites have a finite depth. Therefore, it is necessary to explore the temperature dependence in this equation to determine whether this is a valid assumption to make for temperatures that can be achieved experimentally.

As one would expect, in the limit $T \to 0$, the only state that remains in the motional correlation function is the ground state $(d, n = 0)$, and Eq. (4.22) is recovered. Moreover, Eq. (4.43) shows again that the quantum description, including the excited levels of the harmonic oscillators, recovers the classical master equation with only a modification to the off-diagonal terms. The modification is independent of the atomic positions or separations, and multiplies the coefficients $\Gamma_{\alpha\beta}$ and $V_{\alpha\beta}$ [Eq. (2.52) and Eq. (2.53)] by a constant value.

Now, we analyse the effect that multiplying these coefficients by $\sum_{d=0}^{\infty} J_d\left(\frac{\omega_{\mathrm{a}}}{c}\right)$ has on the cooperativity in the system. In Fig. 4.7**(a)**, the modification to the motional correlation function is analysed for varying temperatures, at different truncations of the energy levels n_{tr} required to describe the correlations. We do this for the exploration of the D2 transition in rubidium-87 atoms, trapped in lattice sites with $\sigma = 0.1a$. This quantity is decomposed further into the contributions due to each energy level (up to $n_{\mathrm{tr}} = 20$ in this case) in Fig. 4.7**(b)**. It is evident that the modification is always a value less that 1, such that the off-diagonal elements of $\Gamma_{\alpha\beta}$ and $V_{\alpha\beta}$ are always reduced if the temperature or well width is increased. Therefore, the effect of the modification resembles the results in Fig. 4.2, Fig. 4.3 and Fig. 4.4, for increasing temperature and well width. This is intuitive for low temperatures, since the ground state is mostly populated and the higher energy level occupations are negligible.

Furthermore, at low temperature, the modification to the correlation function maps onto a single curve, which emphasises the importance of higher energy levels as the temperature increases. This result is reiterated in Fig. 4.7**(b)** where the higher energy contributions evidently become more significant above the temperature bound (vertical dotted lines) given for the particular truncation. For example, consider modelling a lattice with well widths $\sigma = 0.1a$. In order to accurately represent the motional

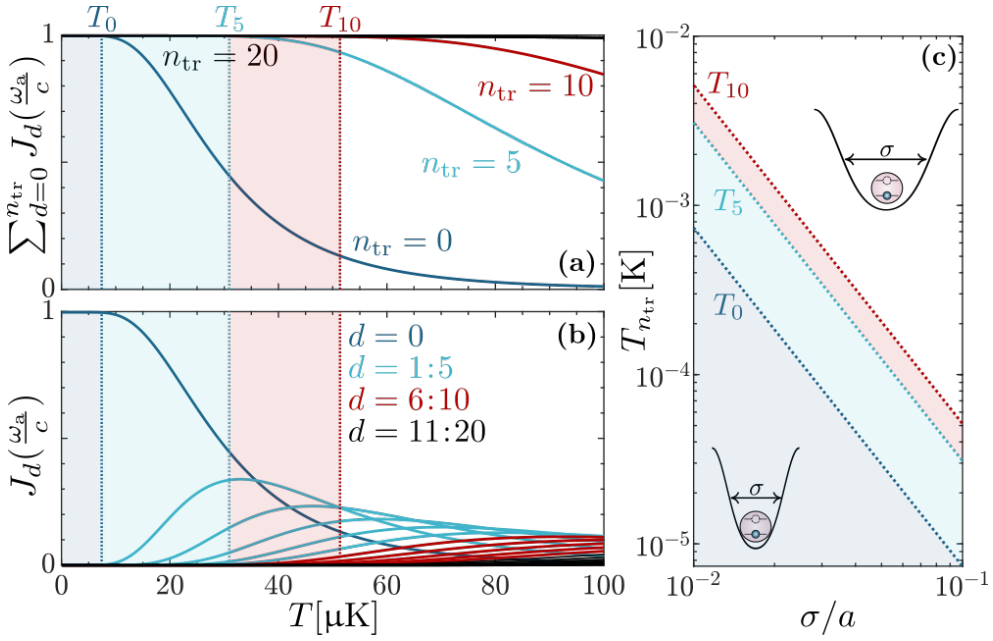

Figure 4.7: **Temperature limits. (a)** The modification to the classical motional correlation function $\sum_{d=0}^{n_{\rm tr}} J_d(\frac{\omega_a}{c})$, due to the quantum description of the lattice sites as 3D quantum harmonic oscillators with trap width $\sigma = 0.1a$, where $a = 0.08\lambda$. The expression is truncated to only include $n_{\rm tr} = 0$ (dark blue), $n_{\rm tr} = 5$ (light blue), $n_{\rm tr} = 10$ (red), and $n_{\rm tr} = 20$ (black) energy levels. The shaded regions define the temperature regime (with the upper bound $T_{n_{\rm tr}}$) in which the truncation is valid, given that the modification deviates by less than 0.01 from the more complete modification (in this case $n_{\rm tr} = 20$). **(b)** Decomposition of the modification into individual contributions $J_d(\frac{\omega_a}{c})$ from each energy level. The colour of the lines highlights which truncation the levels are contributing to. **(c)** Upper temperature bounds for the three explored truncations as a function of the width of the lattice site.

correlation function using only the ground state of the atomic positions, the lattice must be cooler than $T \approx 7\mu$K. This temperature bound is of the same order of magnitude as temperatures experimentally achieved in MOTs and optical lattices [152–154], suggesting that this may be an appropriate approximation to make in some scenarios. Alternatively, it is straightforward to truncate at a higher number of energy levels when simulating the dynamics numerically, which allows for the exploration of higher temperatures.

In addition to this, from both Eq. (4.42) and the Fig. 4.7**(c)**, it is clear that higher temperatures can be achieved for truncations at lower values of d when the width of the lattice sites is smaller. Higher energy levels of the oscillator states, for atoms that are tightly confined, provide smaller contributions to the modification. Therefore, we are able to model positional disorder by the oscillator ground states for higher temperatures when the lattice width is smaller.

Of course, one must also be aware that the choice of Gaussian width ultimately

determines a trapping frequency. To achieve a narrow trap width that allows for ground state modelling at higher temperatures, we require a very high laser frequency. We may be forced to use higher energy levels in our model for experimentally achievable laser trapping frequencies.

4.4 Indistinguishable atoms

In the case of a 1D lattice, the atoms can be modelled as distinguishable, since their positions are always known. The possibility of hopping across lattice sites is neglected. However, this may not be the case in scenarios such as when the lattice sites in an array have significant overlap due to the non-zero Gaussian width, or when the dynamics are being modelled for many atoms in one trap.

For indistinguishable atoms, the state of the atomic positions must be defined such that it is symmetric $(+)$ or antisymmetric $(-)$ under the exchange of atoms depending on whether the atoms are modelled as bosons or fermions. This is determined by the sum of the protons, neutrons and electrons that constitute the atom. Each of these particles has spin$-\frac{1}{2}$, so an atom with an odd number in total is considered fermionic, while atoms with an even number are bosonic [82]. We achieve this symmetry/antisymmetry by defining the state as a superposition of all of the possible ways in which the atoms can contain a certain number of positional excitations

$$|\Phi^{\mathrm{ex},\pm}\rangle = \sqrt{\frac{n_{\phi_1}!\cdots n_{\phi_L}!}{N!}} \sum_{\pi} s_{\pm}^{\pi} |\phi_{\pi(1)}\cdots\phi_{\pi(N)}\rangle, \tag{4.44}$$

where there are N atoms which can exist in L different states, π is the set of unique permutations and $|\phi_j\rangle$ is the single atom motional state. Whether this equation models bosons (+) or fermions (-) is encoded in

$$s_{\pm}^{\pi} = \begin{cases} 1 & \text{if } +, \\ \mathrm{sign}(\pi) & \text{if } -\,. \end{cases} \tag{4.45}$$

Taking this state to be pure, the density matrix is $\rho^{\mathrm{ex},\pm} = |\Phi^{\mathrm{ex},\pm}\rangle\langle\Phi^{\mathrm{ex},\pm}|$ and tracing over the indices $\neq \alpha, \beta$, to extract the relevant information for the motional correlation function $C^{\mathrm{qu}}_{\alpha\beta}(\mathbf{k})$, gives

$$\begin{aligned} \rho^{\mathrm{ex},\pm}_{\alpha\beta} = \frac{n_{\phi_1}!\cdots n_{\phi_L}!}{N!} \sum_{\pi,\pi'} s_{\pm}^{\pi} s_{\pm}^{\pi'} \prod_{\xi\neq\alpha,\beta}^{N} \langle\phi_{\pi'(\xi)}|\phi_{\pi(\xi)}\rangle \\ \times |\phi_{\pi(\alpha)}\phi_{\pi(\beta)}\rangle\langle\phi_{\pi'(\alpha)}\phi_{\pi'(\beta)}|. \end{aligned} \tag{4.46}$$

Recall now the motional correlation function is defined as $C^{\rm qu}_{\alpha\beta}(\mathbf{k}) = \langle \mathrm{e}^{\mathrm{i}\mathbf{k}\cdot\mathbf{r}_{\alpha\beta}}\rangle_{\rm ex}$ in the frozen regime, where all motional correlations decay faster than the timescales associated with the system dynamics. Therefore this quantity is calculated by taking the expectation value over the motional states:

$$\begin{aligned} C^{\rm qu}_{\alpha\beta}(\mathbf{k}) &= \frac{n_{\phi_1}!\cdots n_{\phi_L}!}{N!}\sum_{\pi,\pi'} s^{\pi}_{\pm}s^{\pi'}_{\pm}\prod_{\xi\neq\alpha,\beta}^{N}\langle\phi_{\pi'(\xi)}|\phi_{\pi(\xi)}\rangle \\ &\qquad\times\langle\phi_{\pi'(\alpha)}|\mathrm{e}^{\mathrm{i}\mathbf{k}\cdot\mathbf{r}_\alpha}|\phi_{\pi(\alpha)}\rangle\langle\phi_{\pi'(\beta)}|\mathrm{e}^{-\mathrm{i}\mathbf{k}\cdot\mathbf{r}_\beta}|\phi_{\pi(\beta)}\rangle \\ &= \frac{n_{\phi_1}!\cdots n_{\phi_L}!}{N!}\sum_{\pi,\pi'} s^{\pi}_{\pm}s^{\pi'}_{\pm}F_\alpha(\mathbf{k})F_\beta(-\mathbf{k})\prod_{\xi\neq\alpha,\beta}^{N}F_\xi(\mathbf{0}), \end{aligned} \tag{4.47}$$

where $F_\alpha(\mathbf{k}) = \int_{\mathbb{R}^3}\mathrm{d}\mathbf{r}\ \phi^*_{\pi'(\alpha)}(\mathbf{r})\phi_{\pi(\alpha)}(\mathbf{r})\,\mathrm{e}^{\mathrm{i}\mathbf{k}\cdot\mathbf{r}}$. In the very low temperature regime, while the atoms are considered as trapped in a harmonic oscillator, all atoms can occupy the ground state. If each atom is modelled by a Gaussian state [Eq. (4.21)], with its own centre $\mathbf{r}_{\pi(\alpha)}$, and an assumption is also made that the traps are identical and symmetric in all three directions ($\omega_u = \omega$ and $\sigma_u = \sigma$), one calculates

$$F_\alpha(\mathbf{k}) = \mathrm{e}^{\mathrm{i}\mathbf{k}\cdot[\mathbf{r}_{\pi'(\alpha)}+\mathbf{r}_{\pi(\alpha)}]/2}\mathrm{e}^{-\mathbf{r}^2_{\pi'(\alpha)\pi(\alpha)}/8\sigma^2}\mathrm{e}^{-|\mathbf{k}|^2\sigma^2/2}, \tag{4.48}$$

with $\mathbf{r}_{\pi'(\alpha)\pi(\alpha)} = \mathbf{r}_{\pi'(\alpha)} - \mathbf{r}_{\pi(\alpha)}$. Substituting this equation into the motional correlation function for α, β and n, one finds

$$C_{\alpha\beta}(\mathbf{k}) = \frac{n_{\phi_1}!\cdots n_{\phi_L}!}{N!}\mathrm{e}^{-|\mathbf{k}|^2\sigma^2}\sum_{\pi,\pi'} s^{\pi}_{\pm}s^{\pi'}_{\pm}\mathrm{e}^{\mathrm{i}\mathbf{k}\cdot\mathbf{r}^{\pi\pi'}_{\alpha\beta}}\prod_{\xi=1}^{N}\mathrm{e}^{-[\mathbf{r}_{\pi'(\xi)}-\mathbf{r}_{\pi(\xi)}]^2/(8\sigma^2)}, \tag{4.49}$$

where $\mathbf{r}^{\pi\pi'}_{\alpha\beta} = [\mathbf{r}_{\pi'(\alpha)\pi(\beta)} + \mathbf{r}_{\pi(\alpha)\pi'(\beta)}]/2$. In this motional correlation function, the only factors that have a dependence on $\mathbf{k}$ are the exponential decay factor $\mathrm{e}^{-|\mathbf{k}|^2\sigma^2}$ and the phase factor $\mathrm{e}^{\mathrm{i}\mathbf{k}\cdot\mathbf{r}^{\pi\pi'}_{\alpha\beta}}$. Moreover, the decay factor is independent of the angular part of $\mathbf{k}$. Therefore, only the phase factor of the correlation function must be integrated over the solid angle, which is of the exact same form as Eq. (2.41). Hence, the master equation for the indistinguishable, frozen case is

$$\begin{aligned} \dot\rho =& \frac{n_{\phi_1}!\cdots n_{\phi_L}!}{N!}\sum_{\pi,\pi'}\Bigg[\sum_{\alpha\neq\beta}^{N}\Bigg\{\frac{3\gamma}{2}f(\omega_{\rm a},\mathbf{r}^{\pi\pi'}_{\alpha\beta})\left[\sigma^\beta_-\rho\sigma^\alpha_+ - \frac{1}{2}\left\{\sigma^\alpha_+\sigma^\beta_-,\rho\right\}\right] \\ &+\mathrm{i}\frac{3\gamma}{4}g(\omega_{\rm a},\mathbf{r}^{\pi\pi'}_{\alpha\beta})\left[\sigma^\alpha_+\sigma^\beta_-,\rho\right]\Bigg\}s^{\pi}_{\pm}s^{\pi'}_{\pm}\prod_{\xi=1}^{N}\mathrm{e}^{-[\mathbf{r}_{\pi'(\xi)}-\mathbf{r}_{\pi(\xi)}]^2/(8\sigma^2)}\Bigg]\mathrm{e}^{-\frac{\omega_{\rm a}^2\sigma^2}{c^2}} \\ &+\sum_{\alpha=1}^{N}\gamma\left[\sigma^\alpha_-\rho\sigma^\alpha_+ - \frac{1}{2}\left\{\sigma^\alpha_+\sigma^\alpha_-,\rho\right\}\right]. \end{aligned} \tag{4.50}$$

where $f(\omega_{\rm a}, \mathbf{r}_{\alpha\beta}^{\pi\pi'})$ and $g(\omega_{\rm a}, \mathbf{r}_{\alpha\beta}^{\pi\pi'})$ have the same form as Eq. (2.45) and Eq. (2.50), respectively. It is worth noting here that we are referring to the atomic positions as indistinguishable, whereas in the previous section, the indistinguishability referred to the energy of the atoms within the harmonic oscillators.

4.4.1 3D atomic gas

Consider now an atomic gas trapped in a MOT with temperatures low enough that motional correlations are frozen in time. All atoms now have the same centre $\mathbf{r}_{\pi(\alpha)} = 0$, and every atom occupies the same motional state; the Gaussian state which represents the ground state of the harmonic oscillator is

$$\phi_1(\mathbf{r}) = \prod_{u=x,y,z} \sqrt{\frac{1}{\sqrt{2\pi}\sigma}} \mathrm{e}^{-u^2/4\sigma_u^2}, \tag{4.51}$$

therefore $n_{\phi_1} = N$ and $n_{\phi_2}, \ldots, n_{\phi_L} = 0$. This is only possible for atoms modelled as bosons, which corresponds to the symmetric case. This instance only has one unique permutation, which simplifies the case further, as $\pi = \pi'$ and the summation over these indices vanishes. Using that $f(\omega_{\rm a}, \mathbf{0}) \to 2/3$ and $g(\omega_{\rm a}, \mathbf{0}) \to 0$, the master equation becomes

$$\dot{\rho} = \sum_{\alpha=1}^{N} \gamma \left[\sigma_-^\alpha \rho \sigma_+^\alpha - \frac{1}{2} \left\{ \sigma_+^\alpha \sigma_-^\alpha, \rho \right\} \right] + \sum_{\alpha \neq \beta = 1}^{N} \gamma \left[\sigma_-^\beta \rho \sigma_+^\alpha - \frac{1}{2} \left\{ \sigma_+^\alpha \sigma_-^\beta, \rho \right\} \right] \mathrm{e}^{-\frac{\omega_{\rm a}^2 \sigma^2}{c^2}}. \tag{4.52}$$

From this, one observes that there is no longer a coherent evolution term, which arises since this situation models a BEC. All atoms occupy the same state, and the collection is described by a single wavefunction. The dependence on the atomic index is also removed from this case, due to the indistinguishable nature of the atoms. Hence, all off-diagonal elements take the same value: the single atom decay rate multiplied by a modifying factor ≤ 1. When $\sigma \to 0$, the modification tends to 1, and the matrix of dissipative coefficients becomes uniform. This case corresponds to the most collective one, since $N-1$ collective decay rates are maximally subradiant, $\Gamma_D^k = 0$, and the remaining rate is the most superradiant one $\Gamma_D^k = N\gamma$. Intuitively, this result is expected, since the trap only exists at a single point, and all atoms would occupy the same space. For non-zero values of σ, the off-diagonal elements decrease away from γ, which suggests that the collective nature of the cloud is also reduced.

The case of a cloud of atoms within a 3D harmonic trap is now extended to higher temperatures, such that one must account for atoms occupying higher energy levels of the trap than the ground state. The assumption that the motional states are approximately frozen with respect to system relaxation timescales still holds for the

temperatures being explored in this section, therefore the frozen regime is maintained.

For higher temperatures, it is assumed that a collection of atoms trapped within a 1D harmonic potential (in a general direction, u) occupies a thermal state, which is represented by the density matrix

$$\rho_u^{\text{ex}} = \sum_{n_u=0}^{\infty} \frac{\bar{n}_u^{n_u}}{(1+\bar{n}_u)^{1+n_u}} |\phi_{(n_u,\mathbf{0})}\rangle\langle\phi_{(n_u,\mathbf{0})}|, \tag{4.53}$$

where $\bar{n}_u = 1/\left(\mathrm{e}^{\hbar\omega_u/k_{\text{B}}T} - 1\right)$ is the average number of phonons present at temperature T. Generalisation of this density matrix to 3D is achieved simply, since the $\hat{x}$-, $\hat{y}$- and $\hat{z}$-directions are decoupled from one another, and the full density matrix is constructed by $\rho^{\text{ex}} = \rho_x^{\text{ex}} \otimes \rho_y^{\text{ex}} \otimes \rho_z^{\text{ex}}$. For the isotropic geometry, the average number of phonons is equivalent in all three directions $\bar{n}_u = \bar{n} = 1/\left(\mathrm{e}^{\hbar\omega/k_{\text{B}}T} - 1\right)$, and the full density matrix is

$$\rho^{\text{ex}} = \sum_{\substack{n_x,n_y,\\ n_z=0}}^{\infty} \frac{\bar{n}^{n_x+n_y+n_z}}{(1+\bar{n})^{3+n_x+n_y+n_z}} |\phi_{(n_x,n_y,n_z)}(\mathbf{0})\rangle\langle\phi_{(n_x,n_y,n_z)}(\mathbf{0})|, \tag{4.54}$$

where the state can be relabelled as $|\phi_{(n_x,n_y,n_z)}(\mathbf{0})\rangle = |n_x\rangle|n_y\rangle|n_z\rangle$ and is separable for all three directions. Once again, using the definition of the motional correlation function in the frozen regime $C_{\alpha\beta}(\mathbf{k}) = \langle \mathrm{e}^{\mathrm{i}\mathbf{k}\cdot\mathbf{r}_\alpha}\mathrm{e}^{-\mathrm{i}\mathbf{k}\cdot\mathbf{r}_\beta}\rangle$, along with Eq. (4.54), one finds

$$C_{\alpha\beta}(\mathbf{k}) = \prod_{u=x,y,z} \sum_{n_u=0}^{\infty} \frac{\bar{n}^{n_u}}{(1+\bar{n})^{1+n_u}} \langle n_u|\mathrm{e}^{\mathrm{i}k_u u_\alpha}|n_u\rangle\langle n_u|\mathrm{e}^{-\mathrm{i}k_u u_\beta}|n_u\rangle. \tag{4.55}$$

By writing the position operators in terms of creation and annihilation operators for the phonons in that direction, $u_\alpha = \sigma\left(a_u + a_u^\dagger\right)$, and using the Baker-Campbell Hausdorff theroem, the expectation values become

$$\langle n_u|\mathrm{e}^{\pm\mathrm{i}k_u\sigma\left(a_u+a_u^\dagger\right)}|n_u\rangle = \langle n_u|\mathrm{e}^{\pm\mathrm{i}k_u\sigma a_u^\dagger}\mathrm{e}^{\pm\mathrm{i}k_u\sigma a_u}\mathrm{e}^{-k_u^2\sigma^2\left[a_u,a_u^\dagger\right]/2}|n_u\rangle. \tag{4.56}$$

The commutation relation $\left[a_u, a_u^\dagger\right] = 1$ allows the decay factor to be removed from the expectation value, and by Taylor expanding the remaining two phase factors, one finds

$$\langle n_u|\mathrm{e}^{\pm\mathrm{i}k_u\sigma\left(a_u+a_u^\dagger\right)}|n_u\rangle = \sum_{\ell,m=0} \frac{(\pm\mathrm{i}k_u\sigma)^\ell}{\ell!}\frac{(\pm\mathrm{i}k_u\sigma)^m}{m!}\langle n_u|a_u^{\dagger\ell}{a_u}^m|n_u\rangle\mathrm{e}^{-k_u^2\sigma^2/2}, \tag{4.57}$$

where $\langle n_u|a_u^{\dagger\ell}{a_u}^m|n_u\rangle = \delta_{\ell m}\ell!\bar{n}_u^{\ell}$ [83]. Effectuating the Kronecker delta removes the second summation in Eq. (4.57), and the form of the equation again resembles a

Taylor expansion of $\mathrm{e}^{-k_u^2\sigma^2\bar{n}}$, such that $\langle n_u|\mathrm{e}^{\pm \mathrm{i}k_u u_\alpha}|n_u\rangle = \mathrm{e}^{-k_u^2\sigma^2(2\bar{n}+1)}$. The motional correlation function is therefore

$$C_{\alpha\beta}(\mathbf{k}) = \sum_{\substack{n_x,n_y,\\ n_z=0}}^{\infty} \frac{\bar{n}^{n_x+n_y+n_z}}{(1+\bar{n})^{3+n_x+n_y+n_z}} \mathrm{e}^{-|\mathbf{k}|^2\sigma^2(2\bar{n}+1)}. \tag{4.58}$$

The three summations can now be contained in a single summation over one index n by noting that there are $\binom{n+2}{n}$ combinations of n_x, n_y and n_z that give the same value for $n = n_x + n_y + n_z$. Hence, the motional correlation function for a many-body atomic ensemble, trapped in a 3D harmonic potential in a thermal state, is

$$C_{\alpha\beta}(\mathbf{k}) = \sum_{n=0}^{\infty} \frac{\bar{n}^n}{(1+\bar{n})^{3+n}} \binom{n+2}{n} \mathrm{e}^{-|\mathbf{k}|^2\sigma^2(2\bar{n}+1)}. \tag{4.59}$$

This summation has the exact solution

$$\sum_{n=0}^{\infty} \frac{\bar{n}^n}{(1+\bar{n})^{3+n}} \binom{n+2}{n} = 1, \tag{4.60}$$

and the motional correlation function for the atomic gas trapped in a spherical 3D trap is

$$C_{\alpha\beta}(|\mathbf{k}|) = C(|\mathbf{k}|) = \mathrm{e}^{-|\mathbf{k}|^2\sigma^2(2\bar{n}+1)}. \tag{4.61}$$

This expression highlights one of the key differences between the correlation functions for the distinguishable atoms and indistingiushable atoms case, since it does not contain the term dependent on the separation between pairs of atoms. With all indistinguishable atoms in the same trap, it is impossible to determine the positions of any one atom. All possibilities of each atom existing in a particular position with respect to the remainder of the ensemble are already accounted for. On the other hand, a similarity between the two cases is the dependence on the exponential decay factor $\mathrm{e}^{-|\mathbf{k}|^2\sigma^2}$, and confirms that the correlations are reduced with a greater uncertainty in the position of the atoms (a larger cloud).

The master equation can now be determined for an atomic gas in a 3D spherical cloud, by recalling Eq. (4.8), and substituting the motional correlation function [Eq. (4.61)] into Eq. (4.18). One must note that $C_{\alpha\beta}(\mathbf{k}) = 1$ when $\alpha = \beta$ and for this

scenario, $C_{\alpha\beta}(\mathbf{k}) = C(|\mathbf{k}|)$ for $\alpha \neq \beta$. The master equation is therefore

$$\begin{aligned}\dot{\rho} = \sum_{\alpha\neq\beta=1}^{N} \Bigg\{ & \gamma \left[\sigma_-^\beta \rho \sigma_+^\alpha - \frac{1}{2} \left\{ \sigma_+^\alpha \sigma_-^\beta, \rho \right\} \right] \mathrm{e}^{-\frac{\omega_\mathrm{a}^2 \sigma^2}{c^2}(2\bar{n}+1)} \\ & + \frac{\mathrm{i}\gamma}{2\pi\omega_\mathrm{a}^3} \mathcal{P} \int_{-\infty}^{\infty} \mathrm{d}\omega_\mathbf{k}\, \mathrm{e}^{-\frac{\omega_\mathbf{k}^2 \sigma^2}{c^2}(2\bar{n}+1)} \frac{\omega_\mathbf{k}^3}{\omega_\mathbf{k} - \omega_\mathrm{a}} \left[\sigma_+^\alpha \sigma_-^\beta, \rho \right] \Bigg\} \\ & + \sum_{\alpha=1}^{N} \gamma \left[\sigma_-^\alpha \rho \sigma_+^\alpha - \frac{1}{2} \left\{ \sigma_+^\alpha \sigma_-^\alpha, \rho \right\} \right].\end{aligned} \tag{4.62}$$

From this result, we observe a greater reduction in the off-diagonal elements of the dissipation matrix for higher temperatures (implied by a larger $\bar{n}$), hence we find that increasing temperature once again acts to diminish collectivity. In the opposite limit when $T \to 0$, we recover our master equation for a BEC Eq. (4.52) as $\bar{n} \to 0$ and all atoms occupy the ground state.

These calculations are part of an ongoing investigation into the role of thermal motion on collectivity within atomic ensembles. To proceed with this project, we will extend our calculations to considerations outside of the frozen regime. In this case, one might be required to simulate the dynamics in order to observe the impact on collectivity. This contrasts with the results presented in this chapter, where we were mostly able to predict the consequence of disorder on collective behaviour from the master equation itself.

4.5 Conclusions and outlook

In this chapter, we have explored the significance of atomic motion on the robustness of collective phenomena in many-body atomic ensembles, by introducing the external atomic degrees of freedom as a part of the bath. We derived the master equation under the same assumptions as Chapter 2 and extracted a motional correlation function that accounts for these external degrees of freedom.

We began our analysis by modelling atoms within an optical lattice. Taking the lattice wells to be sufficiently deep, we could describe the wells as quantum harmonic oscillators. We assumed that hopping between sites was prohibited such that the atoms could be described as distinguishable. By firstly considering the zero temperature regime, we assumed that all atoms occupied the oscillator ground states. We determined the corresponding motional correlation function for this case, where the atomic motion is frozen however an uncertainty in the atomic positions still existed due to the non-zero width of the well. We explored the robustness of collectivity and subradiance protected transport, introduced in Chapter 3, to this intrinsic positional disorder and we found that in this temperature limit subradiance is indeed robust; more-so than

the classical positional disorder modelled in Sec. 3.8 for the same parameter regime.

We proceeded to test the validity of the frozen temperature regime by introducing higher energy oscillator states into the model and exploring the individual state occupations as a function of temperature. This analysis allowed us to identify appropriate temperature limits for a given truncation of oscillator states which depends also on the width of the lattice sites. We concluded that for temperatures on the order of micro-Kelvins, one could still accurately model the motional states purely in the oscillator ground states even for the larger values of disorder that we inspected. We should note, however, that this is a preliminary investigation into possible achievable temperatures in experiments. Further investigations should be made into the lasers used to trap the atoms, as this would inform us of other parameters to be used such as the depth of the lattice sites. It would also allow us to explore where the approximation of lattice sites as harmonic oscillators breaks down.

In a related investigation, we considered the atoms to be indistinguishable. This is necessary for atoms trapped in a lattice with overlapping well widths, such that hopping between sites is possible, and for clouds of atoms trapped in 3D MOTs. We determined the appropriate motional correlation functions in these cases, along with the corresponding master equations, again in the frozen regime. This temperature regime was extended for the 3D cloud of atoms, to account for thermal effects, which has direct relevance to ongoing experimental research [28]. This remains an open investigation, where one can now utilise the master equation in order to probe the dynamics of such atomic ensembles for given temperatures. An interesting question to ask is how the motion of atoms at the thermal (experimental) temperatures affects collective behaviour. Do we still observe robust subradiant phenomena? What roles do Doppler broadening and recoil play with regards to collective behaviour? These questions will be examined following this investigation.

Chapter 5
Collectivity in a laser driven 1D chain

5.1 Introduction

In Chapter 3, we investigated collective behaviour that arises in one-dimensional atomic arrays with a single excitation that exists on one, or spread over a few, lattice sites. The results that we have produced stem entirely from theoretical explorations by means of analytic derivations obtained and numerical simulations. Analogous systems are also of interest experimentally due to continued advances in atom-array trapping techniques, for instance using optical lattices [33, 126, 152, 153, 155–158] and optical tweezers [40, 139, 142]. However there still remains a gap between the regimes that one can model theoretically and those that are experimentally achievable. For instance, Reference [14] demonstrates that there exists a magic wavelength that could allow for the trapping of strontium atoms with interatomic spacing much smaller than the transition wavelength, however realising such close spacing experimentally still proves to be a challenge.

Close interatomic spacing is not the only experimental challenge that prohibits us from demonstrating our theoretical findings in a real setting. The state preparation is also an important consideration to make. We previously considered initial states that require single atom resolution laser driving, whereas in reality the width of the laser beam may extend over the lengthscale of many atoms. Additionally, preparation of Gaussian wave packets creates issues due to the necessity of some particular phase imprinting protocol that could be difficult to implement experimentally.

Moreoever, while the ability to create atom-array systems using optical lattices and optical tweezers provides a platform for exploring many-body quantum systems in uniformly spaced geometries, there exist experimental challenges when attempting to prepare a lattice trapping atoms with uniform, singly occupied sites. Some techniques allow uniform trapping across the lattice, however this usually produces a situation in which the lattice is filled with many atoms per site [159]. Ideally we require singly occupied sites with unit filling ($\eta = 1$ where η is the filling fraction) which does not exceed > 1 atom per site, to fully match our theoretically modelled scenario. While challenging, this is not impossible, and defect-free, singly occupied lattices have been achieved [140, 141]. For example, one can create a randomly loaded array

of Rydberg atoms with $\eta = 0.5$ which is then reordered using optical tweezers [160]. Alternatively, there are known reports of atomic arrays containing no more than a single atom per lattice site, however this usually is accompanied by the appearance of defects leading to an imperfect filling fraction $\eta < 1$ [161].

In this chapter, we address these experimental challenges and conduct investigations to explore to what extent collective behaviour can be observed in a realistic scenario. We begin in Sec. 5.2 by defining a set of relevant experimental parameters for optical lattices that allow us to compare the theoretical case previously modelled to a physical situation. We proceed to consider a simple model of laser driving that does not require single or few atom resolution; we take the case where the entire chain is illuminated by the laser field. This model of laser driving has been exploited by a number of theoretical research groups to describe the preparation of an excited atomic system and examine the collective features exhibited [15, 16, 91]. We depict, here, the different directions of driving that we are able to study, with a laser field that varies over the length of the chain.

By incorporating spatially dependent laser driving from Sec. 2.5 into our many-body system master equation, we introduce the steady state properties in Sec. 5.3 that describe the statistics of the system in the infinite time limit. We assume a weakly driven 1D chain, to ensure that we remain within the single (or zero) excitation sector, allowing us to define an equation for the photon emission rate. From this result, we can make a more detailed analysis on the effect of interatomic spacing on the collective behaviour that can arise. Results of this investigation are presented in Sec. 5.4 for different orientations of the driving photon momentum. We make a detailed comparison between the photon emission rate and the decay rates determined from the corresponding master equation. We find a direct mapping from the collective decay rates to the widths of the photon emission spectra.

Finally, in Sec. 5.5, we investigate the effect of imperfect filling on the collective nature of the weakly driven chain, by calculating again the photon emission rate. We consider these imperfections as another form of disorder, and incorporate them into our model to explore the robustness of collectivity in an experimentally realisable regime. Results from the investigations presented in this chapter may bridge the gap between the theoretical understanding and the experimental potential to observe collective behaviour in regular atomic-array geometries.

5.2 Experimental parameters

We have knowingly taken optimal regimes in previous chapters, to clearly demonstrate collective behaviour, however we now want to investigate a readily realisable case; we

will explore the steady state behaviour for the parameters defined below. Following investigations of the parameter space, we aim to evaluate the likelihood of observing collectivity in this specific experimental regime. Here, we define a set of parameters taken directly from an experimental set-up in the Quantum Optics - Atoms group at Institut d'Optique in Palaiseau [162, 163].

Spacing

The optical lattice that we aim to model has a wavelength $\lambda_{\mathrm{OL}} = 940\mathrm{nm}$, such that the interatomic spacing is $a = 470\mathrm{nm}$. The trap will be assumed to be filled with rubidium-87 atoms and we will probe the D2 transition such that the atomic transition wavelength is $\lambda = 780\mathrm{nm}$ and the single atom decay rate is $\gamma = 2\pi \times 6.07$ MHz [28]. The interatomic spacing in this case can be as large as $a/\lambda = 0.6$.

Filling fraction

We assume filling of one atom per site, however this is only successful 50% of the time (with the potential of achieving 80%). Therefore, we will model this effect randomly using a filling fraction that we vary from $\eta = 0.5 \to 1$.

Laser

As previously stated, we require that the system is weakly driven, therefore we select the Rabi frequency of the laser to be $\Omega_{\mathrm{L}} = \frac{\gamma}{100}$. Recalling from Fig. 2.4**(a)** that the time taken to excite a single atom is related to the Rabi frequency by $t_{\mathrm{ex}} = \pi/\Omega_{\mathrm{L}}$, by setting Ω_{L} to be 100 times smaller than the single atom decay rate γ, we guarantee that the timescale associated with driving the single excitation is much longer than the time taken for spontaneous emissions to occur. The detuning of the laser is assumed to be within $|\Delta_{\mathrm{L}}| \leq 10\gamma$. By ensuring that the detuning is small with respect to the atom transition frequency, the laser frequency is $\omega_{\mathrm{L}} \sim \omega_{\mathrm{a}}$. This condition also ensures that $\Omega_{\mathrm{L}} \ll \omega_{\mathrm{L}}$, which satisfies the rotating wave approximation.

For the driving of a many-body system, such as a 1D chain of $N = 200$ atoms (as achieved in experiments in Palaiseau) the direction of the laser momentum vector is an important parameter to consider for the appearance of collective behaviour. We expect that the system will exhibit different features when the laser is applied at different angles. Two situations that we can compare are laser driving parallel to the chain, and perpendicular to the chain [Fig. 5.1**(a)**]. Depending on the orientation of the laser field with respect to the direction of the atomic chain, we can excite states with very different phase patterns, as demonstrated in Fig. 5.1**(b)**. In addition to these scenarios, we also explore the effect of rotating the laser field, about the perpendicular laser direction, by a small angle, and analyse the effect on collectivity [Fig. 5.1**(c)**]. An

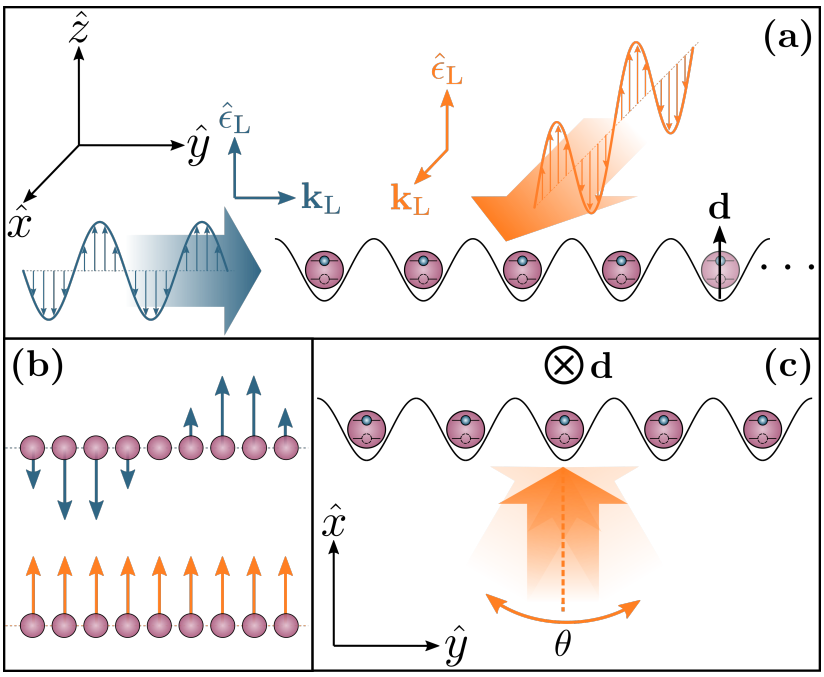

Figure 5.1: **Laser driving to a steady state.** The chain of atoms, with dipole moments aligned in the $\hat{z}$-direction, is driven by a laser field whose electric field amplitude is directed parallel to the atomic dipole moments. **(a)** The laser driving can be applied parallel to the direction of the chain in the $\hat{y}$-direction (blue), or perpendicular in the $\hat{x}$-direction (orange). The laser is applied to all lattice sites. **(b)** Examples of phase imprinting on the atoms, depending on whether the laser driving is parallel (blue) or perpendicular (orange) to the direction of the chain. **(c)** The direction of the perpendicular driving can be modified to explore a small range of angles about the $\hat{x}$-axis.

experimental requirement that we can draw from this set-up is that the width of the laser beam must encompass all atoms; if we want to excite all atoms in the chain, the width of the laser beam must be greater than the chain length $w \geq a(N-1)$. We also assume the laser drives with linearly polarised light, and for the two key orientations of the laser driving we have

- perpendicular driving: $\hat{\mathbf{k}}_{\mathrm{L}} = \hat{x}$,
- parallel driving: $\hat{\mathbf{k}}_{\mathrm{L}} = \hat{y}$.

In both cases here, the field amplitude $\hat{\epsilon}_{\mathrm{L}}$ is aligned in the $\hat{z}$-direction, which allows driving of the atomic transition with dipole moment $\mathbf{d}||\hat{z}$.

Let us now explore the relevance of these parameters, by studying the system dynamics.

5.3 Steady state properties

We begin by introducing an approximate equation for the stationary state of the system. For simplicity, in this chapter we consider the atomic system to be composed of two-level atoms. The laser field, dependent on both time and space, is given by

$$\mathbf{E}_{\mathrm{L}}(\mathbf{r}_\alpha, t) = \mathbf{E}_0 \cos\left(\omega_{\mathrm{L}} t - \mathbf{k}_{\mathrm{L}} \cdot \mathbf{r}_\alpha\right), \tag{5.1}$$

which provides us with the combination of system and laser Hamiltonians within the rotating wave approximation (see Sec. 2.5 for details)

$$H'_{\mathrm{L}} = -\frac{\hbar}{2} \sum_{\alpha=1}^{N} \left[\Delta_{\mathrm{L}} \sigma_z^\alpha + \Omega_{\mathrm{L}} (\sigma_+^\alpha \mathrm{e}^{\mathrm{i}\mathbf{k}_{\mathrm{L}}\cdot\mathbf{r}_\alpha} + \sigma_-^\alpha \mathrm{e}^{-\mathrm{i}\mathbf{k}_{\mathrm{L}}\cdot\mathbf{r}_\alpha})\right]. \tag{5.2}$$

Here, $\mathbf{k}_{\mathrm{L}} = \omega_{\mathrm{L}} \hat{\mathbf{k}}_{\mathrm{L}}/c$ is the laser momentum which tells us the direction of propagation of the field. The master equation for a many-body system of two-level atoms, interacting with both a reservoir and spatially dependent laser field is therefore

$$\begin{aligned}\dot{\rho} = -\mathrm{i} \Bigg[\Bigg\{ \sum_{\alpha=1}^{N} \left[-\frac{\Delta_{\mathrm{L}}}{2} \sigma_z^\alpha - \frac{\Omega_{\mathrm{L}}}{2} (\sigma_+^\alpha \mathrm{e}^{\mathrm{i}\mathbf{k}_{\mathrm{L}}\cdot\mathbf{r}_\alpha} + \sigma_-^\alpha \mathrm{e}^{-\mathrm{i}\mathbf{k}_{\mathrm{L}}\cdot\mathbf{r}_\alpha}) \right] + \sum_{\alpha\neq\beta}^{N} V_{\alpha\beta} \sigma_+^\alpha \sigma_-^\beta \Bigg\}, \rho \Bigg] \\ + \sum_{\alpha,\beta=1}^{N} \Gamma_{\alpha\beta} \left(\sigma_-^\beta \rho \sigma_+^\alpha - \frac{1}{2} \left\{ \sigma_+^\alpha \sigma_-^\beta, \rho \right\} \right).\end{aligned} \tag{5.3}$$

Since we model weak driving, we can therefore assume that we remain in the single excitation sector, and the state is approximately

$$|\psi(t)\rangle = c_G(t)|G\rangle + \sum_{\alpha=1}^{N} c_\alpha(t)|e\rangle_\alpha, \tag{5.4}$$

which takes the same form as Eq. (3.1), simplified for two-level atoms. Weak laser driving also allows us to make the assumption that the system exists in the low saturation limit $c_G(t) \sim 1$ [58], such that the equation of motion for the state coefficients is

$$\dot{c}_\gamma(t) = \mathrm{i}\Delta_{\mathrm{L}} c_\gamma(t) + \mathrm{i}\frac{\Omega_{\mathrm{L}}}{2} \mathrm{e}^{\mathrm{i}\mathbf{k}_{\mathrm{L}}\cdot\mathbf{r}_\gamma} - \mathrm{i} \sum_{\alpha=1}^{N} Z_{\alpha\gamma} c_\alpha(t), \tag{5.5}$$

for $\gamma = 1, \ldots, N$, where once again $Z_{\alpha\gamma} = V_{\alpha\gamma} - \mathrm{i}\frac{\Gamma_{\alpha\gamma}}{2}$. The column vector containing all coefficients therefore evolves according to

$$\dot{\mathbf{c}}(t) = \mathrm{i}(\bar{\Delta}_{\mathrm{L}} - \bar{Z})\mathbf{c}(t) + \mathrm{i}\frac{\Omega_{\mathrm{L}}}{2}\mathbf{v}, \tag{5.6}$$

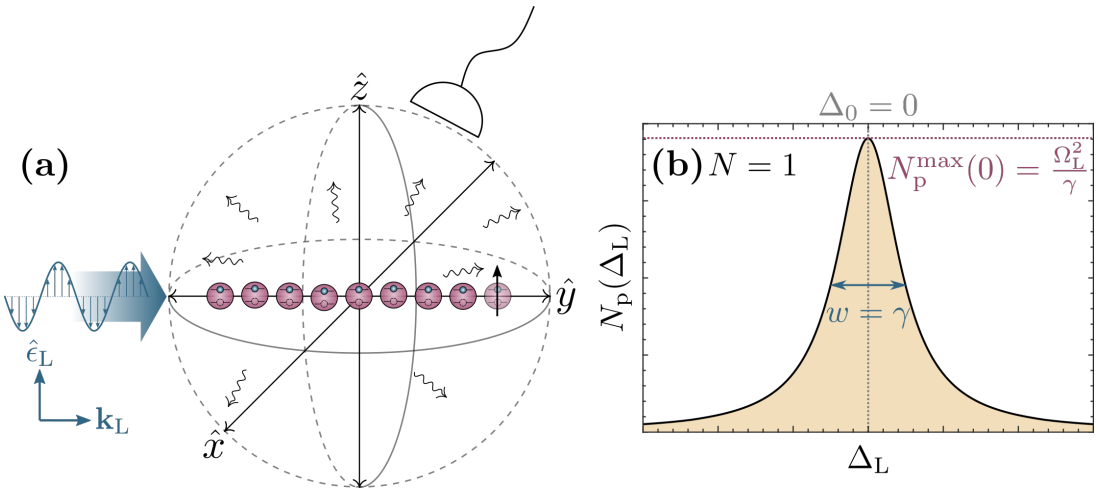

Figure 5.2: **Calculation of photon emission rate.** A chain of atoms, with dipole moments aligned in the $\hat{z}$-direction, is driven by a laser field whose electric field amplitude is directed parallel to the atomic dipole moments. The laser field encompasses the entire chain, thus all atoms are driven. **(a)** Calculation of the photon emission rate assumes that a photon detector can be placed some distance away from the chain and counts the number of photons emitted in that particular direction. The total rate assumes that we perform this counting at all positions on a sphere surrounding the chain. **(b)** For a single atom ($N = 1$), the photon emission rate N_{p} is calculated as a function of the laser detuning Δ_{L}. The Full Width Half Maximum is determined from the analytic expression (blue arrow), and returns the single atom decay rate $w = \gamma$. The maximum intensity of emission is related to the Rabi frequency Ω_{L}.

where $\bar{\Delta}_{\mathrm{L}} = \Delta_{\mathrm{L}}\mathbb{1}$ and $\mathbf{v}$ is a column vector with the α-th element given by $\mathrm{e}^{\mathrm{i}\mathbf{k}_{\mathrm{L}}\cdot\mathbf{r}_\alpha}$. After some long time, we can express the state coefficients for the steady state as $\mathbf{c}_{\mathrm{ss}} = \lim_{t\to\infty}\mathbf{c}(t)$: the system relaxes to a state that no longer evolves with time $\dot{\mathbf{c}}_{\mathrm{ss}} = 0$, and the state coefficients are

$$\mathbf{c}_{\mathrm{ss}} = -\frac{\Omega_{\mathrm{L}}}{2}(\bar{\Delta}_{\mathrm{L}} - \bar{Z})^{-1}\mathbf{v}, \tag{5.7}$$

where $\bar{M}^{-1}$ represents the matrix inverse.

5.3.1 Photon emission rate

One quantity that is probed numerically [164] and can generally be measured experimentally [165] from this type of system is the photon emission rate. We can imagine that the laser driven atomic system is surrounded by photon detectors that count the number of photons that are emitted per second, in all directions [see Fig. 5.2**(a)**].

The normalised photon emission rate is defined as

$$N_{\mathrm{p}}(\Delta_{\mathrm{L}}) = \frac{1}{N}\sum_{\alpha,\beta=1}^{N}\Gamma_{\alpha\beta}\langle\sigma_{+}^{\alpha}\sigma_{-}^{\beta}\rangle_{\mathrm{ss}}, \tag{5.8}$$

where we have scaled this quantity by the number of atoms in the system [58, 166]. This observable is measured for the steady state dynamics (denoted by $\langle\cdot\rangle_{\mathrm{ss}} = \langle\psi_{\mathrm{ss}}|\cdot|\psi_{\mathrm{ss}}\rangle$). Acting with the steady state on either side of the atomic operators returns $\langle\sigma_{+}^{\alpha}\sigma_{-}^{\beta}\rangle_{\mathrm{ss}} = \lim_{t\to\infty} c_{\alpha}^{*}(t)c_{\beta}(t)$, which allows us to express the photon emission rate as

$$N_{\mathrm{p}}(\Delta_{\mathrm{L}}) = \frac{1}{N}\bar{\Gamma}\cdot\bar{C}_{\mathrm{ss}}. \tag{5.9}$$

Here, we have defined $\bar{C}_{\mathrm{ss}} = \mathbf{c}_{\mathrm{ss}}\mathbf{c}_{\mathrm{ss}}^{\dagger}$, utilising the symmetric form of $\Gamma_{\alpha\beta} = \Gamma_{\beta\alpha}$. Taking the limit $N \to 1$, we find that

$$c_{\mathrm{ss}} = \frac{-\Omega_{\mathrm{L}}}{2\left(\Delta_{\mathrm{L}} + \mathrm{i}\frac{\gamma}{2}\right)} \quad \Rightarrow \quad N_{\mathrm{p}}(\Delta_{\mathrm{L}}) = \frac{\frac{\gamma}{4}\Omega_{\mathrm{L}}^{2}}{\Delta_{\mathrm{L}}^{2} + \left(\frac{\gamma}{2}\right)^{2}}, \tag{5.10}$$

which is a Lorentzian curve (as a function of laser detuning) with Full Width Half Maximum (FWHM) $w = \gamma$, centred at $\Delta_0 = 0$ with maximum intensity $N_{\mathrm{p}}^{\max}(0) = \Omega_{\mathrm{L}}^{2}/\gamma$, as depicted in Fig. 5.2**(b)**.

We will now explore the photon emission rate for a many-body 1D chain of atoms, varying the parameters defined in Sec. 5.2. We want to verify whether the emission spectra takes the form of a Lorentzian curve, and if so we want to extract information such as the effective decay rate. This will allow us to investigate the limitations on collective behaviour.

5.4 Spacing and angular dependence

We now use the general steady state results from the previous section to numerically study the photon emission spectra of weakly driven atomic chains, for a range of values of the interatomic spacing. Fixing the laser properties to the values defined in Sec. 5.2, we explore the effect of increasing the interatomic spacing on the photon emission rate, calculated for a chain of length $N = 200$. We begin our investigation with the perfect filling scenario ($\eta = 1$), for laser driving perpendicular to the chain direction (Sec. 5.4.1) and parallel to it (Sec. 5.4.2).

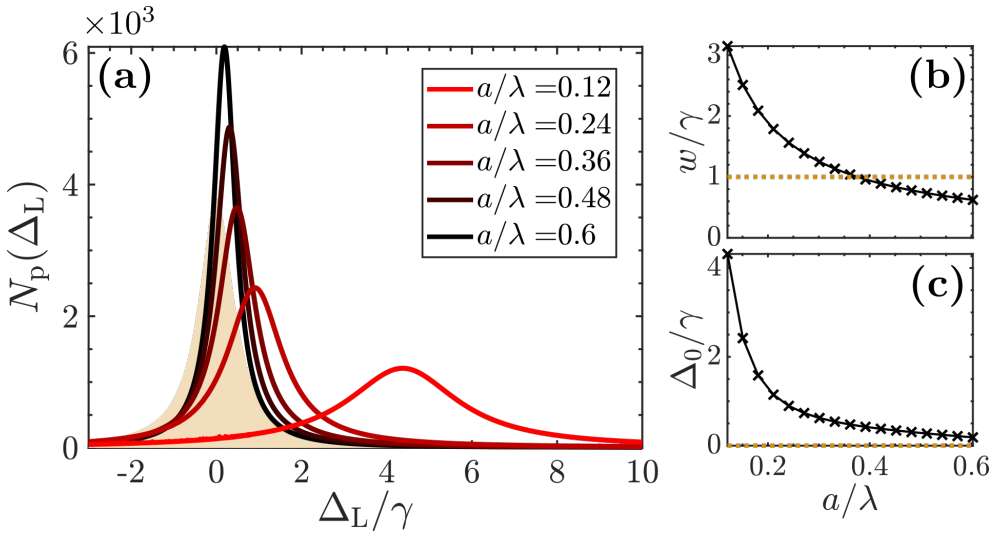

Figure 5.3: **Photon emission rate for perpendicular driving and varying spacing. (a)** The interatomic spacing ratio is varied from $a/\lambda = 0.12 \rightarrow 0.6$ (red to black lines) and the photon emission rate, scaled by the system size N, is plotted as a function of the laser detuning Δ_L. For comparison, the single atom photon emission rate is provided as the shaded orange region. From the Lorenztian form of the curves, **(b)** the width w and **(c)** the shift Δ_0 are calculated as a function of spacing, and the orange dotted lines represent the same values for the single atom case.

5.4.1 Perpendicular driving

The photon emission rate is calculated using Eq. (5.7) and Eq. (5.9), for the case represented by the orange laser driving in Fig. 5.1. It is evident from Fig. 5.3**(a)** that for the many-body case, we still observe a Lorentzian curve for the emission spectrum. For closer interatomic spacing, the peak position Δ_0 is shifted further away from $\Delta_L = 0$, and appears to be broader. However, as the separation is increased, we then observe a narrowing of the spectra, in comparison to the single atom spectrum (demonstrated by the orange shaded region). The width of these Lorentzians tell us the (collective) decay rate. We therefore numerically fit a Lorentzian curve for each ratio of a/λ, and extract the width and shift in each case, as demonstrated in Fig. 5.3**(b)** and **(c)**. For small a/λ, the width of the Lorentzian is greater than the single atom decay rate. This tells us that for a chain of atoms under constant weak driving, on average, excitations are emitted more frequently than from a single atom. The state is therefore superradiant in this regime. In a similar way, larger values of a/λ lead to a collective decay rate smaller than that of a single atom. The weakly driven chain is in a subradiant state that emits excitations less frequently than a single atom.

We examine the validity of our approach by exploring the collective single-photon decay rates, as we did in Sec. 2.4.2. In Fig. 5.4**(a)** we plot the eigenvalues that correspond to the dissipation matrix for the chain of atoms Γ_D^m, as a function of atom

spacing. We only plot one rate in every ten, due to the large system size, however we see the same features as Fig. 2.3 with sharper transitions as the subradiant rates jump to a higher value, closer to the single atom decay rate. Since we are dealing with a finite chain here, the eigenvalues are calculated numerically and ordered from most subradiant to most supperradiant.

We determine which of these decay modes are populated when we laser drive the chain with laser momentum perpendicular to the chain, by first describing the system state as

$$|\psi\rangle = \frac{1}{\sqrt{N}} \sum_{\alpha=1}^{N} \mathrm{e}^{\mathrm{i}\mathbf{k}_\mathrm{L}\cdot\mathbf{r}_\alpha} |e\rangle_\alpha = \frac{1}{\sqrt{N}} \sum_{\alpha=1}^{N} |e\rangle_\alpha, \tag{5.11}$$

since $\mathbf{k}_\mathrm{L} \cdot \mathbf{r}_\alpha = 0$ for all α. We choose $1/\sqrt{N}$ as the amplitude of this state for simplicity, since it contains exactly one excitation. Taking the overlap of the system state with all possible eigenmodes of the decay spectrum $|U_\Gamma(m)\rangle$ returns the probability of each of these decay modes emitting at their given rate. This information is highlighted in Fig. 5.4**(c)**, where we observe that for each interatomic spacing there is one state that is mostly populated at the index m_max, followed by much lower, but non-zero, population in $m_\mathrm{max} + 2$ and $m_\mathrm{max} + 4$. As a function of increasing spacing a/λ, the index of the most populated state decreases from a relatively high number until $a/\lambda = 0.5$, when we find that this index always corresponds to the first, most subradiant state.

The index m_max changes as a function of atomic spacing due to the spatial form of the eigenstates which vary for each value of a/λ. By plotting the shape of the three most populated states, in Fig. 5.4**(d)**, we can see that the general forms are equivalent (within a factor of -1) for all values of a/λ, and mimic the first three even harmonic oscillator states. Intuitively this makes sense, since our system state is an equal, symmetric superposition of all atoms being excited. Therefore, we expect the highest occupied state be the one with the most in phase contributions.

As we have previously stated, the index value m for the numeric case is also a measure of sub- and superradiance, demonstrated in Fig. 5.4**(b)**. For small spacing, m_max corresponds to a mode with a superradiant decay rate. Its value decreases as a function of a/λ until $a/\lambda \geq 0.5$, when $m_\mathrm{max} = 1$ which corresponds to the mode with the most subradiant decay rate. We verify this result by plotting the decay rate that corresponds to the most occupied mode, as a function of spacing, as a red dashed line in Fig. 5.4**(a)**.

Now that we have extracted this information, we can compare the collective decay rate to the width of the photon emission Lorentzian curve as a function of the spacing, as depicted in Fig. 5.4**(e)**. One sees immediately that these two quantities give equivalent results. Likewise, in Fig. 5.4**(f)** we compare the line shift of the peak to

$$\langle V \rangle = \langle \psi | \bar{V} | \psi \rangle, \tag{5.12}$$

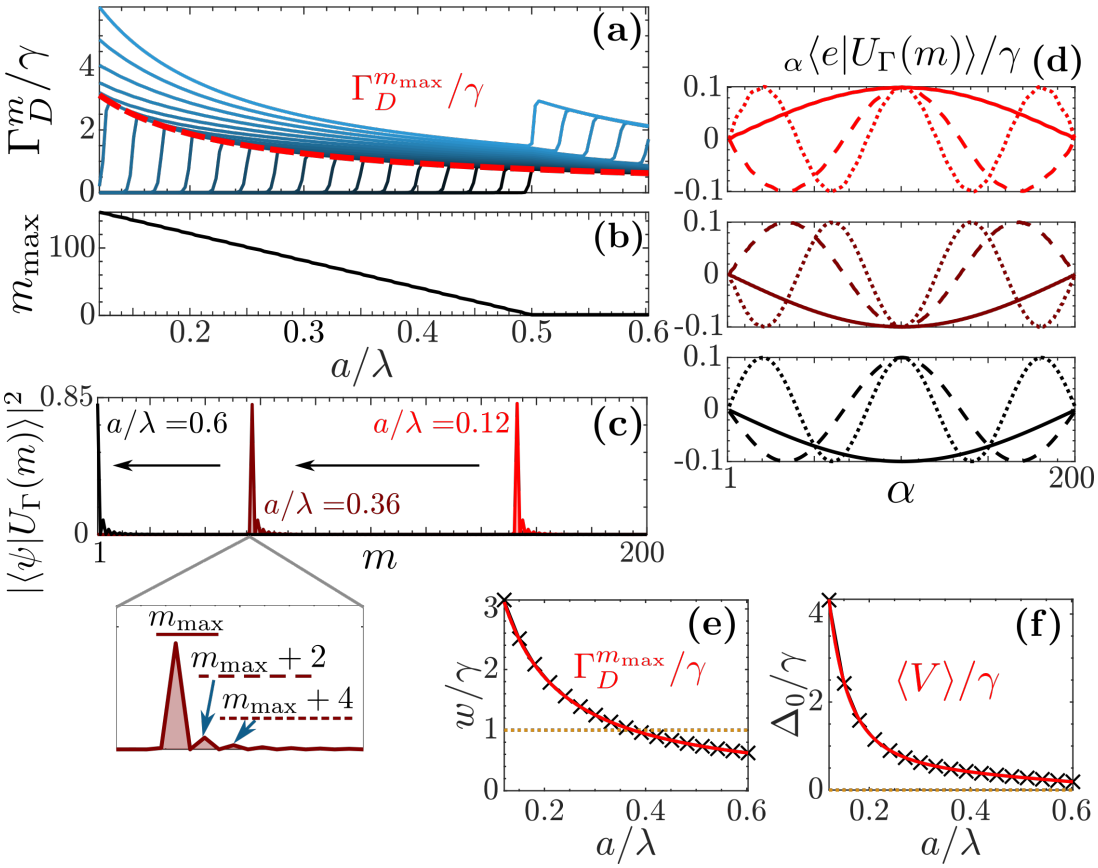

Figure 5.4: **Occupied eigenstates for perpendicular driving and varying spacing.** **(a)** The collective decay rates Γ_D^m scaled by the single atom decay rate for a chain of $N = 200$ atoms, driven by a laser perpendicular to the direction of the chain. The rates are calculated numerically and sorted from most subradiant (black) to most superradiant (blue). The overlap of the system eigenstates with a prepared state $|\psi\rangle$ is squared to return the probability of each state being occupied. The most occupied state is calculated this way and the corresponding rate is given by the red dashed line. **(b)** The index of the most occupied mode $m_{\max}$, as a function of spacing. **(c)** The probability of occupation plotted for three example spacings $a/\lambda = 0.12 \to 0.6$ (red to black) where the highest peak occurs at $m_{\max}$, followed by lesser populations in $m_{\max} + 2$ and $m_{\max} + 4$. **(d)** With increasing $a/\lambda = [0.12, 0.36, 0.6]$, from top to bottom, the three panels demonstrate the form of the eigenstates of the dissipation matrix for $m_{\max}$ (solid), $m_{\max} + 2$ (dashed) and $m_{\max} + 4$ (dotted). Overlaying the results (black crosses) from Fig. 5.3 for **(e)** the width of the Lorentzian curves, where the solid red line represents the most occupied decay rate $\Gamma_D^{m_{\max}}$, and **(f)** the shift of the Lorentzian curves, where the solid red line is the corresponding energy $\langle V\rangle = \langle\psi|\bar{V}|\psi\rangle$ using the coherent interaction matrix.

which is simply the expectation value of the interaction energy in this state [167]. We again see a direct mapping from one result to the other.

These results imply that we can theoretically extract a set of expected results for the experimental photon rate measurement, using the effective Hamiltonian describing the many-body atomic system. In addition to this result, analysis of the decay spec-

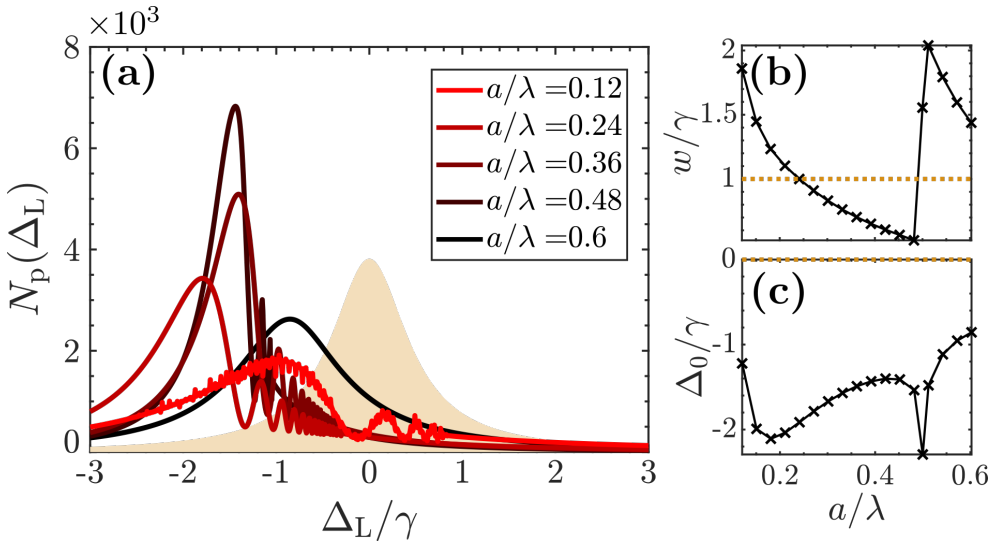

Figure 5.5: **Photon emission for parallel driving and varying spacing.** **(a)** The interatomic spacing ratio is varied from $a/\lambda = 0.12 \rightarrow 0.6$ (red to black lines) and the photon emission rate, scaled by the system size N, is plotted as a function of the laser detuning Δ_L. For comparison, the single atom photon emission rate is provided as the shaded orange region. From the Lorenztian form of the curves, **(b)** the width w and **(c)** the shift Δ_0 are calculated as a function of spacing, and the orange dotted lines represent the same values for the single atom case.

trum suggests that even for perfect filling, the most subradiant mode will never drop below $\Gamma_D^m \sim 0.6$, hence an excitation in this state has a finite lifetime.

5.4.2 Parallel driving

Let us now perform the same calculations for parallel laser driving (represented by the blue laser direction in Fig. 5.1). We calculate the photon emission rate, once again, for a varying interatomic spacing a/λ, as demonstrated in Fig. 5.5**(a)**. In this case, the peaks are no longer necessarily accurately represented by a Lorentzian curve. The fit becomes more appropriate as the spacing is increased. For small values of a/λ, we see the appearance of additional peaks, which may be caused by numerous eigenstates - with varying decay rates - being occupied. We still attempt to fit the Lorentzian curve, in order to extract the width and shift of the most prominent peaks, and the results are plotted in Fig. 5.5**(b)** and **(c)**. We follow with the same analysis as Sec. 5.4.1 to investigate where these additional peaks originate from.

Since the states of the effective Hamiltonian (containing the dissipation and coherent interaction matrices) are independent of the laser driving, the collective decay rates remain the same as those presented in Fig. 5.4**(a)**. However, we now model the

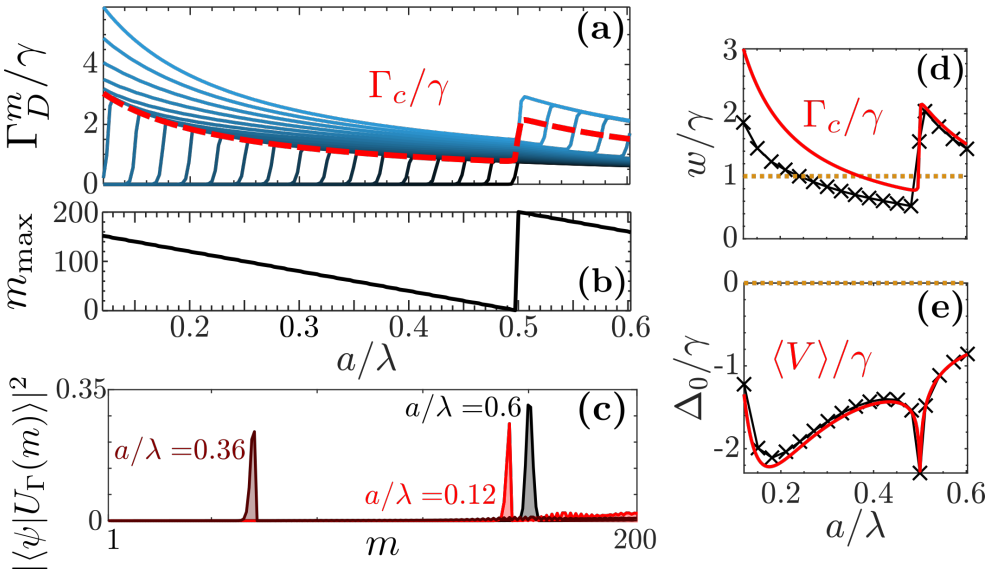

Figure 5.6: **Occupied eigenstates for parallel driving and varying spacing.** **(a)** The decay rates Γ_D^m scaled by the single atom decay rate for a chain of $N = 200$ atoms, driven by a laser parallel to the direction of the chain. The rates are calculated numerically and sorted from most subradiant (black) to most superradiant (blue). The overlap of the system eigenstates with a prepared state $|\psi\rangle$ is squared to return the probability of each state being occupied. The red dashed line corresponds to the sum of all rates, weighted by the probability of the equivalent state being occupied (activity). **(b)** The index of the most occupied mode $m_{\max}$, as a function of spacing. **(c)** The probability of occupation plotted for three example spacings $a/\lambda = 0.12 \rightarrow 0.6$ (red to black). Overlaying the results (black crosses) from Fig. 5.5 for **(d)** the width of the Lorentzian curves, where the solid red line represents the weighted sum of decay rates Γ_c and **(e)** the shift of the Lorentzian curves, where the solid red line is the corresponding interaction energy $\langle V\rangle = \langle\psi|\bar{V}|\psi\rangle$ using the coherent interaction matrix.

state of the system $|\psi\rangle$ such that

$$|\psi\rangle = \frac{1}{\sqrt{N}}\sum_{\alpha=1}^{N} \mathrm{e}^{\mathrm{i}\mathbf{k}_\mathrm{L}\cdot\mathbf{r}_\alpha}|e\rangle_\alpha = \frac{1}{\sqrt{N}}\sum_{\alpha=1}^{N} \mathrm{e}^{\frac{\mathrm{i}\omega_\mathrm{L}\alpha a}{c}}|e\rangle_\alpha \approx \frac{1}{\sqrt{N}}\sum_{\alpha=1}^{N} \mathrm{e}^{\frac{2\pi\mathrm{i}\alpha a}{\lambda}}|e\rangle_\alpha, \qquad (5.13)$$

where we have used that $\Delta_\mathrm{L} \ll \omega_\mathrm{a}$.

Acting this state on the eigenstates gives us the probability of each eigenstate being occupied, as shown in Fig. 5.6**(c)**. In contrast to the perpendicular driving case, this time we see that there are a number of occupied states centred about $m_{\max}$ with no one state exceeding a probability of 0.35. We can consider this as a wave packet in state space with a centre $m_{\max}$ that decreases as a function of atom separation, until $a/\lambda = 0.5$, when the centre exhibits a sharp transition to $m_{\max} = 200$ before decreasing again [see Fig. 5.6**(b)**]. In addition to the wave packet, lower values of a/λ also exhibit non-zero occupation for high m, spread across many of the superradiant modes. Due to these reasons, it no longer makes sense to observe the form of indi-

vidual eigenstates, and the system is unlikely to decay at a rate assigned to a single eigenstate. We therefore calculate the weighted sum of all decay rates

$$\Gamma_c = \sum_{k=1}^{N} \Gamma_D^m |\langle\psi|U_\Gamma(m)\rangle|^2 = K, \tag{5.14}$$

which is equivalent to the activity of the system, in this particular state $|\psi\rangle$. The activity is plotted in both Fig. 5.6**(a)** as a dashed red line, and in Fig. 5.6**(d)** as a solid red line. We also plot the expectation value of the interaction energy in Fig. 5.6**(e)**.

Where the perpendicular driving provided almost identical mapping from the collective decay and interaction energy onto the Lorentzian width and shift, we see here that the upper panel is only consistent for $a/\lambda \gtrapprox 0.5$. For smaller spacing, the Lorentzian underestimates the width of the peak (ignoring the smaller peaks due to other decay modes). On the other hand, the line shift of the peak still accurately represents the interaction energy.

The results from Sec. 5.4.1 and Sec. 5.4.2 provide a clear link between the form of photon emission rate, as a function of laser detuning, and decay and energy quantities that can be extracted directly from the non-Hermitian effective Hamiltonian that evolves the many-body system without laser interactions. This opens up avenues to further investigate which scenarios may exhibit collective behaviour using a theoretical understanding that can mirror expected experimental results.

5.4.3 Other angles

From the results detailed in the previous two sections, we have learned the following outcomes:

- Collective behaviour is exhibited differently depending on the direction of laser driving.
- For lengthscales of experimental interest, collectivity is greatly reduced.
- We can switch from a superradiant to subradiant regime, by altering the spacing between atoms with respect to the transition wavelength.

While the features of cooperative behaviour are less apparent in the experimental regime outlined in Sec. 5.2, the changing regimes still provide interesting results to accompany the understanding of interacting many-body systems. We now explore the transition between collective regimes, for various spacings, by rotating the angle of the laser about the perpendicular driving regime [see Fig. 5.1**(c)**].

Firstly, we assume that the laser can still act on all lattice sites within the chain regardless of the rotation angle. We restrict to a rotation of the laser, where θ is in the

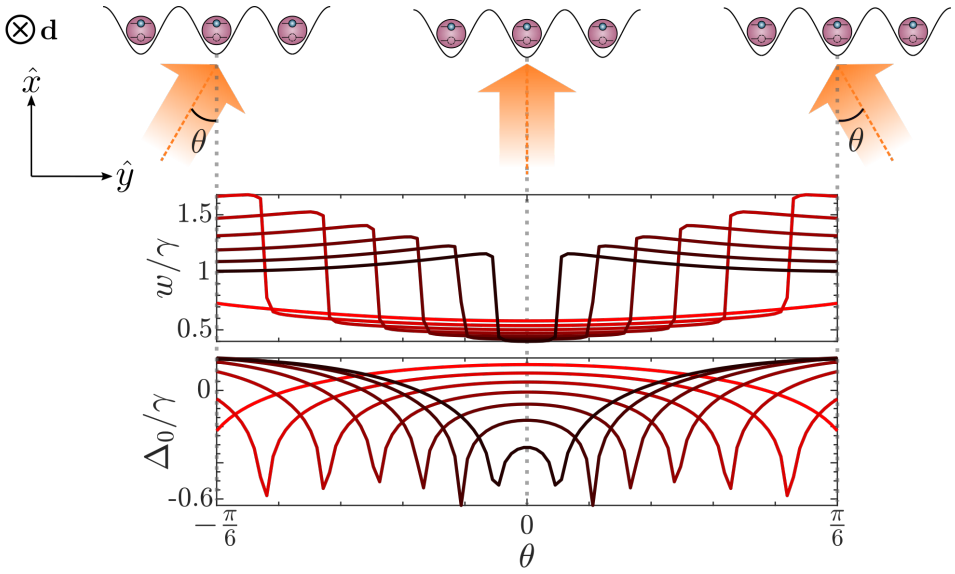

Figure 5.7: **Rotating the driving angle.** An atomic chain is driven by a laser, rotated by an angle θ from the direction perpendicular to the chain direction. The widths w (top) and shifts Δ_0 (bottom) are extracted from a set of Lorentzian curves that are produced by calculating the photon emission rate of the system for interatomic spacings $a/\lambda = 0.65 \rightarrow 0.95$ (red to black).

interval $[-\frac{\pi}{6}, \frac{\pi}{6}]$, about the $\hat{x}$-axis away from the orientation used for the perpendicular application, in alignment with discussed experimental restrictions. A negative θ represents a clockwise rotation of the laser, while positive θ represents an anticlockwise rotation, see Fig. 5.1**(c)** for reference. This range of angles corresponds to a range of laser angles $\theta_{\mathrm{L}} = \frac{\pi}{2} + \theta$ in the interval $[\frac{\pi}{3}, \frac{2\pi}{3}]$ where the laser angle is defined through

$$\mathbf{k}_{\mathrm{L}} \cdot \hat{\mathbf{r}}_\alpha = \frac{\omega_{\mathrm{L}}}{c} \cos\theta_{\mathrm{L}}. \tag{5.15}$$

We take a fixed value for the atomic spacing, and for each value of θ we calculate the photon emission rate. From each Lorentzian curve fitted to this data, we find the width and the shift of the peak and plot these parameters as a function of the laser rotation. This process is repeated for a variety of spacings ranging from $a/\lambda = 0.65 \rightarrow 0.95$ and the results are demonstrated in Fig. 5.7. In this simulation, we have exceeded the lengthscale $a/\lambda = 0.6$ that we were initially trying to explore. This is because the restriction on the angle prevents us from seeing any interesting behaviour. We verify this by observing the most red line ($a/\lambda = 0.65$) in Fig. 5.7. This line remains trivial for all angles, however the higher spacing results exhibit sharp symmetric transitions at a given angle for each case.

For all spacings, as the laser angle approaches the perpendicular alignment (from either side), the width drops from above to below the single atom decay rate. The tran-

sition suggests that by bringing the laser into perpendicular alignment, we suddenly enter a subradiant state. In addition to this, we see sharp peaks in the shifts (interaction energy) at the same angles for each curve. These features could potentially be measured in an experimental scenario, and would allow one to determine the required precision of the laser direction in order to achieve the most subradiant state possible.

5.5 Imperfect filling

The robustness of the investigations presented above can be tested by implementing an imperfect filling fraction at an interatomic spacing relevant to the experimental regime ($a/\lambda = 0.6$). From Fig. 5.8**(a)** and **(b)** we observe that the width of the Lorentzian curves approaches the single atom decay rate for both perpendicular and parallel laser driving as the lattice occupancy decreases. The subradiance that appears from perpendicular driving diminishes, while the chain becomes less superradiant for parallel driving. In addition, the shift of the peaks from $\Delta_{\mathrm{L}} = 0$ decreases for random, imperfect filling, but remains non-zero. It is clear from these results that while collective behaviour is still present and potentially measurable for filling fractions as low as $\eta = 0.5$, the features are weakened.

On the other hand, one may still be able to calculate the precise angle when the applied laser driving changes from exciting a superradiant state to a subradiant state, based on the results of Fig. 5.8**(c)**. The calculation outlined in Sec. 5.4.3 is repeated for filling fractions $\eta = 0.8$ and $\eta = 0.5$, to demonstrate the dependence of the width and shift of the photon emission rate spectra on the angle of the laser driving. For each case of random filling disorder, the width and shift follow the same form as for full filling, with the exception that the magnitudes are lessened. The sharp transitions in the width and the spikes in the shift are still evident and occur at the same angles for each value of η. Therefore, depending on the precision of the experimental apparatus used to measure the photon emission rate, these transition angles could still be measurable in the presence of filling disorder.

5.6 Conclusions and outlook

In this chapter, we have taken the investigations performed in Chapter 3 and limited the physical parameters to better represent an experimentally realisable system. By exploring nearest neighbour atomic spacing that coincides with the wavelength of a particular optical lattice, we have been able to explore the robustness of collective behaviour in this regime, which may help to steer the direction of future experimental investigations.

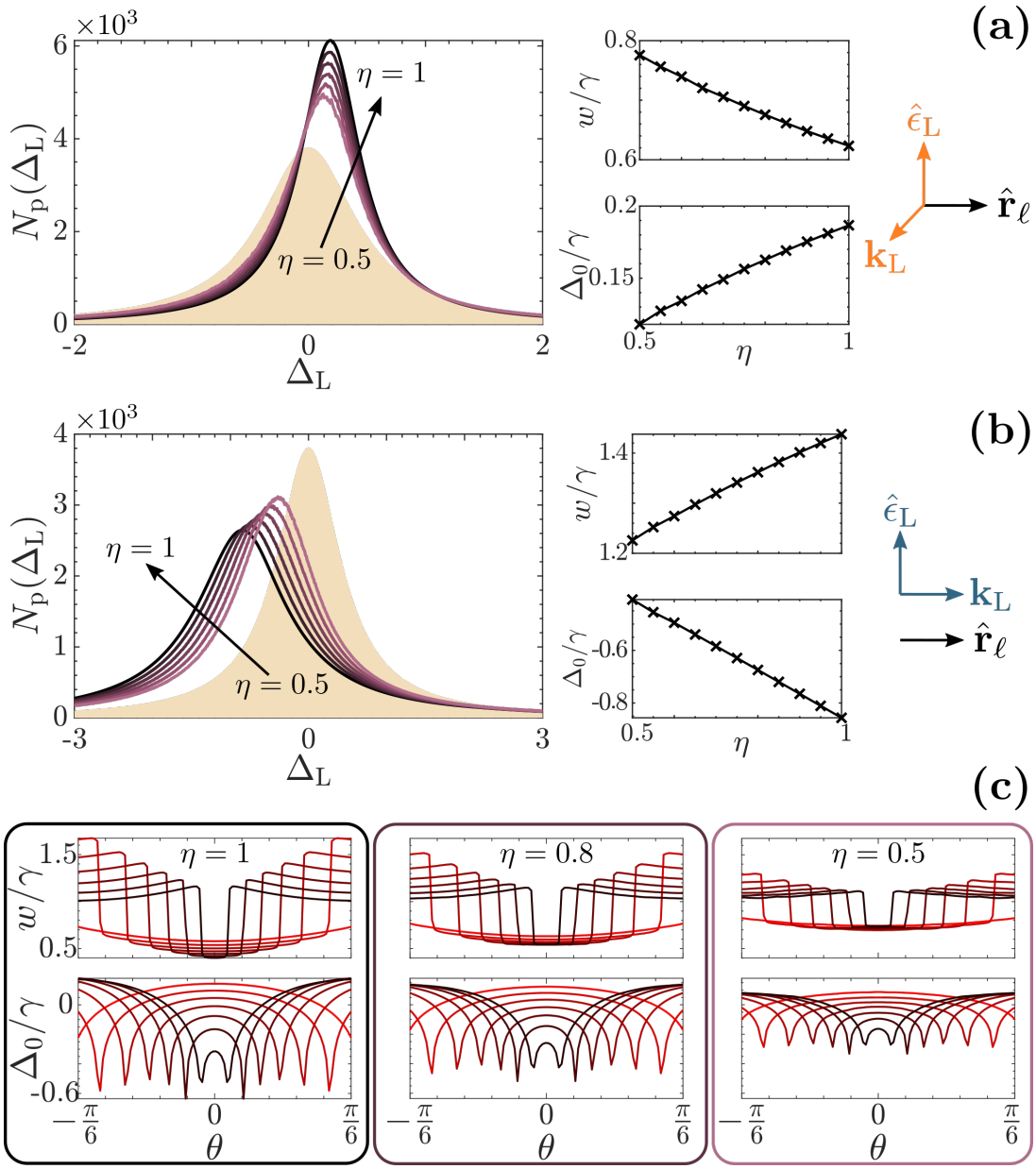

Figure 5.8: **Random imperfect filling.** Photon emission rate $N_{\rm p}(\Delta_{\rm L})$ as a function of laser detuning (left panels) calculated for a chain of atoms with laser driving **(a)** perpendicular and **(b)** parallel to the direction of the chain $\hat{\mathbf{r}}_\alpha$. The chain has $N_{\rm sites} = 200$ lattice sites, equally spaced by $a = 0.6\lambda$, and is occupied with a random filling of $\eta = 0.5 \rightarrow 1$ (pink to black) such that the total number of atoms in the chain is $N = \eta N_{\rm sites}$. Each curve is formed from the average of 20 realisations of random filling. The right panels demonstrate the width w (top) and shift Δ_0 (bottom) of the averaged peaks as a function of random filling. **(c)** Rotating about the perpendicular laser driving alignment, the width (top) and shift (bottom) of the curves are calculated for three cases of random filling, as a function of angle. The fully occupied case in the leftmost box provides the benchmark, and two examples of imperfect filling with $\eta = 0.8$ (middle) and $\eta = 0.5$ (right) are presented for 10 realisations of random occupation.

Defining a theoretical method to calculate the photon emission rate allows for comparison to experimental techniques, while exploration of the dissipation and interaction spectra permits the extraction of system decay rates and energy. By outlining and comparing these methods, we are able to make predictions on experimental measurements of the photon emission rate which relate directly to physics derived from first principles.

We have determined the limit for subradiance on these lengthscales, which is still present, but without capabilities for near-infinite lifetimes. However, in this process we have detected various ways in which the system can exhibit features of collective behaviour, depending on external factors such as the direction of laser driving. In fact, by extending the spatial limit further, we retain the ability to detect and separate superradiant and subradiant behaviour, based on the laser momentum.

In addition to investigations on lengthscale, we briefly explored experimental limitations on the filling of a 1D optical lattice. Intuitively, the best case scenario corresponds to perfect occupation, however we note that collectivity is still identifiable in the presence of imperfections. This particular set of results could potentially lead to an interesting, analogous experimental investigation, since a chain with imperfections is readily prepared.

An additional experimental limitation that should be considered in future iterations of this model is the spatial uniformity of the laser driving. In this chapter, we assumed that all atoms were driven equally by the laser, i.e. the width of the laser encompasses all atoms. This may not be the case in reality, and the angle of laser driving could change which lattice sites are illuminated. This project could therefore be extended by accounting for the finite width of the laser beam. The modified model would make for an interesting comparison to equivalent experiments.

Chapter 6
Conclusion

In this thesis, we have studied how collective behaviour arises in open, many-body atomic systems for geometries such as one-dimensional atomic arrays – with finite and periodic boundaries – and three-dimensional atomic gases. By modelling the atoms simply, with two or four levels, we were able to outline the well-known derivation for the open quantum master equation that describes the system dynamics in Chapter 2. Enabled by long range interactions, we identified coefficients in the Lindblad equation relating to coherent exchange of virtual photons and modified decay rates, which could be adapted further by application of a laser or external magnetic field. Following a description of the current known results regarding open many-body systems of two- and four-level atoms, we were able to explore these features of collectivity to a greater extent in Chapter 3. We proceeded to outline a protocol for excitation transport which utilised photon exchange and subradiance in the single excitation sector. Here, we introduced our first set of new findings in the field of collective behaviour in many-body atomic systems. We have gained an intuition behind the mechanisms that enable coherent transport by identifying how the collective decay rate and corresponding wave packet velocity can be extracted from, or defined by, a given initial state in k-space.

This type of analysis has enabled us to predict and simulate the system behaviour, accounting for a number of discussed experimental considerations. For instance, we first introduced the idea of positional disorder by defining the position of the atoms within a lattice array to be offset from the lattice sites by an amount selected from a Gaussian distribution. We could refer to this type of positional disorder as classical, and we were required to simulate dynamics over many realisations of this disorder. In Chapter 4, we considered the same type of disorder as an intrinsic property of the atoms, represented by a quantum motional state describing the atomic positions and momenta. Deriving the equivalent system master equation, utilising a novel technique described in recent literature [77], we modelled atomic motion as part of the bath, which allowed us to understand the uncertain nature of atomic positions within lattice traps as an inbuilt feature. We modified this derivation to specifically explore one-dimensional chain geometries of atoms, and we provided insight to the effect of motion on energy transport in these systems. Our discussions were made in the low temperature limit, where the atomic motion is essentially frozen. This project could

be extended further by moving out of the frozen regime. Here we would not neglect the time dependence appearing in the motional correlations between the external and internal atomic degrees of freedom. This type of analysis would have direct relevance to experiments regarding thermal atomic clouds [25], and additional theoretical work [168] where Doppler broadening and recoil are suggested to play important roles in the modification of collective behaviour.

We explored additional experimental constraints in Chapter 5, such as the limitation on close spacing between atoms, and the difficulty with achieving perfect, single atom per site filling within a realistic optical lattice. We outlined a theoretical method for calculating the photon emission rate which is an experimentally measurable quantity. By extrapolating the results previously found for a set-up within the collective regime, we could directly relate quantities extracted from the Lindblad equation to real measurable observables. The results presented in this chapter demonstrate that atoms trapped in optical lattices, in regular arrangements achieved with current experimental capabilities, can exhibit collective behaviour albeit greatly reduced in comparison to the examples demonstrated in Chapter 3. It would be interesting to see if experimental results could mirror the results described in this chapter, and whether trapping could be achieved at lengthscales required to occupy the truly subradiant decay manifold. The investigations of this chapter were mostly inspired by discussions with the Quantum Optics – Atoms group at the Institut d'Optique in Palaiseau. With the intention of creating an optical lattice with the parameters described in Chapter 5, our goal was to explore the level of collectivity that one might expect to observe in such a system. Following this research, we hope to continue collaborating with the Institut d'Optique in Palaiseau.

A future direction connecting to this work will be to move away from the linear optics regime (single excitation sector of the dynamics) [58, 60, 62, 63, 169] and consider situations where two or more wave packets interfere with each other to effectively realise photon-photon interactions in a subradiant decoherence-free manifold. This extension, of course, vastly increases the Hilbert space of the many-body system, and may require a different computational treatment to model the system dynamics. In this case, one would consider utilising quantum jump Monte Carlo methods to model instances of the dynamics, which would be averaged over many realisations to create the probabilistic dynamics. Such a platform can find applications ranging from the creation of non-classical states of light [38] to the realisation of photon-photon quantum gates [170]. With a number of avenues that this research could take, along with a variety of potential applications, this work could continue to provide many fruitful insights into the field of quantum optics.

Bibliography

[1] P. A. M. Dirac. The quantum theory of the emission and absorption of radiation. *P. Roy. Soc. A Math. Phy.*, 114(767):243–265, 1927.

[2] V. Weisskopf and E. Wigner. Calculation of the natural brightness of spectral lines on the basis of dirac's theory. *Z. Phys.*, 63:54–73, 1930.

[3] A. Einstein. Zur quantentheorie der strahlung. *Phys. Z.*, 18:124, 1917.

[4] T. H. Maiman. Stimulated optical radiation in ruby. *Nature*, 187(4736):493–494, 1960.

[5] E. T. Jaynes and F. W. Cummings. Comparison of quantum and semiclassical radiation theories with application to the beam maser. *P. IEEE*, 51(1):89–109, 1963.

[6] F. Damanet, A. J. Daley, and J. Keeling. Atom-only descriptions of the driven-dissipative Dicke model. *Phys. Rev. A*, 99(3):033845, 2019.

[7] H.-P. Breuer, F. Petruccione, et al. *The theory of open quantum systems*. Oxford University Press on Demand, 2002.

[8] J. Von Neumann. Wahrscheinlichkeitstheoretischer aufbau der quantenmechanik. *Nach. Ges. Wiss. Göttingen*, 11:245–272, 1927.

[9] G. Lindblad. On the generators of quantum dynamical semigroups. *Commun. Math. Phys.*, 48(2):119–130, 1976.

[10] D. Chruściński and S. Pascazio. A brief history of the gkls equation. arXiv:1710.05993, 2017.

[11] R. H. Dicke. Coherence in spontaneous radiation processes. *Phys. Rev.*, 93:99, 1954.

[12] R. H. Lehmberg. Radiation from an N-atom system. I. General formalism. *Phys. Rev. A*, 2:883, 1970.

[13] G. S. Agarwal. Master-equation approach to spontaneous emission. II. Emission from a system of harmonic oscillators. *Phys. Rev. A*, 3:1783, 1971.

[14] B. Olmos, D. Yu, Y. Singh, F. Schreck, K. Bongs, and I. Lesanovsky. Long-range interacting many-body systems with alkaline-earth-metal atoms. *Phys. Rev. Lett.*, 110:143602, 2013.

[15] R. T. Sutherland and F. Robicheaux. Collective dipole-dipole interactions in an atomic array. *Phys. Rev. A*, 94:013847, 2016.

[16] R. J. Bettles, S. A. Gardiner, and C. S. Adams. Cooperative eigenmodes and scattering in one-dimensional atomic arrays. *Phys. Rev. A*, 94:043844, 2016.

[17] C. Cohen-Tannoudji, J. Dupont-Roc, and G. Grynberg. *Photons and Atoms-Introduction to Quantum Electrodynamics*. 1997.

[18] R. Friedberg, S.R. Hartmann, and J.T. Manassah. Frequency shifts in emission and absorption by resonant systems of two-level atoms. *Phys. Rep.*, 7(3):101, 1973.

[19] M. O. Scully. Collective Lamb shift in single photon dicke superradiance. *Phys. Rev. Lett.*, 102:143601, 2009.

[20] J. Keaveney, A. Sargsyan, U. Krohn, I. G. Hughes, D. Sarkisyan, and C. S. Adams. Cooperative Lamb shift in an atomic vapor layer of nanometer thickness. *Phys. Rev. Lett.*, 108:173601, 2012.

[21] J. Pellegrino, R. Bourgain, S. Jennewein, Y. R.P. Sortais, A. Browaeys, S. D. Jenkins, and J. Ruostekoski. Observation of suppression of light scattering induced by dipole-dipole interactions in a cold-atom ensemble. *Phys. Rev. Lett.*, 113:133602, 2014.

[22] S. D. Jenkins, J. Ruostekoski, J. Javanainen, S. Jennewein, R. Bourgain, J. Pellegrino, Y. R. P. Sortais, and A. Browaeys. Collective resonance fluorescence in small and dense atom clouds: Comparison between theory and experiment. *Phys. Rev. A*, 94:023842, 2016.

[23] S. L. Bromley, B. Zhu, M. Bishof, X. Zhang, T. Bothwell, J. Schachenmayer, T. L. Nicholson, R. Kaiser, S. F. Yelin, M. D. Lukin, A. M. Rey, and J. Ye. Collective atomic scattering and motional effects in a dense coherent medium. *Nat. Comm.*, 7:11039, 2016.

[24] T. Peyrot, Y. R. P. Sortais, A. Browaeys, A. Sargsyan, D. Sarkisyan, J. Keaveney, I. G. Hughes, and C. S. Adams. Collective Lamb shift of a nanoscale atomic vapor layer within a sapphire cavity. *Phys. Rev. Lett.*, 120:243401, 2018.

[25] T. Bienaimé, N. Piovella, and R. Kaiser. Controlled Dicke subradiance from a large cloud of two-level systems. *Phys. Rev. Lett.*, 108:123602, 2012.

[26] J. R. Ott, M. Wubs, P. Lodahl, N. A. Mortensen, and R. Kaiser. Cooperative fluorescence from a strongly driven dilute cloud of atoms. *Phys. Rev. A*, 87:061801, 2013.

[27] R. A. de Oliveira, M. S. Mendes, W. S. Martins, P. L. Saldanha, J. W. R. Tabosa, and D. Felinto. Single-photon superradiance in cold atoms. *Phys. Rev. A*, 90:023848, 2014.

[28] W. Guerin, M. O. Araújo, and R. Kaiser. Subradiance in a large cloud of cold atoms. *Phys. Rev. Lett.*, 116:083601, 2016.

[29] S. J. Roof, K. J. Kemp, M. D. Havey, and I. M. Sokolov. Observation of single-photon superradiance and the cooperative Lamb shift in an extended sample of cold atoms. *Phys. Rev. Lett.*, 117(7):073003, 2016.

[30] M. O. Araújo, W. Guerin, and R. Kaiser. Decay dynamics in the coupled-dipole model. *J. Mod. Opt.*, 65(11):1345, 2018.

[31] F. Cottier, R. Kaiser, and R. Bachelard. Role of disorder in super- and subradiance of cold atomic clouds. *Phys. Rev. A*, 98:013622, 2018.

[32] D. Jaksch, C. Bruder, J. I. Cirac, C. W. Gardiner, and P. Zoller. Cold bosonic atoms in optical lattices. *Phys. Rev. Lett.*, 81(15):3108, 1998.

[33] I. Bloch. Ultracold quantum gases in optical lattices. *Nat. Phys.*, 1(1):23, 2005.

[34] H. Bernien, S. Schwartz, A. Keesling, H. Levine, A. Omran, H. Pichler, S. Choi, A. S. Zibrov, M. Endres, M. Greiner, et al. Probing many-body dynamics on a 51-atom quantum simulator. *Nature*, 551(7682):579–584, 2017.

[35] R. J. Bettles, Ji ří Minář, C. S. Adams, I. Lesanovsky, and B. Olmos. Topological properties of a dense atomic lattice gas. *Phys. Rev. A*, 96:041603, 2017.

[36] G. Facchinetti, S. D. Jenkins, and J. Ruostekoski. Storing light with subradiant correlations in arrays of atoms. *Phys. Rev. Lett.*, 117:243601, 2016.

[37] T. Laycock, B. Olmos, and I. Lesanovsky. Creation of collective many-body states and single photons from two-dimensional Rydberg lattice gases. *J. Phys. B*, 44:184017, 2011.

[38] A. V. Gorshkov, J. Otterbach, M. Fleischhauer, T. Pohl, and M. D. Lukin. Photon-photon interactions via Rydberg blockade. *Phys. Rev. Lett.*, 107:133602, 2011.

[39] B. Olmos and I. Lesanovsky. Collective photon emission from symmetric states created with Rydberg atoms on a ring lattice. *Phys. Rev. A*, 82:063404, 2010.

[40] J. Wilson, S. Saskin, Y. Meng, S. Ma, A. Burgers, and J. Thompson. Trapped arrays of alkaline earth Rydberg atoms in optical tweezers. arXiv:1912.08754, 2019.

[41] H. Zoubi. Collective light emission of a finite-size atomic chain. *EPL*, 100(2):24002, 2012.

[42] A. J. Daley, M. Rigol, and D. S. Weiss. Focus on out-of-equilibrium dynamics in strongly interacting one-dimensional systems. *New J. Phys.*, 16(9):095006, 2014.

[43] D. F. Kornovan, N. V. Corzo, J. Laurat, and A. S. Sheremet. Extremely subradiant states in a periodic one-dimensional atomic array. *Phys. Rev. A*, 100(6):063832, 2019.

[44] H. Zoubi and H. Ritsch. Optical properties of collective excitations for finite chains of trapped atoms, 2011. arXiv:1106.4923.

[45] R. J. Bettles, S. A. Gardiner, and C. S. Adams. Enhanced optical cross section via collective coupling of atomic dipoles in a 2D array. *Phys. Rev. Lett.*, 116(10):103602, 2016.

[46] G. Facchinetti and J. Ruostekoski. Interaction of light with planar lattices of atoms: Reflection, transmission, and cooperative magnetometry. *Phys. Rev. A*, 97(2):023833, 2018.

[47] E. Shahmoon, D. S. Wild, M. D. Lukin, and S. F. Yelin. Cooperative resonances in light scattering from two-dimensional atomic arrays. *Phys. Rev. Lett.*, 118(11):113601, 2017.

[48] J. Rui, D. Wei, A. Rubio-Abadal, S. Hollerith, J. Zeiher, D. M. Stamper-Kurn, C. Gross, and I. Bloch. A subradiant optical mirror formed by a single structured atomic layer. arXiv:2001.00795, 2020.

[49] E. Fort and S. Grésillon. Surface enhanced fluorescence. *J. Phys. D App. Phys.*, 41(1):013001, 2007.

[50] E. M. Purcell, H. C. Torrey, and R. V. Pound. Resonance absorption by nuclear magnetic moments in a solid. *Phys. Rev.*, 69(1-2):37, 1946.

[51] P. T. Worthing, R. M. Amos, and W. L. Barnes. Modification of the spontaneous emission rate of Eu 3+ ions embedded within a dielectric layer above a silver mirror. *Phys. Rev. A*, 59(1):865, 1999.

[52] R. M. Amos and W. L. Barnes. Modification of the spontaneous emission rate of Eu 3+ ions close to a thin metal mirror. *Phys. Rev. B*, 55(11):7249, 1997.

[53] R. Jones, J. A. Needham, I. Lesanovsky, F. Intravaia, and B. Olmos. Modified dipole-dipole interaction and dissipation in an atomic ensemble near surfaces. *Phys. Rev. A*, 97:053841, 2018.

[54] M. O. Scully, E. S. Fry, C. H. R. Ooi, and K. Wódkiewicz. Directed spontaneous emission from an extended ensemble of n atoms: Timing is everything. *Phys. Rev. Lett.*, 96:010501, 2006.

[55] D. Plankensteiner, L. Ostermann, H. Ritsch, and C. Genes. Selective protected state preparation of coupled dissipative quantum emitters. *Sci. Rep.*, 5:16231, 2015.

[56] M. O. Scully. Single photon subradiance: Quantum control of spontaneous emission and ultrafast readout. *Phys. Rev. Lett.*, 115:243602, 2015.

[57] H. H. Jen, M. S. Chang, and Y. C. Chen. Cooperative single-photon subradiant states. *Phys. Rev. A*, 94:013803, 2016.

[58] A. Asenjo-Garcia, M. Moreno-Cardoner, A. Albrecht, H. J. Kimble, and D. E. Chang. Exponential improvement in photon storage fidelities using subradiance and "selective radiance" in atomic arrays. *Phys. Rev. X*, 7:031024, 2017.

[59] H. H. Jen. Phase-imprinted multiphoton subradiant states. *Phys. Rev. A*, 96:023814, 2017.

[60] H. H. Jen. Directional subradiance from helical-phase-imprinted multiphoton states. *Sci. Rep.*, 8(1):1–8, 2018.

[61] H. H. Jen, M.-S. Chang, and Y.-C. Chen. Cooperative light scattering from helical-phase-imprinted atomic rings. *Sci. Rep.*, 8:9570, 2018.

[62] M. Moreno-Cardoner, D. Plankensteiner, L. Ostermann, D. E Chang, and H. Ritsch. Extraordinary subradiance with lossless excitation transfer in dipole-coupled nano-rings of quantum emitters. arXiv:1901.10598, 2019.

[63] P.-O. Guimond, A. Grankin, D. V. Vasilyev, B. Vermersch, and P. Zoller. Subradiant bell states in distant atomic arrays. *Phys. Rev. Lett.*, 122:093601, 2019.

[64] J. Perczel, J. Borregaard, D. E. Chang, H. Pichler, S. F. Yelin, P. Zoller, and M. D. Lukin. Topological quantum optics in two-dimensional atomic arrays. *Phys. Rev. Lett.*, 119:023603, 2017.

[65] B. Willingham and S. Link. Energy transport in metal nanoparticle chains via sub-radiant plasmon modes. *Opt. Express*, 19(7):6450, 2011.

[66] G. G. Giusteri, F. Mattiotti, and G. L. Celardo. Non-hermitian Hamiltonian approach to quantum transport in disordered networks with sinks: Validity and effectiveness. *Phys. Rev. B*, 91:094301, 2015.

[67] B. Leggio, R. Messina, and M. Antezza. Thermally activated nonlocal amplification in quantum energy transport. *EPL*, 110(4):40002, 2015.

[68] P. Doyeux, R. Messina, B. Leggio, and M. Antezza. Excitation injector in an atomic chain: Long-range transport and efficiency amplification. *Phys. Rev. A*, 95:012138, 2017.

[69] P. Doyeux, S. A. H. Gangaraj, G. W. Hanson, and M. Antezza. Giant interatomic energy-transport amplification with nonreciprocal photonic topological insulators. *Phys. Rev. Lett.*, 119:173901, 2017.

[70] A. Mattioni, F. Caycedo-Soler, S. F. Huelga, and M. B. Plenio. Design principles for long-range energy transfer at room temperature. arXiv:1812.07905, 2018.

[71] S. Filipp, A. F. van Loo, M. Baur, L. Steffen, and A. Wallraff. Preparation of subradiant states using local qubit control in circuit QED. *Phys. Rev. A*, 84:061805, 2011.

[72] K. Lalumière, B. C. Sanders, A. F. van Loo, A. Fedorov, A. Wallraff, and A. Blais. Input-output theory for waveguide QED with an ensemble of inhomogeneous atoms. *Phys. Rev. A*, 88:043806, 2013.

[73] S. D. Jenkins, J. Ruostekoski, N. Papasimakis, S. Savo, and N. I. Zheludev. Many-body subradiant excitations in metamaterial arrays: Experiment and theory. *Phys. Rev. Lett.*, 119:053901, 2017.

[74] P. Lodahl, A. Floris van Driel, I. S. Nikolaev, A. Irman, K. Overgaag, D. Vanmaekelbergh, and W. L. Vos. Controlling the dynamics of spontaneous emission from quantum dots by photonic crystals. *Nature*, 430:654, 2004.

[75] P. Tighineanu, R. S. Daveau, T. B. Lehmann, H. E. Beere, D. A. Ritchie, P. Lodahl, and S. Stobbe. Single-photon superradiance from a quantum dot. *Phys. Rev. Lett.*, 116:163604, 2016.

[76] J.-H. Kim, S. Aghaeimeibodi, C. J. K. Richardson, R. P. Leavitt, and E. Waks. Super-radiant emission from quantum dots in a nanophotonic waveguide. *Nano Lett.*, 18(8):4734, 2018.

[77] F. Damanet, D. Braun, and J. Martin. Master equation for collective spontaneous emission with quantized atomic motion. *Phys. Rev. A*, 93(2):022124, 2016.

[78] K. Blum. *Density matrix theory and applications*, volume 64. Springer Science & Business Media, 2012.

[79] M. O. Scully and M. S. Zubairy. *Quantum optics*. Cambridge University Press, 1997.

[80] D. H. Kobe. Gauge transformations and the electric dipole approximation. *Am. J. Phys.*, 50(2):128–133, 1982.

[81] M. Schwartz. *Principles of Electrodynamics*. Dover Books on Engineering. Dover Publications, 1987.

[82] A. Beiser. *Concepts of modern physics*. Tata McGraw-Hill Education, 2003.

[83] S. Barnett and P. M. Radmore. *Methods in theoretical quantum optics*, volume 15. Oxford University Press, 2002.

[84] R. Loudon. *The quantum theory of light*. OUP Oxford, 2000.

[85] X. Zhou, X. Xu, X. Chen, and J. Chen. Magic wavelengths for terahertz clock transitions. *Phys. Rev. A*, 81(1):012115, 2010.

[86] D. F. V. James. Frequency shifts in spontaneous emission from two interacting atoms. *Phys. Rev. A*, 47(2):1336, 1993.

[87] P. Lambropoulos and D. Petrosyan. *Fundamentals of quantum optics and quantum information*, volume 23. Springer, 2007.

[88] A. Sitek and A. Manolescu. Dicke states in multiple quantum dots. *Phys. Rev. A*, (4):043807, 2013.

[89] H. Zoubi and H. Ritsch. Superradiant and dark exciton states in an optical lattice within a cavity. *EPL*, 87(2):23001, 2009.

[90] A. Sitek and A. Manolescu. Spontaneous generation of entangled exciton in quantum dot systems. *Opt. Quantum Electron.*, 46(4):613–621, 2014.

[91] Y. Miroshnychenko, U. V. Poulsen, and K. Mølmer. Directional emission of single photons from small atomic samples. *Phys. Rev. A*, 87:023821, 2013.

[92] A. Rivas and S. F. Huelga. *Open quantum systems*. Springer, 2012.

[93] J. E. Sansonetti and G. Nave. Wavelengths, transition probabilities, and energy levels for the spectrum of neutral strontium (Sr i). *J. Phys. Chem. Ref. Data*, 39(3):033103, 2010.

[94] M. A. Norcia, R. J. Lewis-Swan, J. R. K. Cline, B. Zhu, A. M. Rey, and J. K. Thompson. Cavity-mediated collective spin-exchange interactions in a strontium superradiant laser. *Science*, 361(6399):259–262, 2018.

[95] F. Schwabl. *Quantum Mechanics*. Springer-Verlag Berlin Heidelberg, 4 edition, 2007.

[96] C. J. Foot et al. *Atomic physics*, volume 7. Oxford University Press, 2005.

[97] H. J. Kimble. The quantum internet. *Nature*, 453:1023, 2008.

[98] A. I. Lvovsky, B. C. Sanders, and W. Tittel. Optical quantum memory. *Nat. Photonics*, 3:706, 2009.

[99] H. De Riedmatten, M. Afzelius, M. U. Staudt, C. Simon, and N. Gisin. A solid-state light-matter interface at the single-photon level. *Nature*, 456(7223):773, 2008.

[100] W. Tittel, M. Afzelius, T. Ere, R. L. Cone, S. Kröll, S. A. Moiseev, and M. Sellars. Photon-echo quantum memory in solid state systems. *Laser & Photon. Rev*, 4:244, 2010.

[101] M. P. Hedges, J. J. Longdell, Y. Li, and M. J. Sellars. Efficient quantum memory for light. *Nature*, 465:1052, 2010.

[102] I. Aharonovich, D. Englund, and M. Toth. Solid-state single-photon emitters. *Nat. Photonics*, 10:631, 2016.

[103] T. Zhong, J. M. Kindem, J. G. Bartholomew, J. Rochman, I. Craiciu, E. Miyazono, M. Bettinelli, E. Cavalli, V. Verma, S. W. Nam, et al. Nanophotonic rare-earth quantum memory with optically controlled retrieval. *Science*, 357(6358):1392–1395, 2017.

[104] E. Saglamyurek, N. Sinclair, J. Jin, J. A. Slater, D. Oblak, F. Bussières, M. George, R. Ricken, W. Sohler, and W. Tittel. Broadband waveguide quantum memory for entangled photons. *Nature*, 469:512, 2011.

[105] S. Marzban, J. G. Bartholomew, S. Madden, K. Vu, and M. J. Sellars. Observation of photon echoes from evanescently coupled rare-earth ions in a planar waveguide. *Phys. Rev. Lett.*, 115:013601, 2015.

[106] G. Corrielli, A. Seri, M. Mazzera, R. Osellame, and H. De Riedmatten. Integrated optical memory based on laser-written waveguides. *Phys. Rev. Appl.*, 5:054013, 2016.

[107] B. Vermersch, P. O. Guimond, H. Pichler, and P. Zoller. Quantum state transfer via noisy photonic and phononic waveguides. *Phys. Rev. Lett.*, 118:133601, 2017.

[108] B. Julsgaard, J. Sherson, J. I. Cirac, J. Flurášek, and E. S. Polzik. Experimental demonstration of quantum memory for light. *Nature*, 432:482, 2004.

[109] T. Chanelière, D. N. Matsukevich, S. D. Jenkins, S. Y. Lan, T. A.B. Kennedy, and A. Kuzmich. Storage and retrieval of single photons transmitted between remote quantum memories. *Nature*, 438:833, 2005.

[110] C.-W. Chou, H. De Riedmatten, D. Felinto, S. V. Polyakov, S. J. Van Enk, and H. J. Kimble. Measurement-induced entanglement for excitation stored in remote atomic ensembles. *Nature*, 438(7069):828, 2005.

[111] V. V. Kuz'min, A. N. Vetlugin, and I. V. Sokolov. Control of parameters of quantum memory for light in a cavity configuration. *Opt. Spectrosc.*, 119(6):1004–1009, 2015.

[112] E. Saglamyurek, M. Grimau Puigibert, Q. Zhou, L. Giner, F. Marsili, V. B. Verma, S. Woo Nam, L. Oesterling, D. Nippa, D. Oblak, and W. Tittel. A multiplexed light-matter interface for fibre-based quantum networks. *Nat. Comm.*, 7:11202, 2016.

[113] M. Parniak, M. Dabrowski, M. Mazelanik, A. Leszczyński, M. Lipka, and W. Wasilewski. Wavevector multiplexed atomic quantum memory via spatially-resolved single-photon detection. *Nat. Comm.*, 7:2140, 2017.

[114] A. Kalachev and S. Kröll. Coherent control of collective spontaneous emission in an extended atomic ensemble and quantum storage. *Phys. Rev. A*, 74:023814, 2006.

[115] A. Kalachev. Quantum storage on subradiant states in an extended atomic ensemble. *Phys. Rev. A*, 76:043812, 2007.

[116] R. Zhao, Y. O. Dudin, S. D. Jenkins, C. J. Campbell, D. N. Matsukevich, T. A. B. Kennedy, and A. Kuzmich. Long-lived quantum memory. *Nat. Phys.*, 5:100, 2009.

[117] X. Deng, V. E. Kravtsov, G. V. Shlyapnikov, and L. Santos. Duality in power-law localization in disordered one-dimensional systems. *Phys. Rev. Lett.*, 120:110602, 2018.

[118] T. Botzung, D. Vodola, P. Naldesi, M. Müller, E. Ercolessi, and G. Pupillo. Algebraic localization from power-law couplings in disordered quantum wires. *Phys. Rev. B*, 100:155136, 2019.

[119] E. Akkermans and A. Gero. Cooperative effects in one-dimensional random atomic gases: Absence of single-atom limit. *EPL*, 101(5):54003, 2013.

[120] A. Biella, F. Borgonovi, R. Kaiser, and G. L. Celardo. Subradiant hybrid states in the open 3D Anderson-Dicke model. *Europhys. Lett.*, 103(5):57009, 2013.

[121] R. M. Gray et al. Toeplitz and circulant matrices: A review. *Found. Trends Commun. Inf. Theory*, 2(3):155–239, 2006.

[122] T. H. Berlin and M. Kac. The spherical model of a ferromagnet. *Phys. Rev.*, 86(6):821, 1952.

[123] P. Vernaz-Gris, K. Huang, M. Cao, A. S. Sheremet, and J. Laurat. Highly-efficient quantum memory for polarization qubits in a spatially-multiplexed cold atomic ensemble. *Nat. Commun.*, 9(1):1–6, 2018.

[124] N. Sangouard, C. Simon, H. De Riedmatten, and N. Gisin. Quantum repeaters based on atomic ensembles and linear optics. *Reviews of Modern Physics*, 83(1):33, 2011.

[125] P. L DeVries and J. E. Hasbun. *A first course in computational physics*. Jones & Bartlett Publishers, 2011.

[126] R. Yamamoto, J. Kobayashi, T. Kuno, K. Kato, and Y. Takahashi. An ytterbium quantum gas microscope with narrow-line laser cooling. *New J. Phys.*, 18:023016, 2016.

[127] M. Miranda, R. Inoue, N. Tambo, and M. Kozuma. Site-resolved imaging of a bosonic Mott insulator using ytterbium atoms. *Phys. Rev. A*, 96:043626, 2017.

[128] M. A. Norcia, A. W. Young, and A. M. Kaufman. Microscopic control and detection of ultracold strontium in optical-tweezer arrays. *Phys. Rev. X*, 8:041054, 2018.

[129] M. Saffman, T. G. Walker, and K. Mølmer. Quantum information with rydberg atoms. *RMP*, 82(3):2313, 2010.

[130] N. Šibalić and C. S. Adams. *Rydberg physics*. IOP Publishing, 2018.

[131] F. Le Kien and A. Rauschenbeutel. Nanofiber-mediated chiral radiative coupling between two atoms. *Phys. Rev. A*, 95:023838, 2017.

[132] P. Lodahl, S. Mahmoodian, S. Stobbe, A. Rauschenbeutel, P. Schneeweiss, J. Volz, H. Pichler, and P. Zoller. Chiral quantum optics. *Nature*, 541:473, 2017.

[133] S. A. H. Gangaraj, G. W. Hanson, and M. Antezza. Robust entanglement with three-dimensional nonreciprocal photonic topological insulators. *Phys. Rev. A*, 95:063807, 2017.

[134] G. Buonaiuto, R. Jones, B. Olmos, and I. Lesanovsky. Dynamical creation and detection of entangled many-body states in a chiral atom chain. *New J. Phys.*, 21(11):113021, 2019.

[135] A. Albrecht, L. Henriet, A. Asenjo-Garcia, P. B. Dieterle, O. Painter, and D. E. Chang. Subradiant states of quantum bits coupled to a one-dimensional waveguide. *New J. Phys.*, 21(2):025003, 2019.

[136] H. H. Jen. Selective transport of atomic excitations in a driven chiral-coupled atomic chain. *J. Phys. B*, 52(6):065502, 2019.

[137] H. H. Jen, M.-S. Chang, G.-D. Lin, and Y.-C. Chen. Subradiance dynamics in a singly-excited chiral-coupled atomic chain. arXiv:1905.00558, 2019.

[138] C. Weitenberg, M. Endres, J. F. Sherson, M. Cheneau, P. Schauß, T. Fukuhara, I. Bloch, and S. Kuhr. Single-spin addressing in an atomic Mott insulator. *Nature*, 471:319, 2011.

[139] H. Kim, W. Lee, H.-G. Lee, H. Jo, Y. Song, and J. Ahn. In situ single-atom array synthesis using dynamic holographic optical tweezers. *Nat. Comm.*, 7:13317, 2016.

[140] M. Endres, H. Bernien, A. Keesling, H. Levine, E. R. Anschuetz, A. Krajenbrink, C. Senko, V. Vuletic, M. Greiner, and M. D. Lukin. Atom-by-atom assembly of defect-free one-dimensional cold atom arrays. *Science*, 354(6315):1024, 2016.

[141] D. Barredo, S. de Léséleuc, V. Lienhard, T. Lahaye, and A. Browaeys. An atom-by-atom assembler of defect-free arbitrary two-dimensional atomic arrays. *Science*, 354(6315):1021, 2016.

[142] A. Cooper, J. P. Covey, I. S. Madjarov, S. G. Porsev, M. S. Safronova, and M. Endres. Alkaline-earth atoms in optical tweezers. *Phys. Rev. X*, 8:041055, 2018.

[143] M. O. Araújo, I. Krešić, R. Kaiser, and W. Guerin. Superradiance in a large and dilute cloud of cold atoms in the linear-optics regime. *Phys. Rev. Lett.*, 117:073002, 2016.

[144] S. Jennewein, L. Brossard, Y. R. P. Sortais, A. Browaeys, P. Cheinet, J. Robert, and P. Pillet. Coherent scattering of near-resonant light by a dense, microscopic cloud of cold two-level atoms: Experiment versus theory. *Phys. Rev. A*, 97(5):053816, 2018.

[145] P. Földi, M. G. Benedict, and A. Czirják. Preparation of decoherence-free, subradiant states in a cavity. *Phys. Rev. A*, 65(2):021802, 2002.

[146] F. Robicheaux and S. Huang. Atom recoil during coherent light scattering from many atoms. *Phys. Rev. A*, 99(1):013410, 2019.

[147] P. Weiss, A. Cipris, M. O. Araújo, R. Kaiser, and W. Guerin. Robustness of Dicke subradiance against thermal decoherence. *Physical Review A*, 100(3):033833, 2019.

[148] S. D. Jenkins, J. Ruostekoski, J. Javanainen, R. Bourgain, S. Jennewein, Y. R. P. Sortais, and A. Browaeys. Optical resonance shifts in the fluorescence of thermal and cold atomic gases. *Phys. Rev. Lett.*, 116(18):183601, 2016.

[149] A. S. Kuraptsev and I. M. Sokolov. Influence of atomic motion on the collective effects in dense and cold atomic ensembles. *Physical Review A*, 101(3):033602, 2020.

[150] J. Zeiher, P. Schauß, S. Hild, T. Macrì, I. Bloch, and C. Gross. Microscopic characterization of scalable coherent Rydberg superatoms. *Phys. Rev. X*, 5(3):031015, 2015.

[151] J. A. Needham, I. Lesanovsky, and B. Olmos. Subradiance-protected excitation transport. *New J. Phys.*, 21(7):073061, 2019.

[152] S. L. Campbell, R. B. Hutson, G. E. Marti, A. Goban, N. D. Oppong, R. L. McNally, L. Sonderhouse, J. M. Robinson, W. Zhang, B. J. Bloom, et al. A fermi-degenerate three-dimensional optical lattice clock. *Science*, 358(6359):90–94, 2017.

[153] N. Poli, M. Schioppo, S. Vogt, U. Sterr, C. Lisdat, G. M. Tino, et al. A transportable strontium optical lattice clock. *Appl. Phys. B*, 117(4):1107–1116, 2014.

[154] M. A. Norcia and J. K. Thompson. Cold-strontium laser in the superradiant crossover regime. *Phys. Rev. X*, 6(1):011025, 2016.

[155] M. M Boyd. High precision spectroscopy of strontium in an optical lattice: Towards a new standard for frequency and time.

[156] M. Enderlein, T. Huber, C. Schneider, and T. Schaetz. Single ions trapped in a one-dimensional optical lattice. *Phys. Rev. Lett.*, 109(23):233004, 2012.

[157] P. Verkerk, D. R. Meacher, A. B. Coates, J.-Y. Courtois, S. Guibal, B. Lounis, C. Salomon, and G. Grynberg. Designing optical lattices: an investigation with cesium atoms. *EPL*, 26(3):171, 1994.

[158] J. A. Sherman, N. D. Lemke, N. Hinkley, M. Pizzocaro, R. W. Fox, A. D. Ludlow, and C. W. Oates. High-accuracy measurement of atomic polarizability in an optical lattice clock. *Phys. Rev. Lett.*, 108(15):153002, 2012.

[159] Y. Wang, S. Shevate, T. M. Wintermantel, M. Morgado, G. Lochead, and S. Whitlock. Preparation of hundreds of microscopic atomic ensembles in optical tweezer arrays. arXiv:1912.04200, 2019.

[160] A. Browaeys and T. Lahaye. Many-body physics with individually controlled Rydberg atoms. *Nature Physics*, pages 1–11, 2020.

[161] S. de Léséleuc, D. Barredo, V. Lienhard, A. Browaeys, and T. Lahaye. Analysis of imperfections in the coherent optical excitation of single atoms to Rydberg states. *Physical Review A*, 97(5):053803, 2018.

[162] I. Ferrier-Barbut. Personal communication.

[163] A. Glicenstein, G. Ferioli, N. Sibalic, L. Brossard, I. Ferrier-Barbut, and A. Browaeys. Collective shift in resonant light scattering by a one-dimensional atomic chain. arXiv:2004.05395, 2020.

[164] R. T. Sutherland and F. Robicheaux. Coherent forward broadening in cold atom clouds. *Phys. Rev. A*, 93(2):023407, 2016.

[165] T. Ido, T. H. Loftus, M. M. Boyd, A. D. Ludlow, K. W. Holman, and J. Ye. Precision spectroscopy and density-dependent frequency shifts in ultracold Sr. *Phys. Rev. Lett.*, 94(15):153001, 2005.

[166] R. Jones, G. Buonaiuto, B. Lang, I. Lesanovsky, and B. Olmos. Collectively enhanced chiral photon emission from an atomic array near a nanofiber. *Phys. Rev. Lett.*, 124(9):093601, 2020.

[167] Z. Meir, O. Schwartz, E. Shahmoon, D. Oron, and R. Ozeri. Cooperative Lamb shift in a mesoscopic atomic array. *Phys. Rev. Lett.*, 113(19):193002, 2014.

[168] J. Javanainen, J. Ruostekoski, Y. Li, and S.-M. Yoo. Shifts of a resonance line in a dense atomic sample. *Phys. Rev. Lett.*, 112(11):113603, 2014.

[169] Y.-X. Zhang and K. Mølmer. Theory of subradiant states of a one-dimensional two-level atom chain. arXiv:1812.09784, 2019.

[170] D. Tiarks, S. Schmidt-Eberle, T. Stolz, G. Rempe, and S. Dürr. A photon–photon quantum gate based on Rydberg interactions. *Nat. Phys.*, 15:124, 2019.